

THE DYNAMICS OF A MANTLE WITH A PLUME-FED ASTHENOSPHERE

--

METHOD DEVELOPMENT AND NUMERICAL EXPERIMENTAL STUDIES

A Dissertation

Presented to the Faculty of the Graduate School

of Cornell University

In Partial Fulfillment of the Requirements for the Degree of

Doctor of Philosophy

by

Chao Shi

January 2012

© 2012 Chao Shi

THE DYNAMICS OF A MANTLE WITH A PLUME-FED ASTHENOSPHERE

--

METHOD DEVELOPMENT AND NUMERICAL EXPERIMENTAL STUDIES

Chao Shi, Ph. D.

Cornell University 2012

This dissertation is composed of three studies addressing different but related problems on dynamic processes occurring in a Plume-fed Asthenosphere system, as well as techniques for improving numerical models of mantle convection. The first paper, *2D Numerical Experiments on a Plume-fed Asthenosphere: Necessary Preconditions and Implications for Geoid and Dynamic Topography*, performs a suite of 2D finite element-based experiments that explore what conditions are needed so that mantle flow includes a plume-fed asthenosphere (PFA) as a key part of its flow pattern. We find that a plume flux  $\sim$ 1.2 times big as the slab flux is needed for a persistent PFA. The numerical experiments also demonstrate that, instead of generating dynamic topography on the sea floor, flow-induced dynamic relief due to sub-asthenospheric density anomalies will preferentially form at the base of a buoyant asthenosphere, which is a promising mechanism to explain why Earth's  $\pm$ 100m Geoid variations are associated with much less than  $\sim$ 2km of dynamic topography at Earth's surface. The second paper, *A Quasi-Cspline*

*Interpolation Algorithm for Data on Unstructured Triangular and Tetrahedral Meshes*, develops a quasi-cubic Hermite spline interpolation algorithm for 2D and 3D scattered data, fitting both nodal values and slopes to the edges of triangular or tetrahedral cubic serendipity elements. This explicit recipe for 2D and 3D interpolation has been tested in vectorized and parallelized Matlab code, and has been used in both 2D and 3D large numerical simulations using unstructured triangular and tetrahedral meshes. The third paper, *Plume-asthenosphere-lithosphere Interactions Within a Mantle with a Plume-fed Asthenosphere: Implications for Hawaii- and Iceland-type Plume Dynamics*, studies the effects of on- and off-axis deep-mantle plumes with thermally controlled density and viscosity variations, assuming that thermal expansion controls density and that viscosity is governed by a temperature-dependent Arrhenius-type relation. The code we use is a parallel Matlab-based 3-D Finite Element code that we have developed, which utilizes unstructured tetrahedral meshes, and which can handle large and abrupt (6 orders of magnitude) viscosity contrasts (Hasenclever, PhD Dissertation 2010). In this paper, We show the results of: 1) the necessary conditions (plume flux, density contrast, viscosity contrast) for the existence of a PFA system with an on/off-axis plume; 2) resulting 3-D flow patterns in the asthenosphere, and the dynamic topography that is associated with them; 3) the decoupling effect of a buoyant and less viscous asthenosphere layer to the underlying mantle, and how this helps lead to relatively fixed hot spots.

## BIOGRAPHICAL SKETCH

Chao Shi was born in Chongqing, China on Feb. 14, 1984, and has been the only child in his family because of the “one-child policy” initiated in China around 1979. The major influences in his malleable years were his mom Shuxian Yu (1955-) and dad Jincheng Shi (1956-). Before moving to Xi'an, Shaanxi Province with his parents in 1993, he spent most of his first 9 years of childhood in Chongqing, including 3 years in the Elementary School Attached to Chongqing Geological Instrument Factory. During these 9 years, there were 2 short segments in which he would have potentially stayed longer either in Jinzhou, Liaoning Province with his grandparents, or in Haikou, Hainan Province because of a career opportunity for his parents, but in both cases he was soon brought back to Chongqing. In Xi'an, he received formal education in the Primary School Attached to the Institute 210 of China Aerospace Science & Industry Corporation (1993-1996), and the Middle School Attached to Northwestern Polytechnical University (1996-2002). At the age of 18 he entered Peking University, Beijing, and later received B.Sc. in Geophysics in 2006, upon which he moved to the US to study Geological Sciences / Computational Geodynamics at Cornell University, Ithaca, NY. He married Xinxin Cai (1983-) shortly before receiving his Ph.D. in Geological Sciences in 2011. Now as a doctor with his own family, he continues on his journey to learn new things and better understand the world.

Dedicated to Shuxian, Jincheng and Xinxin

献给我的父母和爱人

## ACKNOWLEDGMENTS

When younger, I felt that personal achievement is largely based on hard work from that individual; through the years I have learned more and more how everyone is helped and supported by others. One is extremely lucky to be born in a peaceful era, and keep finding great friends and mentors on the way to gain knowledge and enrich humanity.

I had a segmented childhood because of parents changing jobs and moving, while Chinese-style school hours and homework mercilessly ate into my spare time as a ‘kid’. Nonetheless, I have developed friendship among good groups of people in primary, middle and high schools. Thanks to the Internet, I am still chatting with them quite often. Among too many names, I would like to thank Chenxiang Ning and Fan Yang -- 2 very warm and dedicated then teenage boys – for great memories and friendships, I feel that we have always been together. I had 2 great head teachers during my middle and high school years, Xiaobai Zhuang and Hong Xie, who trusted me with character-shaping responsibilities and largely built my confidence interacting with people early on.

My years in Peking University had a stamping effect on me. There I met some of my greatest friends: Han Li, Ge Jin, Yang Zhao, Bo Tan, Xiang He, Yibing

Tang, Siqi Zhang, Yijie Zhou, Yao You, Hang Zhou, Chen Chen, Tianqi Liu and others. This peer group has been a source of motivation, as well as a target group sharing ideas with. Almost all of them came to the US / UK for advanced degrees. 2 educators -- Zijian Ni and Weiying Zhong -- carefully trimmed my personality, and cheered me up after an awful semester in my freshman year. I enjoyed learning from and interacting with professors like Xiaofei Chen, Yongen Cai, Jieyuan Ning and Shiyong Zhou, and probably learned the most from Prof. Yongshun John Chen. Joining John's research group has been inspiring and life-changing – modeling projects and group seminar series on Fridays greatly opened my eyes, and after 2 years as an undergraduate research assistant, I was led onto the track to join Cornell University and work with Prof. Jason Phipps Morgan.

While at Cornell I have enjoyed learning a ton from and working closely with Jason Phipps Morgan. I relied on Jason for all sorts of non-academic things too, and he always tried to get back to me as soon as possible, in a protective way. Bill White, Wilkins Aquino, Chris Andronicos, Larry Brown and Larry Cathles also largely influenced me – they helped Jason to support me, teach me, and provide me with career and life advice. I also thank department staff members Steve Gallow, Savannah Sawyer, Amy Colvin and Judy Starr for their continuous support. Faculty and staff members in Snee Hall have all been very warm to me, for which I am and always will be thankful, as it is very

important for any international student and his / her family. I shared most of my time at Cornell with group member Gregory Kirkpatrick, who has been my first and best friend made in the US, academic buddy and brother, language tutor, life coach and saver. He constantly shared thoughts with me, went to conferences and shared room with me, helped me with hardware / software issues, invited me to beer hours and parties, gave me rides and took me to visit places, and when I had US Visa issue in one summer, he drove me to Canada and back, during which he invited me to stay at his parents' house. I will be forever grateful to have you as a dear friend, Greg. Another fellow student Joerg Hasenclever, now a postdoc as well as co-author of mine, has been giving me hand-on and remote guidance and support, which helped me to become a developer later on. I also thank some other fellow students who greatly inspired and helped me: Jack Loveless, Peter Nester, Brian Ruskin, Neil McGlashan, Adam Goss, Holly (Caprio) Moore, Jacob Moore, Danielle (Glasgow) Wolf, David Wolf, Gabriela Depine, Pheobe Judge, Amanda Baker, Mary Kosloski, Sander Hunter, Bill Barnhart, Scott Henderson, Andrew Melkonian, Chen Chen (Female) and Ceren Karaca. This is a very diverse group, while they all share some great qualities as human beings – I have always been dreaming that I can be a combination of these people. Some of my undergrad friendships came to Cornell with me. They are my younger academic brothers from Peking University -- Chen Chen (CC), Tianqi Liu and Chao An. They brought much fun at school and on basketball courts, and took

good care of me when I was down or too busy. Ji Cheng, a physics student from Peking University, has also become a close friend, and offered me a room to stay when I was finishing this thesis. Thanks for your hospitality. I really looked forward to having a home to come back to after a long day's work. I would like to thank my awesome roommates Dan Deng, Chen Wang, Jack Liu, Fan Zhu, Yi Shen, and again Chen Chen (CC) and Ji Cheng. Xinxin and I had much fun with our go-to couple -- Chenxi Tian and Zhen Wang. We enjoyed BBQ gathering, camping, card game nights, and went on trips together. It is impossible to mention all my friends at Cornell. I thank them all. Among many other things, one key quality I have acquired when interacting with them, is being able to live with people who are better than me, and improving my own personality through mimicking and practice.

My family has been the greatest blessing of a pretty fortunate life. Thanks Mom and Dad, for helping me learn to live and love. Through good times and bad times, our hearts have been and will always be together. Thanks Xinxin, for loving me and carefully fixing holes in me. Thank you for joining my family and making everything better.

Finally, thanks to this era.

## TABLE OF CONTENTS

I.	Title Page	
II.	Copyright Page	
III.	Abstract	
IV.	Biographical Sketch.....	iii
V.	Dedication.....	iv
VI.	Acknowledgments.....	v
VII.	Table of Contents.....	ix
VIII.	Body of Dissertation	
<i>Chapter 1:</i> 2D Numerical Experiments on a Plume-fed Asthenosphere: Necessary Preconditions and Implications for Geoid and Dynamic Topography.....		1
<i>Chapter 2:</i> A Quasi-Cspline Interpolation Algorithm for Data on Unstructured Triangular and Tetrahedral Meshes.....		27
<i>Chapter 3:</i> Plume-asthenosphere-lithosphere Interactions Within a Mantle with a Plume-fed Asthenosphere: Implications for Iceland- and Hawaii-type Plume Dynamics.....		88

## CHAPTER 1

# 2D Numerical Experiments on a Plume-fed Asthenosphere: Necessary Preconditions and Implications for Geoid and Dynamic Topography

Chao Shi and Jason Phipps Morgan

Dept. of Earth and Atmospheric Sciences, Cornell Univ., Ithaca, NY 14853

### ***Abstract***

We explore what conditions are needed so that mantle flow includes a plume-fed asthenosphere (PFA) as a key structure within its large scale flow pattern. To do this, we performed a suite of 2D finite element-based experiments, exploring models that include the temperature-dependent rheological effects of ridge accretion, plate cooling, and well-resolved  $\sim$ 10-30km-thick asthenosphere dragdown by subducting slabs. We find that a plume flux  $\sim$ 1.2 times big as the slab flux is needed to maintain a persistent PFA. The numerical experiments also demonstrate that, instead of generating dynamic topography on the sea floor, flow-induced dynamic relief due to sub-

asthenospheric density anomalies will preferentially form at the base of a buoyant asthenosphere. We suggest this mode of dynamic internal relief may be associated with a significant fraction of the near surface density anomalies that create Earth's low-order geoid, and also associated with local relief at the base of the asthenosphere near plumes, ridges, and trenches that can be imaged in seismic experiments.

### ***Introduction***

The conventional picture of Earth's mantle convection is that it occurs in convection cells, with plates and slabs forming the cold top boundary layer of each cell (Fig. 1). We think this picture is too simple, and that a plume-fed asthenosphere may form an important dynamic boundary layer beneath the plates, especially when the lithosphere is relatively thin. If the asthenosphere is fed by hot plumes from the deep mantle, then it will be more buoyant and less viscous than its underlying mantle. This will lead to several dynamic effects: limited sub-slab asthenosphere entrainment; a pervasive counter flow pattern within the asthenosphere; broad asthenosphere decoupling of plates and deeper mantle except in the regions around subducting slabs and where thick cratonic roots may extend beneath the PFA; and dynamic links within the D"-plume-asthenosphere system (Phipps Morgan et al., 1995a; Phipps

Morgan et al., 2007; Yamamoto et al., 2007). Here we explore and quantify the potential significance of these effects, while also quantifying what the threshold plume flux is for a Plume-Fed Asthenosphere (PFA) to be a persistent structure in the convecting mantle.

The asthenosphere is observed in seismic studies as a low-seismic-velocity (Dziewonski and Anderson, 1981) and high-attenuation (Widmer et al., 1991) zone between ~100-300km depths. It is now known to be widely distributed underneath oceanic lithosphere (e.g. Gaherty et al., 1999; Nettles and Dziewonski, 2008; Dalton et al., 2009). However, beneath the stable continental regions, seismic speeds are much faster, implying a much stronger mantle between ~80-250 km depth (Goes and van der Lee, 2002). The seismic Low Velocity Zone (LVZ) is also considered by most scientists as a lower viscosity zone, as an effect of competing temperature and pressure conditions at the shallowest mantle (Weertman and Weertman, 1975; Buck and Parmentier, 1986; Karato and Wu, 1993). Furthermore, studies of oceanic plates and global stress distribution implies the existence of an asthenosphere with a viscosity of  $\sim 1E18\text{-}19$  Pa-s (Richter and McKenzie, 1978; Wiens and Stein, 1985; Ghosh et al, 2007), which is consistent with the viscosity estimates from glacier-rebound studies at Iceland (Sigmundsson and Einarsson, 1992) and other non-tectonic regions.

Several potential causal mechanisms have been proposed to explain the observed features of a shallow asthenosphere individually: the seismic LVZ is presumed to be due to the presence of partial melt in the asthenosphere but not deeper (Anderson, 1989; Hammond and Humphreys, 2000), or higher water content in the asthenosphere (Karato and Jung, 1998); the significant change in seismic attenuation between asthenosphere and underlying mantle is supposed to be related to a sharp increase in grain-size below the asthenosphere (Faul and Jackson, 2005); and the viscosity increase below the asthenosphere is proposed to be due to a change between dislocation creep within the asthenosphere and diffusion creep below the asthenosphere (Weertman and Weertman, 1975; Karato and Wu, 1993). However, all these observations can be more simply explained by the single unifying hypothesis that the plume-fed asthenosphere has a higher potential temperature than the underlying mesosphere.

We favor the Plume-fed Asthenosphere hypothesis that, the asthenosphere forms and persists as a simple consequence of plume upwelling from deep mantle. Hot buoyant material rises, until its ascent is stopped by overlying plates, where it forms a persistent hot and low viscosity layer that can only be effectively removed by near-surface cooling and transformation into lithosphere. Because of its temperature dependent buoyancy and low viscosity, it will tend to float above the rest of the mantle, and is hard for subducting

slabs to drag down at trenches (Phipps Morgan et al., 1995;2007).

A recent seismic geotherm study suggests that the asthenosphere underneath oceanic lithosphere could be around  $\sim$ 1400  $^{\circ}$ C, about 200  $^{\circ}$ C hotter than its underlying mantle (Cammarano and Romanowicz, 2007). This  $\sim$ 200  $^{\circ}$ C temperature anomaly would naturally lead to low seismic wavespeeds and high attenuation (Faul and Jackson, 2005), as well as a >100-fold reduction in viscosity, when the asthenosphere is both warmer and shallower than the underlying mantle in a dislocation creep scenario (Karato and Wu, 1993). This temperature difference would also introduce a  $\sim$ 0.7% density difference between the asthenosphere and its underlying mantle, as if the thermal expansion coefficient is  $3.3 \times 10^{-5} \text{ } ^{\circ}\text{C}^{-1}$ . Furthermore, any partial melt extraction would enhance this buoyancy effect even more (Oxburgh and Parmentier, 1977; Phipps Morgan et al, 1995b). In this way, the asthenosphere could remain as a persistent hotter-than-average region of the mantle if it is fed by observed mantle-penetrating plumes (Montelli et al. 2004, Wolfe et al., 2009) at a rate comparable to its rate of removal by lithosphere accretion and subduction. A more closer look at the emerging evidence supporting our PFA hypothesis can be found in Phipps Morgan et al. (2011). This study aims to test and quantify the earlier qualitative and boundary layer theory-based descriptions (Phipps Morgan et al., 1995:2007; Yamamoto et al., 2007).

## **Numerical Method**

We use the Finite Element Method to solve Stoke's equations for velocity and pressure, and also solve heat conduction & advection equations for the evolving temperature field. A Matlab-based 2D Finite Element code, inspired in many ways by the MILAMIN code (Debrowski et al, 2008), solves these equations. For the velocity and pressure problem, we choose the Uzawa method (Zienkiewicz and Taylor, 2000): in each time step, we solve first for pressure and velocity, then update temperature. For heat advection and diffusion, we use the operator splitting method: in each time step, we let heat diffuse by solving a diffusion-only heat equation with finite elements (Hughes, 2000), then we utilize the velocity field to find the backtrack positions for all nodes, conduct a cubic interpolation (Shi and Phipps Morgan, 2011) over the unstructured mesh for temperature on the backtrack positions, and then advect temperature profile in a semi-Lagrange fashion. Code techniques are described in more detail by Hasenclever (2010).

We utilize unstructured triangular meshes with quadratic elements to discretize the spatial domain. This decision is made to focus computational power into regions which will highly affect the global flow pattern -- in an earlier study

(Phipps Morgan et al., 2007), it was found that fine mesh in the slab-entrainment ‘sheet’ is very important for resolving the large scale pattern of counterflow within the asthenosphere. When the plate speed  $V$  is 100 km/Ma, viscosity of the asthenosphere  $\mu_{asth}$  is  $10^{19}$  Pa s, density contrast between the asthenosphere and its underlying mantle  $\Delta\rho_{asth}$  is  $\sim 320$  kgm $^{-3}$ , we estimate that the thickness of the asthenosphere entrainment sheet  $h$  is 20km, using equation  $h = \sqrt{4\mu_{asth}V/\Delta\rho_{asth}g}$  (Phipps Morgan et al., 2007). This requires at least a 3-5km resolution within the entrainment sheet.

### ***Model Setup: Mesh and Boundary Conditions***

Our numerical experiments here focus on assessing what average plume flux is needed for a plume-fed asthenosphere to exist as a persistent layer within the convecting mantle. The 2D model takes into account plume supply, ridge accretion, lithosphere cooling with age, and well-resolved slab dragdown effects, all of which must be accurately approximated for a ‘brute-force’ numerical experiment to accurately assess this basic question.

In these experiments, we do not let mantle plumes spontaneously form at the hot base of the mantle. Instead we extract mantle at a prescribed rate from a

single region near the bottom of the mantle (the ‘base of the plume stem’) and inject this hot material into the uppermost mantle by setting proper edge boundary conditions to model a ridge-centered plume, or utilizing dilatational elements to model off-axis plume-tops. We do this for two reasons. The lesser reason is that this would require variable locations of high resolution wherever the plume conduit formed – however this kind of adaptive mesh is fairly easy now for this type of 2D unstructured finite element code (Davis et al., 2008). The main reason is that, in a 2D numerical experiment, we cannot correctly treat the links between plume upwelling and surrounding mantle flow in a 2D Cartesian code -- a plume ‘conduit’ in a 2D Cartesian code actually represents an infinitely long sheet of upwelling in 3D. A 2D axisymmetric code would treat a ridge-centered plume conduit better, but couldn’t model lithosphere drag effects well. Furthermore, wherever we had an off-axis plume, we would ‘break’ the surrounding mantle flow into two separate subregions, a physical effect that happens around slabs, but not plumes, in the mantle’s actual 3D geometry. We bypass this issue by using a 2D Cartesian code and creating a ‘sink’ at the plume base and ‘source’ at the top of the would-be plume conduit. This bypasses the correct treatment of upwelling in the plume conduit, but neglects the (much less than 2D sheet-like) coupling between the plume’s pipe-like conduit and surrounding mantle flow. The numerical experiments do include a correct treatment of the effects of subducting slabs and slab drag-down — both of which are inherently 2D phenomena that can

be accurately treated in 2D numerical experiments.

The mesh shown in Fig. 2 is used to model the velocity and temperature field in asthenosphere and mantle. It covers a 6000-by-3000 km model space. We make this mesh with our own Matlab-based unstructured 2D triangular mesh generator ‘Mesh2dSpring’ (Shi and Phipps Morgan, 2009), which in turn is based on ideas in the DISTMESH unstructured mesh generator (Persson and Strang, 2004). Our goal is to obtain high resolution in the asthenosphere, the slab-entrainment ‘sheet’ (the thin asthenosphere layer which goes down alongside the slab), and the D” layer by having a fine mesh in these regions. Therefore mesh resolution varies in different regions from ~2km (near ridge and within the asthenosphere entrainment sheet) to ~500 km (in the middle of the mantle).

On the top boundary, the horizontal velocity boundary condition simulates a plate moving at a speed of 100 km/Ma, and the vertical velocity boundary condition is used to simulate the consumption of asthenosphere into the growing lithosphere. This is calculated from the thickness of oceanic lithosphere and the plate velocity (100 km/Ma), which is a combination of thermal and compositional lithosphere (Yale and Phipps Morgan, 1998). The lithospheric slab is then subducted back into the domain with a temperature profile calculated using the half-space cooling solution for a lithospheric

thermal boundary layer of appropriate plate age (Turcotte and Schubert, 2002). The velocity boundary condition on the left side is used to simulate a ridge-centered plume. Material flows out of the box through the ‘sink’ at the lower left corner (-2940 ~ -3000 km), and flows into the box through the ‘source’ beneath the ridge (-100 ~ -250 km) at a fixed temperature 1400 °C. Later in the paper we also use dilatational elements to make a ‘source’ beneath off-axis lithosphere, in order to move the plume away from the left domain boundary. All the rest of the domain boundary has symmetry boundary conditions, so that the plume-plate-slab system is the only factor moving mass and heat through the computational domain.

## **Results**

### *Generate the asthenosphere from a uniform mantle:*

The first set of experiments simulates the formation of a PFA from a uniform ambient mantle (Fig. 3). The ridge-centered (coming from the left side of the computational domain) hot plume flux forms a thin layer at the top of the cooler ambient mantle. When the asthenosphere material reaches the slab, it starts to go down with the slab. Soon after, the hot layer near the slab accumulates to a thickness where its intrinsic buoyancy starts to dominate the local pull from slab dragdown. When this happens, strong counterflow is set up within

the asthenosphere, as described in Phipps Morgan et al. (1995) and Yamamoto et al. (2007). In this simulation, we find that the maximum counter flow speed can be as fast as 60% of the plate speed, and only a ~10-20 km thick ‘sheet’ of  $\sim 10^{19}$  Pa s viscosity asthenosphere is entrained and downdragged by the subducting slab. We also see that as the asthenosphere layer grows towards the trench, the underlying mantle is progressively decoupled from surface plate motions, and starts to move much more slowly. When the asthenosphere forms a complete decoupling layer between the mesosphere and overlying plate, the subducting slab is the *only* region where plate motions directly couple with underlying sub-asthenospheric mantle flow.

*Plume flux effect (strong / weak / no plume):*

Next we conducted a series of experiments (Fig. 4) where we varied the plume flux to see its effect on the structure and flow pattern in the asthenosphere. In the strong-plume mode (plume supply =  $2 \times$  slab flux =  $2 \times$  lithosphere consumption > lithosphere consumption + slab drag-down), the asthenosphere grows thicker, which also involves a stronger counter flow. In a transient no-plume mode where we simply shut off the plume flux, the asthenosphere thins with time. It is very interesting that, in both cases, the base of the asthenosphere layer remains relatively flat and smooth. This is due to the combination of its buoyancy and low viscosity; only relatively small

asthenospheric pressure gradients are needed to transfer material laterally within the asthenosphere, and these are associated with relatively small (e.g. tens of km) tilt and relief at the base of the asthenosphere (and correspondingly  $\sim$ 50x smaller dynamic topography effects at the seafloor, where the density contrast is  $\sim$ 50x larger than the  $\sim$ 0.3-1% density contrast between asthenosphere and its underlying cooler and less depleted mantle). The counter flow pattern adjusts to generate a relatively uniform thickening/thinning fashion throughout the layer and simple uniform upwards or downwards movement of underlying cooler and more viscous mesosphere. Finally, we find that the asthenosphere maintains a steady thickness when the plume supply is about the same as the sum of the consumption of the lithosphere and the portion of asthenosphere dragged down by the slab, e.g., when the plume flux =  $1.1\text{--}1.2 \times$  slab flux.

*Dilation element runs: moving the plume-top ‘source’ off-axis.*

If, rather than being at the ridge, the plume head is close to the subduction slab, would all plume material be more effectively dragged down with the slab? To answer this question, we close the ‘source’ on the left boundary, and use dilatational elements close to  $x = 5000$  km,  $y = 0$  km to represent ‘source’ at the plume top, now located near the slab, for an intraplate plume (Fig. 5). We choose a strong plume flux, being twice the amount of the subducting slab flux,

and find that the asthenospheric counter flow would still show up, and it will go around the dilatation center (plume head) and preserve the general flow pattern within the layer. It is worth noting that: in 3D, asthenosphere counterflow can do this much easier, as it can migrate *laterally* around the local region where the plume is feeding the asthenosphere (Shi et al., 2011).

*Relief in asthenosphere: a possible explanation for the lack of correlation between geoid and dynamic topography.*

We also designed a series of experiments (Fig. 6) to explore the potential effects of a PFA on dynamic relief at the base of the asthenosphere, dynamic surface topography, and the geoid. In these experiments we place a hot/cold cylindrical anomaly centered 1000km beneath the top of the asthenosphere layer (in the middle of the fine mesh region of the grid in Fig. 6a). When buoyant material rises or dense material sinks, the base of the asthenosphere locally deflects upwards or downwards, correspondingly, while preserving its overall large-scale counter flow pattern. This provides a simple explanation for the existence of  $\sim \pm 100\text{m}$  surface geoid anomalies *without* the corresponding  $\pm 1\text{-}2\text{km}$  dynamic surface topography that is predicted by global geoid models (Thoraval et al., 1995, Cadek and Fleitout, 2006) — the geoid is due to internal mantle density anomalies (for example, as imaged by seismic tomography), but most of the near-surface density anomalies are not due to surface dynamic

topography, but instead to ~50-100km of dynamic relief along the base of the asthenosphere layer (Phipps Morgan et al., 1995; Yamamoto et al., 2007).

### ***Discussion***

These numerical experiments clearly show that in numerical flow simulations, lack of resolution at small but important regions within the simulation can strongly affect global flow pattern. Both lab and numerical experiments showed in an earlier study that properly resolving the thin asthenosphere entrainment sheet dragged by the subducting slab is critical to resolve the scale of counter flow within a buoyant low-viscous asthenosphere (Phipps Morgan et al., 2007) -- with a 2 orders of magnitude viscosity contrast and 1% density contract between the asthenosphere and its underlying mantle, we need at least ~5km resolution within the asthenosphere entrainment sheet to obtain a good solution for a counter flow in the asthenosphere. In general, the thickness of the downdragged sheet should can be estimated from the boundary layer estimate  $h = \sqrt{4\mu_{asth}V/\Delta\rho_{asth}g}$  (Phipps Morgan et al., 2007), so if the asthenosphere viscosity drops down to  $10^{18}$  Pa s, the entrainment sheet would be ~5km thick, therefore requiring ~1km numerical resolution to

model the behavior of this layer. Failure to provide this needed resolution results in numerical runs that artificially drag down too much hot and buoyant asthenosphere into deeper mantle, leaving less asthenosphere mass to feed large-scale counter flow. This is the main reason why this dragdown feature has not been seen in many previous 2D and 3D studies of the large-scale structure of mantle convection.

Asthenosphere acts as a decoupling layer whose base stays nearly flat as the layer thins or thickens. This is because of the asthenosphere's combination of buoyancy and low viscosity -- any flow needed to move material laterally is associated with relatively small lateral pressure gradients, hence only a slight long-wavelength tilt to the base of the asthenosphere. This effect helps the asthenosphere remain a persistent sub-oceanic feature while it may thins in periods of reduced plume supply or enhanced consumption effects such as the opening of an ocean basin (cf Phipps Morgan et al., 1995).

These numerical experiments also hint that there may be greatly different geochemical residence time scales within a large-scale pattern of 'whole mantle flow'. The experiments show a striking pattern of mantle flow: speeds in slabs, plumes, asthenosphere, and  $D''$  are relatively fast, while material introduced into other regions moves much more slowly, which would lead to much longer geochemical residence times. Therefore, a certain parcel near

the surface of the earth can either take a very long (>2 Ga) or short (200 Ma) time to be recycled back into the D'' region. This result suggests that the PFA is a scenario in which it is likely that both long-lived (~1-4 Ga) and short-lived (<500 Ma) subduction inputs can be simultaneously sampled as ‘components’ by mantle plumes fed by D'', without the need for ‘spatially isolated’ reservoirs in which to store these different-age mantle samples. Instead these regions have been ‘dynamically isolated’ by these two intrinsic differing timescales in mantle supply to D'' within whole mantle convection with plumes and a PFA.

Is the D'' another asthenosphere-like channel within the mantle? It is intriguing to think about where the hot plume material comes from. Both asthenosphere and D'' are places of greatest seismic anisotropy (Long, 2009). This could imply that anisotropy is due to fast strain rates or high strain (Brodholt et al., 2007), and not intrinsically due to dislocation creep – since D'' is thought to be at pressures where diffusion creep dominates. Maybe once again the mantle is telling a simpler story, and the enhanced anisotropy within the asthenosphere and D'' is a clue that both are regions of high strain-rates associated with strong lateral flow linked to a D''-plume-asthenosphere return flow to the downwelling associated with slab subduction.

## References

- Anderson, D.L., 1989. Theory of the Earth, Blackwell Scientific Publications.
- Brodholt, J.P., Helffrich, G. and Trampert, J., 2007. Chemical versus thermal heterogeneity in the lower mantle: The most likely role of anelasticity, *Earth Planet. Sci. Lett.*, 262, 429-437.
- Buck, W.R. and Parmentier, E.M., 1986. Convection beneath young oceanic lithosphere: Implications for thermal structure and gravity. *J. Geophys. Res.*, 91, 1961–1974.
- Cadek, O., and Fleitout, L., 2006. Effect of lateral viscosity variations in the core-mantle boundary region on predictions of the long-wavelength geoid, *Stud. Geophys. Geod.*, 50(2), 217-232.
- Dabrowski, M., Krotkiewski, M. and Schmid, D.W., 2008. MILAMIN: MATLAB-based finite element method solver for large problems, *Geochem. Geophys. Geosyst.*, 9, Q04030
- Dalton, C.A., Ekström, G. and Dziewonski, A.M., 2009. Global seismological shear velocity and attenuation: A comparison with experimental observations, *Earth Planet. Sci. Lett.*, 284, 65-75.
- Davies, D.R., Davies, J.H., Hassan, O., Morgan, K. & Nithiarasu, P., 2008. Adaptive finite element methods in geodynamics; Convection dominated mid-ocean ridge and subduction zone simulations. *Int. J. Num. Meth. Heat Fluid Flow*, 7-8, 1015-1035,
- Dziewonski, A. and Anderson, D.L., 1981. Preliminary reference Earth model. *Phys. Earth Planet. In.*, 25, 297–356.
- Gaherty, J.B., Kato, M. and Jordan, T.H., 1999. Seismological structure of the up- per mantle: a regional comparison of seismic layering. *Phys. Earth Planet. In.*, 110, 21–41.
- Ghosh, A., Wen, L., Holt, W.E., Haines, A.J. and Flesch, L.M., 2007. A best-fit lithosphere-mantle coupling model constrained by plate motions and the velocity gradient tensor field in the plate boundary zones, *EOS Trans. AGU*, 88(52), Fall Meet. Suppl., Abstract T21B-0582.
- Goes, S. and van der Lee, S., 2002. Thermal structure of the North American uppermost mantle inferred from seismic tomography. *J. Geophys. Res.*, 107, ETG2-1–ETG2-13.
- Hammond, W.C. and Humphreys, E.D., 2000. Upper mantle seismic wave velocity: effects of realistic partial melt geometries. *J. Geophys. Res.*, 105, 10975–10986.

Hasenclever, J., 2010. Modeling Mantle Flow and Melting Processes at Mid-Ocean Ridges and Subduction Zones - Development and Application of Numerical Models. Ph.D. Thesis.

Hughes, T.J.R., 2000. The Finite Element Method: linear static and dynamic Finite Element Analysis, Dover Publications, Inc.

Karato, S.-I. and Wu, P., 1993. Rheology of the upper mantle: a synthesis. *Science*, 260, 771–778.

Karato, S.-I. and Jung, H., 1998. Water, partial melting and the origin of the seismic low velocity and high attenuation zone in the upper mantle. *Earth Planet. Sci. Lett.*, 157, 193–207.

Long, M. D., 2009, Complex anisotropy in D'' beneath the eastern Pacific from SKS-SKKS splitting discrepancies, *Earth Planet. Sci. Lett.*, 283, 181-189.

Montelli, R., Nolet, G., Dahlen, F.A., Master, G., Engdahl, E.R. and Hung, S.-H., 2004. Finite-frequency tomography reveals a variety of plumes in the mantle, *Science*, 303, 338-343.

Nettles, M. and Dziewonski, A.M., 2008. Radially anisotropic shear velocity structure of the upper mantle globally and beneath North America, *J. Geophys. Res.*, 113, B02303.

Oxburgh, E.R., Parmentier, E.M., 1977. Compositional and density stratification in oceanic lithosphere-causes and consequences, *Journal of the Geological Society*, 133, 343-355

Persson, P.-O., Strang, G., 2004. A simple mesh generator in MATLAB. *SIAM Review*, 46(2), 329-345.

Phipps Morgan, J., Morgan, W.J., Zhang, Y.-S. and Smith, W.H.F., 1995a. Observational hints for a plume-fed sub- oceanic asthenosphere and its role in mantle convection. *J. Geophys. Res.*, 100, 12753–12768.

Phipps Morgan, J., Morgan, W.J. and Price, E., 1995b. Hotspot melting generates both hotspot volcanism and a hotspot swell? *J. Geophys. Res.*, 100, 8045–8062.

Phipps Morgan, J., 1997. The generation of a compositional lithosphere by mid-ocean ridge melting and its effect on subsequent off-axis hotspot upwelling and melting. *Earth Planet. Sci. Lett.*, 146, 213–232.

Phipps Morgan, J. and Morgan, W.J., 1999. Two-stage melting and the geochemical

evolution of the mantle: A recipe for mantle plum-pudding. *Earth Planet. Sci. Lett.*, 170, 215–239.

Phipps Morgan, J., Hasenclever, J., Hort, M., Rüpke, L. and Parmentier, E. M., 2007. On subducting slab entrainment of buoyant asthenosphere. *Terra Nova*, 19: 167–173.

Phipps Morgan, J., Shi, C., Hasenclever, J., 2011. New Observational and Experimental Evidence for a Plume-Fed Asthenosphere Boundary Layer in Mantle Convection, *Earth Planet. Sci. Lett.*, *submitted*.

Richter, F.M. and McKenzie, D., 1978. Simple plate models of mantle convection. *J. Geophys.*, 44, 441–471.

Sigmundsson, F. and Einarsson, P., 1992. Glacio-isostatic crustal movements caused by historical volume change of the Vatnajokull ice cap. *Geophys. Res. Lett.*, 19, 2123–2126.

Shi, C., Phipps Morgan, J., 2009. Plume-fed Asthenosphere: a possible origin for 250–350km deep seismic reflectors?, *Eos Trans. AGU*, 90(52), Fall Meet. Suppl., Abstract DI13A-1647.

Shi, C., Phipps Morgan, J., Hasenclever, J., 2011. Plume-asthenosphere-lithosphere interactions within a mantle with a Plume-fed Asthenosphere: implications for Hawaii- and Iceland-type plume dynamics, *in prep*

Thoraval, C., Machetel, P. and Cazenave, A., 1995. Locally layered convection inferred from dynamic models of the Earth's mantle, *Nature*, 375.

Turcotte, D. L. and Schubert, G., 2002, *Geodynamics*, 2<sup>nd</sup> Ed., Cambridge University Press.

Weertman, J. and Weertman, J.R., 1975. High temperature creep of rock and mantle viscosity. *Annu. Rev. Earth Planet. Sci.*, 3, 293–315.

Widmer, R., Masters, G. and Gilbert, F., 1991. Spherically symmetric attenuation within the Earth from normal mode data. *Geophys. J. Int.*, 104, 541–553.

Wiens, D.A. and Stein, S., 1985. Implications of oceanic intraplate seismicity for plate stresses, driving forces, and rheology. *Tectonophysics*, 116, 143–162.

Wolfe, C.J., Solomon, S.C., Laske, G., Collins, J.A., Detrick, R.S., Orcutt, J.A., Bercovici, D. and Hauri, E.H., 2009. Mantle shear-wave velocity structure beneath the Hawaiian hot spot, *Science*, 326, 1388-1390.

Yale, M. and Phipps Morgan, J., 1998, Asthenosphere flow model of hotspot–ridge

interactions: a comparison of Iceland and Kerguelen, *Earth Planet. Sci. Lett.*, 161, 1-4, 45-56.

Yamamoto, M., Phipps Morgan, J. and Morgan, W.J., 2007a. Global plume-fed asthenosphere flow—I: Motivation and model development, *Geological Society of America Special Papers*, 430, 165-188.

Yamamoto, M., Phipps Morgan, J. and Morgan, W.J., 2007b. Global plume-fed asthenosphere flow—II: Application to the geochemical segmentation of mid-ocean ridges, *Geological Society of America Special Papers*, 430, 189-208.

Zienkiewicz, O.C. and Taylor, R.L., 2000. *The Finite Element Method*, 5th Ed., Elsevier

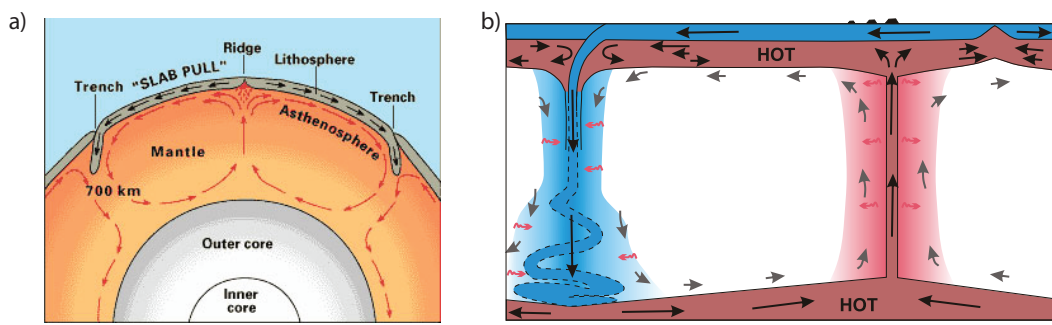


**Figure 1. Textbook mantle convection cell pattern vs. flow structures anticipated from a plume-fed asthenosphere. a) Cartoon of traditional interpretation of links between surface plate motions and whole mantle convection. b) Cartoon of flow structures within mantle convection that includes a Plume-fed Asthenosphere.**

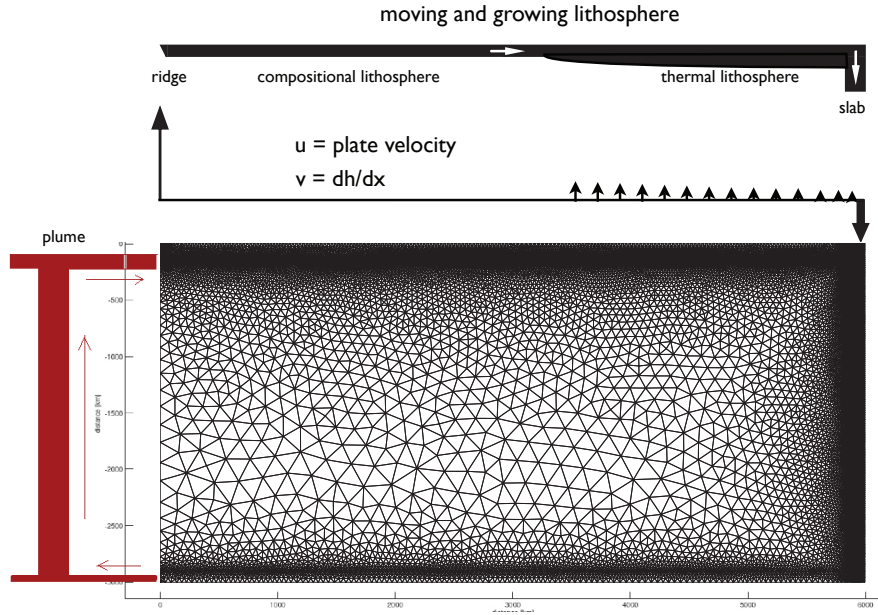


**Figure 2. Boundary conditions and a sample mesh used for the experiments shown in Figure 3. (a)** Top boundary condition treats the effects of ridge accretion, slab subduction, and a moving and growing oceanic lithosphere. The effect of a moving and growing lithosphere is modeled by prescribing a horizontal velocity and vertical outgoing flux along the top boundary, so that we mimic the situation that there is a lithosphere outside our computational domain shearing and consuming the asthenosphere. **(b)** Treatment of plume effects shown on the mesh generated with our Matlab based mesh generator ‘Mesh2dSpring’. Plume effects are modeled by taking out material from the bottom left corner, and putting exactly the same amount back into the domain on the left boundary near the top, at a temperature of 1400 C. We generate unstructured triangular meshes with varying resolution (element size) ranging from 5km to 300km, which corresponds to quadratic node spacing ranging from 2.5 to 150km. The finest resolution (~2.5km node spacing) is used near mid-ocean ridge (top left corner) and plume entrainment sheets (near top right corner), with fine-to-medium resolution at subducting slab (top right corner), within the asthenosphere (fine top layer) and within D'' (fine bottom layer).

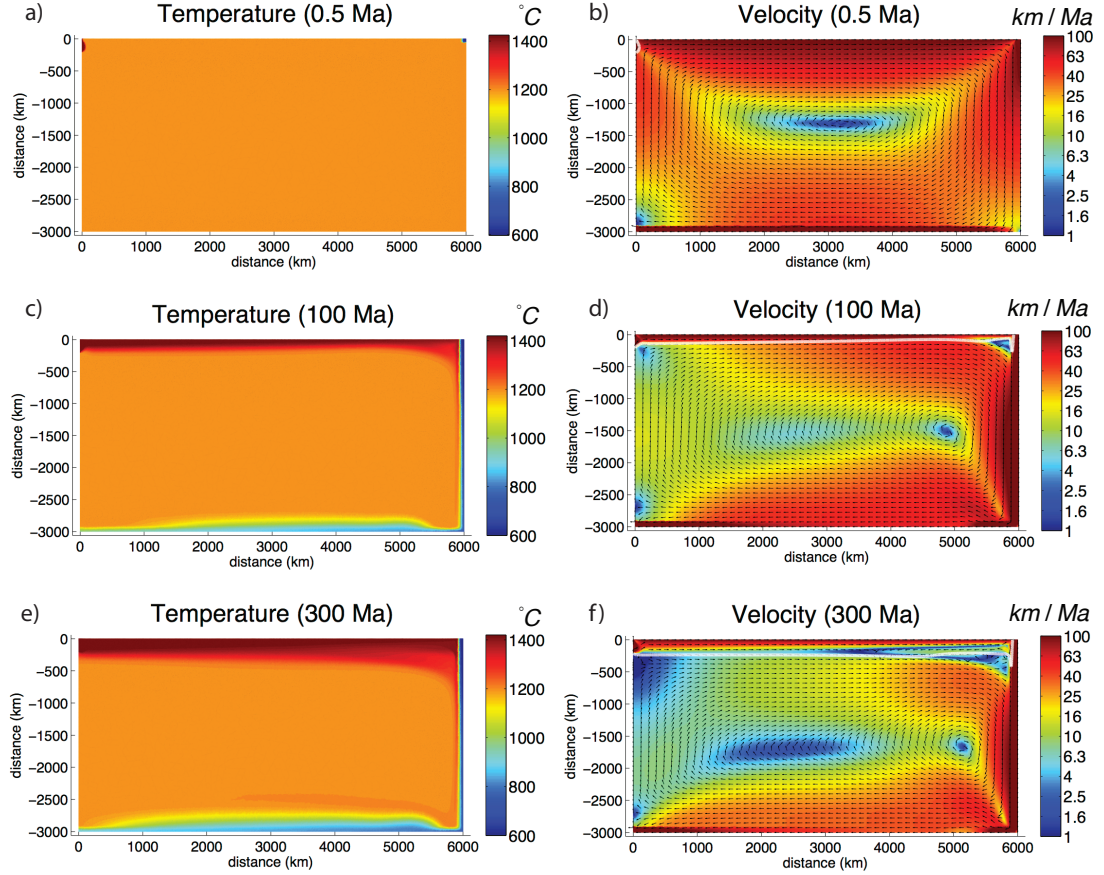


**Figure 3.** Panels showing the evolution of an experiment that generates a plume-fed asthenosphere layer from the starting condition of a uniform mantle. Left column shows temperature fields (temperature scales on the right of each panel), and right column shows corresponding velocity fields. In these panels, arrows show only the flow direction, and color is used to show the local speed (velocity scale on the right, note the logarithmic color scale used). White contour lines on the speed plots show the location of the  $1350^{\circ}$  C isotherms, which outline the boundary of hot asthenospheric material. The age in Ma of each snapshot is given at the top of each panel. The run started from a uniform mantle temperature of  $1200^{\circ}$  C. Hot plume material was fed into the box near the top left corner on the left boundary, with a similar mass flow removed from the lhs of the D'' region as shown in Figure 2. As the hot, buoyant and less viscous plume material enters, it immediately forms a lower viscosity layer that slows underlying mantle by decoupling it from surface plate motions. When this hot material accumulates to a certain thickness that produces enough buoyancy to locally resist slab dragdown, then counter flow begins within the asthenosphere layer, with the onset of a Plume-fed Asthenosphere flow structure within the lithosphere-mantle system. At the end of the experiment, well-developed counter flow is found in the asthenosphere, and the underlying mantle only “feels” the effects of plate/slab motion where the subducting slab penetrates beneath the asthenospheric decoupling layer.

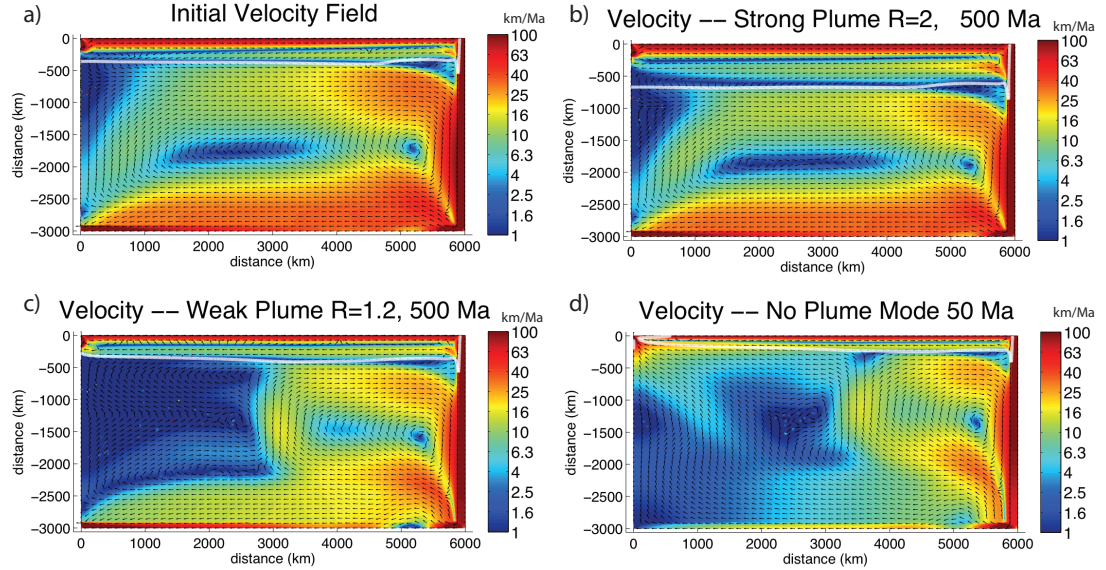


**Figure 4.** Snapshots of velocity structures that can arise with a time-varying plume flux. Plot format described in Figure 3. We first generate a) from a uniform mantle with a plume flux =  $2 * \text{slab flux}$  for 500 Ma, and use this as the starting point to vary plume flux. Panel b) shows the velocity field after keeping the ratio between plume flux and slab flux  $R$  at 2 for 500 Ma, this ‘strong’ plume continually grows the thickness of the asthenosphere. c) After switching to a ‘maintenance-level’ plume flux  $R = 1.2$  with the initial condition shown in a), after 500 Ma the asthenosphere retains about the same thickness. d) Lastly, when we completely turn off the plume, the asthenosphere is just consumed by ridge, growing lithosphere, and dragged down by slab. In this case, the asthenosphere would eventually be completely consumed by lithosphere growth and slab dragdown, and the mantle flow structure will return to the initial structure shown in Fig. 3b. Notice that because of the counter flow pattern, the asthenosphere stays quasi-flat independent of whether it is growing or shrinking.

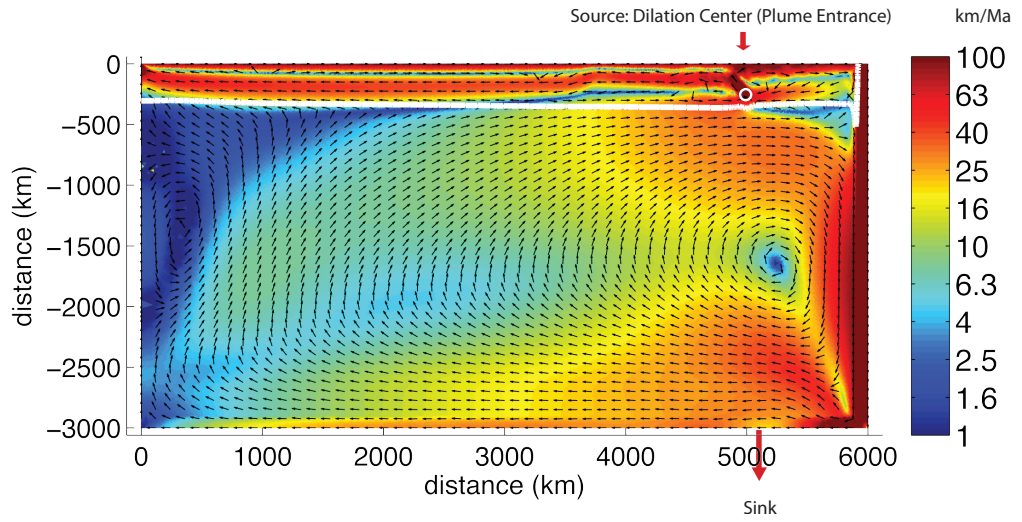


**Figure 5.** Snapshot of the velocity field from an experiment with off-axis plume flux that is introduced near the trench using dilatational elements. In this run the ‘plume top’ is located around 5000 km from the ridge axis. Plot format described in Figure 3. We see that even in 2D, buoyant asthenosphere fed by a near-trench plume would resist slab dragdown and create a persistent pattern of partial asthenosphere counter-flow. In 3D asthenosphere return flow is even easier, as it will wrap around the plume top as it returns towards the ridge.

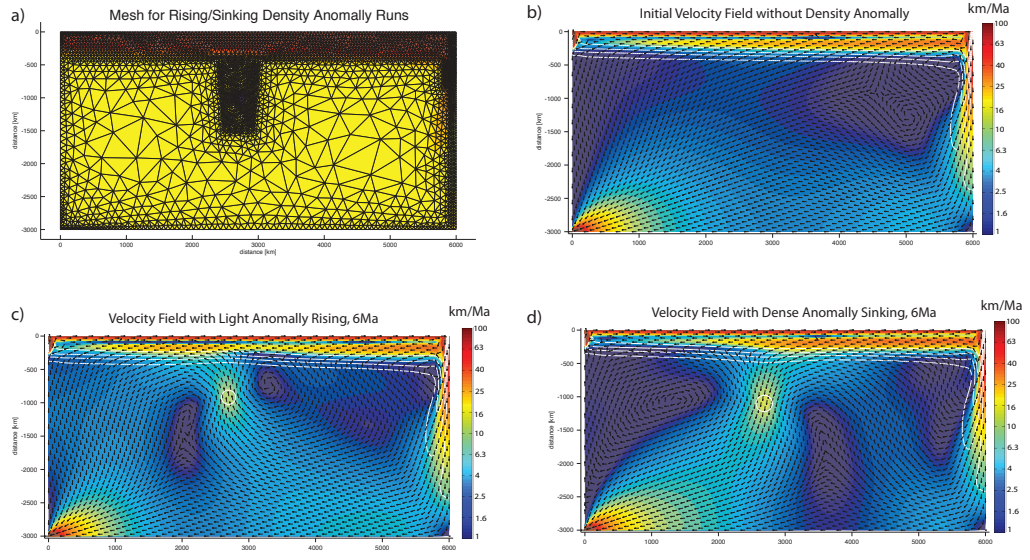


**Figure 6. Dynamic relief at the base of the asthenosphere can explain the apparent decoupling between Earth's Geoid and surface dynamic topography. Assume there is a cylindrical density anomaly below the base of a buoyant, lower viscosity asthenosphere. (The asthenosphere could even have a well-developed counter-flow pattern already developed as in the example shown here.) The subasthenospheric density anomaly generates dynamic relief at the base of the asthenosphere, while otherwise preserving the general pattern of counterflow and asthenospheric decoupling between surface plate motions and subasthenospheric mantle. This mechanism provides a potential physical mechanism for the lack of correlation between the geoid and dynamic topography on the sea floor.**

## CHAPTER 2

# A Quasi-Cspline Interpolation Algorithm for Data on Unstructured Triangular and Tetrahedral Meshes

Chao Shi and Jason Phipps Morgan

Dept. of Earth and Atmospheric Sciences, Cornell Univ., Ithaca, NY 14853

### ***Abstract***

We have developed a quasi-cubic Hermite spline interpolation algorithm for 2D and 3D scattered data, fitting both nodal values and slopes to the edges of triangular or tetrahedral cubic serendipity elements. Our method follows the approach of 1D Hermite cubic splines to fit nodal values and along-edge slope information, and utilizes serendipity-cubic or full-cubic Finite Element shape functions to extend values into the faces and interior of each triangular / tetrahedral element. This explicit recipe for 2D and 3D have been tested in vectorized and parallelized Matlab code, and has been used in both 2D and 3D large numerical simulations using unstructured triangular and tetrahedral meshes.

## **PART 1 -- *Introduction***

In both numerical modeling and data analysis, interpolation schemes are often necessary, increasingly for use on unstructured triangular and tetrahedral meshes. During interpolation, in addition to a desired accuracy, the user desires a ‘smooth’ interpolated field. In some numerical applications, the user may also want the interpolation method to suppress the generation of over-shoot and under-shoot values. These artifacts are often seen during interpolation when a smooth field changes sharply across a short distance, for near advective ‘shock’ fronts.

Smooth or blending function interplants were one of the first approaches to unstructured interpolation. These match a given function and slopes on the boundary of a triangle / tetrahedron. The first methods to construct these curved triangular surfaces were developed by Barnhill, Birkhoff and Gordon (1973). Their methods combine 3 univariate interpolants along the 3 edge-parallel lines going through the point of interest, by utilizing the Boolean sum scheme. Gregory (1974) introduced the convex combination method, which combines 3 Hermite projectors defined on the 3 parallels to edges. Later the side-vertex method was presented in Nielson (1979), with the use of 3 interpolants that each match conditions on a vertex and its facing edge. The common point of these methods is that the interpolations are: 1) at least C1

continuous over the entire domain; 2) constructed in a barycentric coordinate system; and 3) are non-trivial to extend to 3D. Attempts to extend these 2D schemes to 3D started with Alfeld (Alfeld, 1984). While they provide C1 or C2 continuity, these techniques lead to high order ( $\geq$ degree 5) polynomials that are typically over-complex for use in numeric modeling, and which can introduce unwanted oscillations in regions of rapid variation. In addition, their volume-face-edge logic is relatively complicated to implement, code, and execute.

The Finite Element Method uses shape functions to interpolate values from discrete ‘nodal’ locations to arbitrary locations within the computational domain. For triangles, standard linear interpolation only requires values on the vertices of each triangle. In conventional finite elements, higher-order element interpolations are associated with more complicated elements that have additional ‘nodal values’ at midside or internal element locations. Therefore, given a mesh composed of 4-node tetrahedra and only nodal function data (no derivative data), only linear interpolation is possible with standard shape functions. However, the alternative hierarchical element formulation (Zienkiewicz and Taylor, 2000) has the feature that higher order interpolations can be constructed using derivative (slope) information that is co-located at the vertex nodes.

Other proposed methods, e.g. the minimal energy method, least squares fitting, must solve a matrix inverse problem to obtain the parameters for their interpolants, which greatly increases the required computational work. Because of this disadvantage, here we propose a set of more accurate explicit interpolants that can be cheaply used in large computational modeling projects, in particular for 3D use with unstructured tetrahedral meshes.

Here we present a quasi-cubic Hermite spline (quasi-cspline) piecewise cubic interpolation scheme for both triangles and tetrahedra. In this scheme, both value and slope information are continuous within each tetrahedron and at the vertex of each tetrahedron, and interpolated values are determined from finite-element shape functions within each tetrahedron. Furthermore, the interpolation scheme involves only a local solution to determine the needed slope information at element vertices.

We consider the following situation: We are given a polygonal/polyhedral domain tessellated into triangles/tetrahedra, with prescribed function values at the vertices of the tessellation. Derivative data at vertices could also be given as a further constraint, but is not essential -- we can estimate nodal derivatives from nodal values, and then match those. The objective is to construct a quasi-smooth bivariate/trivariate function that interpolates vertices exactly with continuous derivatives at all element vertices and within all elements.

The scheme we present here has the following features: 1) The interpolation is C<sub>0</sub> continuous everywhere in the underlying domain, C<sub>1</sub> continuous within elements, around vertices, and along edges/faces in the edge/face-parallel direction, while across boundaries it is not defined to be C<sub>1</sub>; 2) It is local and explicit, so that the cost of interpolation on a given number of locations is independent of the total amount of data, and also that local changes in the data will only have local effects. 3) It uses polynomials no higher than 3rd order, with variants that can reproduce complete cubic polynomials. For practical use in Matlab this algorithm has been vectorized so that interpolation for multiple points is done as single vector operations.

The following sections are arranged as follows: In part 2, we describe the general idea of constructing this scheme, starting with a 1D presentation, and then introducing the steps needed to generalize this approach to 2D and 3D. In part 3, detailed 2D interpolants are presented. After this, in part 4 we describe the 3D recipe focusing on details that differ between 2D and 3D. In part 5, we show some tests for this interpolation scheme on triangular and tetrahedral meshes, and we finish with a short discussion of future possible extensions to this recipe.

## **PART 2 -- Quasi-Cspline Interpolation, Progressing from 1D to 3D**

Our idea is inspired by the 1D cubic Hermite spline scheme for 1D interpolation. This is defined as follows: On the unit interval  $[0,1]$ , given a starting point  $T_0$  at  $x=0$  and an ending point  $T_1$  at  $x=1$  with starting slope  $K_0$  at  $x=0$  and ending slope  $K_1$  at  $x=1$ , a unique cubic curve can be determined (Fig.1a). The resulting cubic polynomial is given by

$$T = (2x^3 - 3x^2 + 1)T_0 + (-2x^3 + 3x^2)T_1 + (x^3 - 2x^2 + x)K_0 + (x^3 - x^2)K_1 \quad (1)$$

where  $x \in [0,1]$ . Notice that each of the 4 terms in the above equation matches one of the 4 fitting constraints on nodal values and slopes:  $T_0$ ,  $T_1$ ,  $K_0$ , and  $K_1$ . (Fig.1b)

This cubic Hermite interpolation scheme is explicit, and naturally produces a C1 smooth cubic curve over the entire segmented 1D domain, which is highly desirable in various discrete modeling methods. However, a full extension of this 1D Hermite scheme to 3D unstructured mesh is difficult, and we will not attempt this here. Instead, we note that the Finite Element Method includes a set of less-standard shape functions -- hierarchical shape functions -- that can be used to decompose a within-element interpolation into linear, quadratic,

cubic terms, etc. (Zienkiewicz and Taylor, 2000). So if we combine the essence of 1D cubic Hermite interpolation with a strategic subset of hierarchical Finite Element shape functions, we can build a family of quasi-cspline interpolants on triangular (2D) and tetrahedral (3D) meshes that preserve full slope continuity within elements, at vertices shared by elements, and partial slope continuity along the interfaces between elements. (The lack of complete interface slope continuity is why we call this a quasi-cspline approach.)

To see how our interpolation basis functions relate to standard cubic Hermite interpolation, consider the following form for a 1D cubic interpolation that is defined for elements linked by a ‘vertex’ at each end of the 1D element (Fig. 1c). Our 1D cubic interpolant is defined by

$$T = (1-x)T_0 + xT_1 + (-x^2 + x)\frac{(K_o - K_{lin}) - (K_1 - K_{lin})}{2} + (2x^3 - 3x^2 + x)\frac{(K_o - K_{lin}) + (K_1 - K_{lin})}{2}$$

$$(2) \quad K_{lin} = (T_1 - T_0)/1 = T_1 - T_0 \\ (3)$$

where  $x \in [0,1]$ . Compared with the 4-term cubic Hermite spline shown in Fig. 1b, the unique cubic polynomial (Fig. 1a) is now decomposed into 4 different terms – 2 linear terms (one associated with each linear shape function in the element), and quadratic and cubic components. The linear terms match both

$T_0$  and  $T_1$ , while introducing a constant slope  $K_{lin}$  over the whole interval;

2) the quadratic term does not affect the function value at the 2 ends, while it applies 2 opposite-sense slopes at the ends; 3) the cubic term also does not affect function value at the ends, while introducing 2 equal slopes at the ends.

Finally, when we add the 4 shape function contributions together, this recipe (Fig. 1c) leads to the same cubic polynomial matching  $T_0, T_1, K_0$ , and  $K_1$  as does the construction for cubic Hermite interpolation (Fig. 1b).

Using this particular decomposition into linear, quadratic and cubic shape functions, there is a clear path to extend interpolation scheme onto unstructured grids in 2D and 3D. The idea is that we develop our interpolants on triangular and tetrahedral meshes to match both vertex values and vertex slopes -- as the cubic Hermite spline does in 1D. Since we build these interpolants from finite element shape functions, the resulting interpolations will be continuous everywhere, and will also have continuous derivatives within each element, and in the edge-parallel directions along interfaces between elements. (In 3D, we can also choose to make edge-normal slopes be continuous at the center of each element face — we will discuss the details to do this later.)

In a triangle, if we know both values and slopes at the 3 vertices of each triangle, then we have 9 independent constraints (1 nodal value and 2

gradients on each vertex). In each element, 9 linear to cubic shape functions are used to match this vertex information. The resulting interpolation is called a serendipity element in Finite Element terminology, because, while it contains complete linear and quadratic basis functions, its cubic basis set is missing a ‘bubble’ polynomial term (cf. Figure 3).

A complete set of bivariate cubic polynomials has 10 terms, so we can add this 10th shape function: its use will not change nodal values or nodal slopes, but will affect interpolated values in the interior of the triangle. In Finite Element discussions, this shape function is called a “bubble” function.

In a tetrahedron, matching vertex values and vertex slopes involves 16 independent constraints (1 value and 3 gradients on each of the 4 vertices), while a complete trivariate cubic polynomial series has 20 terms. In our tetrahedral scheme, there are a total of 20 shape functions: using only the first 16 generates a 3D serendipity element interpolation, while the last 4 shape functions are “bubble”-like functions, one associated with each face of the tetrahedron. Before we further discuss these details, we summarize the basic interpolation recipe in 2D.

### ***PART 3 -- 2D Interpolation on a Mesh of Unstructured Triangles***

We use finite element shape functions to construct the interpolation operator, keeping the spirit of spline interpolation at all vertices shared by many elements, while using FEM shape functions for easy-to-construct interpolation inside each element. This approach leads to the following continuity pattern:

- 1) At each node, both values and slopes are continuous.
- 2) Along edges, both values and derivatives in the edge-direction are continuous.
- 3) Across edges, values are continuous, but edge-normal derivatives can be discontinuous.
- 4) Within each element, both values and derivatives are continuous.

Since each unstructured element may have a different geometry, to avoid constructing a unique set of shape functions for each element, we instead chose to map all elements to a standard ‘parent’ element following standard FE approaches (Fig. 2). Here we present the shape functions in the r-s coordinate system of the parent element. All interpolation is done within this parent element, with values then mapped back to the original element. These operations involve standard bookkeeping approaches used in FE (cf. Zienkiewicz and Taylor, 2000: section 9 or Hughes, 2000: section 3).

Linear

$$N_1 = 1 - r - s$$

$$N_2 = r$$

$$N_3 = s$$

**Quadratic**

$$N_4 = r(1-r-s)$$

$$N_5 = \sqrt{2}rs$$

$$N_6 = s(1-r-s)$$

(4)

**Cubic**

$$N_7 = r(1-r-s)(1-2r-s)$$

$$N_8 = \sqrt{2}rs(s-r)$$

$$N_9 = s(1-r-s)(1-r-2s)$$

**Bubble**

$$N_{10} = rs(1-r-s)$$

To visualize these shape functions, we plot 4 representative functions in Fig. 3, each of which represents 1 of 4 distinct subcategories:  $N_1$  to  $N_3$  are *linear* shape functions matching nodal values, these 3 linear functions determine a plane, which contains the *linear background slopes*;  $N_4$  to  $N_6$  are *quadratic* shape functions matching the 2<sup>nd</sup> order perturbation (deviation from linear background slopes) along each of the 3 edges from linear shape functions, they adjust slopes at nodes without changing nodal values;  $N_7$  to  $N_9$  are *cubic* shape functions matching 3<sup>rd</sup> order perturbation (deviation from linear background slopes) along each of the 3 edges from linear shape functions – similar to quadratic ones, they only affect nodal slopes, but not nodal values;  $N_{10}$  is the ‘bubble’ function, which does not affect either nodal values or nodal slopes – it only changes values in the interior of an triangle.

Note that on a triangle we typically only have 9 pieces of information: 3 nodal values and 6 nodal slopes, therefore for most interpolation tasks, only the first 9 shape functions need be used. Combining the first 9 shape functions in 2D (Fig. 3a-c) is comparable to combining the 4 shape functions in 1D (Fig. 1c), in the sense that all nodal values and nodal slopes are matched. However a difference from 1-D interpolation is that the 4-term 1D interpolant is fully cubic while the 9-term 2D interpolant is missing one cubic term. The bubble function  $N_{10}$  would make the bivariate cubic polynomial series complete, but would need 1 additional piece of information to constrain its value.

Here is our preferred recipe to construct a 2D interpolation with these shape functions. The recipe starts from step 1 if only nodal values are given, jump to step 3 if both nodal values and slopes are known:

- 1) Find linear background slopes in each triangle: on each triangle, the 3 given nodal values and the coordinates of the 3 vertices defines a plane, the slopes of which are the desired linear background slopes. This is calculated with standard FEM algebra (cf. Zienkiewicz section 4.2.1).
  - 2) Calculate nodal slopes as a weighted average from neighboring elements.
- Fig. 4a shows an example geometry where all linear background slopes have

been calculated in the 6 triangles sharing node  $S$ ; the average of these slopes defines the slopes at  $S$ :  $K_{xs}$  and  $K_{ys}$ . This weighted average scheme can be a simple arithmetic mean, a distance weighted mean, an area weighted mean, etc. This step guarantees that interpolation in neighboring elements would be compatible (generated from same data on shared nodes), and that certain smoothness is achieved at each vertex as each node absorbs information from nearby elements. It also reduces extreme slopes through averaging.

3) Find the deviations from the ‘baseline’ linear slopes on each triangle: now that we have nodal values and slopes defined, we first need to find the deviation in the nodal slope from the linear background slope defined by the vertex nodal values. This is because our hierarchical shape function set is designed so that the linear shape functions  $N_1$  to  $N_3$  take care of both nodal values and linear background slopes, while quadratic and cubic shape functions  $N_4$  to  $N_9$  only take care of the *deviation* in nodal slope from the linear background. The linear background slopes are denoted as  $K_{ex}$  and  $K_{ey}$  (step 1 shows how to calculate them), and the deviation in slope for node  $A$  is denoted as  $K_{1x}^d$  and  $K_{1y}^d$ , with the relationships

$$K_{1x}^d = K_{1x} - K_{ex}$$

$$K_{1y}^d = K_{1y} - K_{ey}$$

where  $K_{1x} = \frac{\partial T_1}{\partial x}$ ,  $K_{1y} = \frac{\partial T_1}{\partial y}$  are slopes at node A (Fig. 2 and 5).

4) Map nodal values and slopes to parent element (Fig. 5): here we map all nodal values and slopes from their original x-y space to the parent element r-s space – with  $T_1$ ,  $T_2$  and  $T_3$  unchanged, all slope deviations  $K_{1x}^d$ ,  $K_{1y}^d$ ,  $K_{2x}^d$ ,  $K_{2y}^d$ ,  $K_{3x}^d$  and  $K_{3y}^d$  are mapped to  $K_{1r}^d$ ,  $K_{1s}^d$ ,  $K_{2r}^d$ ,  $K_{2q}^d$ ,  $K_{3q}^d$  and  $K_{3s}^d$  (Zienkiewicz, section 9). Note that along edge  $B'C'$ , we define a unit vector  $q$  pointing from  $C'$  to  $B'$ .

5) Construct final interpolant: with the 9 pieces of information defined in r-s space, we can combine these with shape functions  $N_1$  to  $N_9$ , arriving at a weighted sum

$$\begin{aligned} T(r,s) = & T_1 N_1 + \frac{K_{1r}^d - K_{2r}^d}{2} N_4 + \frac{K_{1r}^d + K_{2r}^d}{2} N_7 \\ & + T_2 N_2 + \frac{K_{3q}^d - K_{2q}^d}{2} N_5 + \frac{K_{3q}^d + K_{2q}^d}{2} N_8 \\ & + T_3 N_3 + \frac{K_{1s}^d - K_{3s}^d}{2} N_6 + \frac{K_{1s}^d + K_{3s}^d}{2} N_9 \end{aligned} \quad (5)$$

To better demonstrate what this interpolant does, we next describe 2 ways to interpret it. The first interpretation is that we can decompose it into 3 parts: the linear part ( $N_1$  to  $N_3$ ) is the standard linear interpolation on triangles; the quadratic part ( $N_4$  to  $N_6$ ) adds a 2<sup>nd</sup> order perturbation – imagine combining Fig. 3b and its 2 counter parts bulging up on edge  $A'B'$  and  $B'C'$  together; and the cubic part ( $N_7$  to  $N_9$ ) adds a 3<sup>rd</sup> order perturbation – visualize a combination of Fig. 3c and its 2 counter parts. Another perspective is that this interpolant is doing what Fig. 1c does on each edge – matching 2 nodal values and 2 *along-edge* slopes on the ends of each edge, and when all 3 edges are treated this way, the combination satisfies all 9-constraints at the 3 vertices of the triangle. Note too that, along each edge between neighboring elements, we have constructed a 1D spline between the edge's two vertex nodes.

Using this 9-piece interpolant, we have constructed a particular type of quasi-cubic serendipity element that with the addition of a central bubble function would be the minimal full cubic interpolant. The interpolated result around a given node has an ‘umbrella-skeleton’ structure (Fig. 4b). (For computational use in MATLAB, this algorithm has been vectorized to interpolate multiple locations simultaneously, and also parallelized for interpolation on multi-compute-domain data sets. Because it results in finite-element-like interpolation, it is particularly easy to implement for smooth quasi-cubic interpolation within a finite element calculation.)

## **PART 4 -- 3D Interpolation on a Mesh of Unstructured Tetrahedra**

This 2D interpolation recipe was designed to be straightforward to extend to 3D, replacing triangles by tetrahedral. In 3D, the interpolation recipe retains these features:

- 1) At each node, both values and slopes fit the known data, and are continuous.
- 2) Along edges, both values and slopes in the edge-direction are continuous.
- 3) Along each face, both values and face-parallel slopes are continuous.
- 4) Across each face, values are continuous, but face-normal derivatives are usually discontinuous.
- 5) Within the element, both values and first derivatives are continuous.

As in 2D, we choose to map all tetrahedral in xyz space to a unit tetrahedra in rst space (with 3 edges lying on 3 axes, each from 0 to 1), and perform interpolation in the regular tetrahedron in rst space, and map value back to xyz space (Fig. 6). Standard Finite Element reference books (cf. Zienkiewicz, section 9 or Hughes, section 3) describe this standard mapping and bookkeeping approach in detail.

Because of the use of standard finite element mapping to a reference parent element, we only need to define 1 set of cubic shape functions on the reference right-tetrahedron:

### Linear

$$N_1 = r$$

$$N_2 = s$$

$$N_3 = t$$

$$N_4 = 1 - r - s - t$$

### Quadratic

$$N_5 = \sqrt{2}rs$$

$$N_6 = \sqrt{2}st$$

$$N_7 = t(1 - r - s - t)$$

$$N_8 = r(1 - r - s - t)$$

$$N_9 = \sqrt{2}rt$$

$$N_{10} = s(1 - r - s - t)$$

### (6)

### Cubic

$$N_{11} = \sqrt{2}rs(s - r)$$

$$N_{12} = \sqrt{2}st(t - s)$$

$$N_{13} = t(1 - r - s - t)(1 - r - s - 2t)$$

$$N_{14} = r(1 - r - s - t)(1 - 2r - s - t)$$

$$N_{15} = \sqrt{2}rt(t - r)$$

$$N_{16} = s(1 - r - s - t)(1 - r - 2s - t)$$

### Bubble

$$N_{17} = st(1 - r - s - t)$$

$$N_{18} = rt(1 - r - s - t)$$

$$N_{19} = rs(1 - r - s - t)$$

$$N_{20} = rst$$

To visualize these shape functions is not a simple task, as they are intrinsically 4 dimensional plots. Instead, in Fig. 7 we mainly try to show the way these shape functions are constructed, and only visualize values on a single edge or face. We show 1 example from each of the 4 categories: 1) The *Linear* shape function  $N_1$  is designed so that its value is 0 on face  $B'C'D'$ , and 1 at vertex  $A'$  (Fig. 7a). When we combine the first 4 functions  $N_1$  to  $N_4$  together, it is the standard FE linear shape function set for a tetrahedron, which matches all 4 nodal values, and produces the *linear background slopes*. 2) The *Quadratic* shape function  $N_5$  is 0 on face  $A'C'D'$  and  $B'C'D'$ , and is non-zero values anywhere else within the tetrahedron and on edge  $A'B'$ . More importantly, the parameter  $\sqrt{2}$  along the ‘hypotenuse’ ensures that derivatives  $\left. \frac{\partial N_5}{\partial u} \right|_{B'} = 1$ ,  $\left. \frac{\partial N_5}{\partial u} \right|_{A'} = -1$ , which makes slope data fitting more convenient when these shape functions are used (Fig. 7b). 3) The *Cubic* shape function  $N_{11}$  is asked to be zero on face  $A'C'D'$ ,  $B'C'D'$  and a bisecting plane  $C'D'E'$  (Fig. 7c). Again, the parameter  $\sqrt{2}$  ensures that derivatives  $\left. \frac{\partial N_{11}}{\partial u} \right|_{A'} = \left. \frac{\partial N_{11}}{\partial u} \right|_{B'} = 1$ . 4) The *Bubble* function  $N_{20}$  is 0 on 3 faces  $A'B'D'$ ,  $A'C'D'$  and  $B'C'D'$ , and non-zero anywhere else (Fig. 7d). Shape function  $N_{20}$  has values and slopes of zero at all 4 vertices, therefore does not affect our fitting of nodal value or

nodal slope, but would change values within the face  $A'B'C'$ , and within the interior of the tetrahedral volume.

Note that on a tetrahedron with nodal values and derivatives specified, there are only 16 pieces of information: 4 nodal values and 12 nodal slopes, therefore for the simplest interpolation scheme, only the first 16 shape functions are used to define the interpolating function. Combining the first 16 shape functions in 3D is analogous to combining the first 9 shape functions in 2D (Fig. 3a-c), in the sense that all nodal values and nodal slopes are matched by this interpolation. The bubble functions  $N_{17} - N_{20}$  would make the trivariate cubic polynomial series complete, but 4 additional pieces of information are needed to constrain their values. This will be further discussed in later parts of the paper – unlike 2D, relatively easy local calculations can be used to generate these values.

The quasi-cubic interpolation recipe for tetrahedra is (start from step 1 if only nodal values are given, jump to step 3 if nodal values and slopes are both given):

- 1) Find linear background slopes in each tetrahedron: on each tetrahedron, the 4 given nodal values and the coordinates of the 4 vertices define the

desired linear background slopes. As in 2D, these are determined with standard FE algebra (cf. Zienkiewicz section 4.2.1).

- 2) Calculate nodal slopes as a weighted average from the slopes in the elements that share each vertex node. This is shown in Fig. 4a, all linear background slopes have been calculated in the 6 triangles sharing node  $S$ , and these slopes are averaged to obtain the slopes at  $S$ :  $K_{xs}$  and  $K_{ys}$ . The weighted average scheme can be a simple arithmetic mean, a distance weighted mean, an area weighted mean, etc. This step guarantees that interpolation in neighboring elements would be compatible (generated from same data on shared nodes), and that derivatives are continuous at each vertex node. It also reduces extreme slopes by averaging.
- 3) Find the deviations from the background linear slope within each tetrahedron: now that we have nodal values and slopes for a given tetrahedron, we first need to find the deviation in each vertex node's slopes from the tetrahedrons linear background slopes that arise from a linear interpolation fitting the 4 vertex values. This is because our hierarchical shape function set is designed so that the linear shape functions  $N_1$  to  $N_4$  take care of both nodal values and linear background slopes, while quadratic and cubic shape functions  $N_5$  to  $N_{16}$  only take care of the vertex slope *deviations* from the linear background slopes. Similar to the 2D case, the linear

background slopes in 3D are denoted as  $K_{ex}$ ,  $K_{ey}$  and  $K_{ez}$ , meaning element-wise slopes (step 1 shows how to calculate them), and the slope deviation of node  $A$  is denoted as  $K_{1x}^d$ ,  $K_{1y}^d$  and  $K_{1z}^d$  (Fig. 6), with the relationships

$$K_{1x}^d = K_{1x} - K_{ex}$$

$$K_{1y}^d = K_{1y} - K_{ey}$$

$$K_{1z}^d = K_{1z} - K_{ez}$$

where  $K_{1x} = \frac{\partial T_1}{\partial x}$ ,  $K_{1y} = \frac{\partial T_1}{\partial y}$  and  $K_{1z} = \frac{\partial T_1}{\partial z}$  are slopes at node  $A$  (Fig. 6).

4) Map nodal values and slopes to parent element (Fig. 6): here we map all nodal values and slopes from their original x-y-z space to the parent element r-s-t space – with  $T_1$ ,  $T_2$  and  $T_3$  unchanged, all slope deviations  $K_{1x}^d$ ,  $K_{1y}^d$ ,  $K_{1z}^d$ ,  $K_{2x}^d$ ,  $K_{2y}^d$ ,  $K_{2z}^d$ ,  $K_{3x}^d$ ,  $K_{3y}^d$ ,  $K_{3z}^d$ ,  $K_{4x}^d$ ,  $K_{4y}^d$  and  $K_{4z}^d$  are mapped to  $K_{1r}^d$ ,  $K_{1u}^d$ ,  $K_{1v}^d$ ,  $K_{2u}^d$ ,  $K_{2s}^d$ ,  $K_{2w}^d$ ,  $K_{3v}^d$ ,  $K_{3w}^d$ ,  $K_{3t}^d$ ,  $K_{4r}^d$ ,  $K_{4s}^d$  and  $K_{4t}^d$  (cf. Zienkiewicz, section 9). Note that along edge  $B'A'$ ,  $C'A'$  and  $C'B'$ , we define a unit vector  $u$ ,  $v$  and  $w$ , respectively. Their positive directions are chosen so that when we take the 3 right triangular faces  $A'C'D'$ ,  $B'C'D'$  and  $A'B'D'$  out of the unit tetrahedron, on each of the triangles the positive directions defined on the edges are the same as those in our 2D case (Fig. 5).

5) Construct the final interpolant for each tetrahedral element: with the 16 pieces of information defined in r-s-t space, we can combine these with shape functions  $N_1$  to  $N_{16}$ , arriving at a weighted sum

$$T(r,s,t) =$$

(7)

$$\begin{aligned} & T_1 N_1 + T_2 N_2 + T_3 N_3 + T_4 N_4 \\ & + \frac{K_{2u}^d - K_{1u}^d}{2} N_5 + \frac{K_{3w}^d - K_{2w}^d}{2} N_6 + \frac{K_{4t}^d - K_{3t}^d}{2} N_7 + \frac{K_{4r}^d - K_{1r}^d}{2} N_8 + \frac{K_{3v}^d - K_{1v}^d}{2} N_9 + \frac{K_{4s}^d - K_{2s}^d}{2} N_{10} \\ & + \frac{K_{2u}^d + K_{1u}^d}{2} N_{11} + \frac{K_{3w}^d + K_{2w}^d}{2} N_{12} + \frac{K_{4t}^d + K_{3t}^d}{2} N_{13} + \frac{K_{4r}^d + K_{1r}^d}{2} N_{14} + \frac{K_{3v}^d + K_{1v}^d}{2} N_{15} + \frac{K_{4s}^d + K_{2s}^d}{2} N_{16} \end{aligned}$$

To reiterate what the pieces of this interpolant do: the linear part ( $N_1$  to  $N_4$ ) is the standard linear interpolation on tetrahedra; the quadratic part ( $N_5$  to  $N_{10}$ ) adds a 2<sup>nd</sup> order perturbation that matches the ‘mean’ slope deviation of the two vertices sharing each edge – exactly as done for the 2D case -- imagine combining Fig. 3b and its 2 counter parts bulging up on edge  $A'B'$  and  $B'C'$  together, and translate this effect to 3D; and the cubic part ( $N_{11}$  to  $N_{16}$ ) adds a 3<sup>rd</sup> order perturbation that corrects for the difference in the slope deviation at each vertex from their mean value for each edge – e.g. Fig. 3c and its 2 counter parts are being ‘translated’ into 3D. Another perspective is that this interpolant is doing what Fig. 1c does on each edge – matching 2 nodal values and 2 *along-edge* slopes on the ends of each edge, and when all 6 edges are

treated this way, the combination satisfies all 16-pieces of constraints. Note too that, along each edge between neighboring elements, we have constructed a 1-D spline between the edge's two vertex nodes, just as was done in the corresponding 2D interpolant.

Using this 16-term interpolant, we have constructed a particular type of quasi-cubic serendipity element. A key feature of these interpolations is that they follow the essence of extending 1D splines into higher dimensional spaces, and use this 1-D fitting technique to construct interpolants in 2D and 3D. Figure 4b shows the multiple 1D spline-lines of an example local fitting surface for 2D interpolation. We mainly focus on fitting the 1D ‘skeleton’ element edges as splines (fitting nodal values and *along-edge* slopes), and let finite element shape functions extend the interpolation into the rest of the triangular area (2D) or tetrahedral volume (3D). This is why this technique can be readily extending from 2D to 3D (or higher dimensionality)

This algorithm in 3-D has also been vectorized in Matlab to interpolate on multiple locations simultaneously, and parallelized for interpolation on multi-domain data sets in a cluster environment.

## **PART 5 -- Assessment of the Quasi-Cspline Interpolation Scheme**

In this section, we examine several standard test problems to compare the new interpolation schemes with previous methods. For 2D, we use 2 sets of test cases to compare our 2D 9-piece interpolant with Nielson's side-vertex method (Nielson 1979), an even higher order method based on Nielson's developed by Zhang and Cheng (2002), standard linear FE interpolation, and Matlab's built-in interpolation subroutines ‘interp2.m’. For 3D, we use both Gaussian and Super Gaussian test cases to compare the 3D 16-term interpolation scheme with standard FE linear interpolations, and Matlab's built-in interpolation subroutine ‘interp3.m’. Note that Matlab's built-in ‘interp2.m’ and ‘interp3.m’ can provide both linear and cubic interpolations, but they only work on structured rectangular and brick meshes. That is why we also use regularly spaced meshes for these comparisons.

#### *2D test case1:*

The first set of test functions are the 6 bivariate functions proposed by Franke (1979), which were slightly modified and used in a more recent study (Zhang and Cheng, 2002). We adopt the ones used by Zhang and Cheng (2002):

$$F_1(x,y) = 3.9 \exp[-0.25(9x-2)^2 - 0.25(9y-2)^2] + 3.9 \exp[-(9x+1)^2/49 - (9y+1)/10]$$

$$+ 2.6 \exp[-0.25(9x-7)^2 - 0.25(9y-3)^2] - 1.04 \exp[-(9x-4)^2 - (9y-7)^2]$$

$$F_2(x,y) = 5.2 \exp(18y-18x) / [9 \exp(18y-18x) + 9]$$

$$F_3(x,y) = 5.2 [1.25 + \cos(5.4y)] / [64 - 6(3x-1)^2]$$

(8)

$$F_4(x,y) = 5.2 \exp\{-81[(x-0.5)^2 + (y-0.5)^2]/16\}/3$$

$$F_5(x,y) = 5.2 \exp[-81((x-0.5)^2 - (y-0.5)^2)/4]/3$$

$$F_6(x,y) = 5.2 \sqrt{64 - 81[(x-0.5)^2 + (y-0.5)^2]} / 9 - 2.6$$

The 33-point data set presented in (Franke, 1979) is used to generate triangles for comparison (Table 1). The triangulation of the data set (Fig. 8) is performed using ‘DelaunayTri’ command in Matlab, which is a Delaunay triangulation algorithm based on CGAL. Notice that this triangulation is exactly the same as those in (Zhang and Cheng, 2002) and (Franke, 1979).

We tried to test the different interpolation schemes in a manner than allows easy intercomparison with previous schemes. Therefore, we have defined a ‘coarse mesh’ with known ‘nodes’ (Table 1) and triangulation (Fig. 8), and calculate nodal values and nodal slopes using benchmark functions  $F_1(x,y)$  to  $F_6(x,y)$ . We then interpolate this scattered coarse field to a ‘fine mesh’ -- a 21x21 uniform node set also defined on  $[0,1]^2$ . Finally, we compare the interpolated values and benchmark values on the 21x21 fine mesh.

In this test, we compare 5 different schemes. The first 2 methods are Nielson's method (Nielson, 1979) and the Nielson-hybrid method (Zhang and Cheng 2002), the third method is our quasi-cspline method with 'known' exact nodal slopes, the fourth is our quasi-cspline method with approximated nodal slopes (see step 2 in our 2D interpolation recipe), and the fifth is the standard Finite Element linear interpolation, which is simply taking the 3 terms in (5) involving  $N_1$ ,  $N_2$  and  $N_3$  only.

The results are shown in Table 2, with the data in the first 2 rows – the Nielson method and the Nielson-hybrid taken directly from a table in (Zhang and Cheng 2002). We find that the max error produced by our full quadratic/incomplete cubic method is significantly larger than those by Nielson method and Zhang and Cheng's method, but is significantly smaller than the max error generated by standard Finite Element linear interpolation. We will discuss the reasons for this later in the discussion section, here we only state that the main cause is that Nielson method and Zhang and Cheng's method require two times or more constraints and polynomial fit terms than our method, their accuracy advantages become especially obvious when we interpolate within the largest triangles of the test mesh.

## *2D test case 2*

Here we base our 2D test case 2 on another set of meshes: these meshes (11x11 and 21x21 node meshes) are also defined on  $[0,1]^2$ , but with structured rectangular elements, with the uniformly spaced rectangular grid of node points divided into triangles by Matlab's 'DelaunayTri' command (Fig. 9). This allows these meshes to be alternately used as structured rectangular meshes for Matlab's cubic interpolation schemes for regular grids or as unstructured triangular meshes for our more general interpolation scheme – using the same nodes, but triangular instead of rectangular connections between nodes. Again we interpolate data from the 11x11 or 21x21 meshes to regular grids of 21x21 or 41x41 points defined on the same region. We also compare our technique to Matlab's built-in 'griddata.m' function that performs interpolation on unstructured triangles or tetrahedral.

We compare the following interpolation schemes: 1) the new quasi-cspline method with exact slopes prescribed, 2) the new method with slopes approximated according to the above recipe, 3) standard Finite Element linear interpolation on triangular elements, 4) Matlab's built-in 'interp2.m' with its 'linear' option on – a bilinear interpolation on a structured rectangular grid; 5) 'interp2.m' with 'cubic' option on – a bicubic interpolation on a structured

rectangular mesh; 6) Matlab's built-in 'griddata.m' with its 'cubic' option on – a cubic interpolation developed for scattered data interpolation (Yang, 1986).

The test functions we choose consist of all 6 bivariate functions proposed previously (8), and 2 Super Gaussian functions, which share a general form defined in spherical coordinate system:

$$f(r) = A_0 \exp(-2|r/L|^n)$$

(9)

where  $A_0$  is an amplitude constant,  $r$  is radius,  $L$  is waist,  $n$  is the Super Gaussian order ( $>2$ ). For testing purposes, here we translate the Super Gaussian to a 2D Cartesian system:

$$f(x,y) = A_0 \exp\left(-2\sqrt{x^2 + y^2}/L\right)^n$$

(10)

To determine the parameters  $A_0$ ,  $L$  and  $n$  that we shall use, we show in Fig. 10 the effects of order  $n$ : when  $n$  increases, the function turns closer and closer to a step function, which means a steeper 'ramp' – the sharper the

front is, the more challenging this function is for most interpolation methods.

We choose  $n = 5$ , and define 2 additional test functions:

$$\begin{aligned} F_7 &= \exp\left(-\left|\sqrt{(x-0.5)^2 + (y-0.5)^2}/0.2\right|^5\right) \\ F_8 &= \exp\left(-\left|\sqrt{(x-0.5)^2 + (y-0.5)^2}/0.4\right|^5\right) \end{aligned} \quad (11)$$

These 2 functions (11) usually involve both over- and under-shoot when interpolated, while the Gaussian-like case  $n=2$  is already tested in the previous functions  $F_4$  and  $F_5$  (8).

We compare both max errors and RMS errors on the regular grid of sampling points when interpolating with the previously mentioned 6 different methods. The results are shown in Table 3 (interpolated from the 11x11 coarse mesh data) and Table 4 (21x21 coarse mesh). We find that: 1) cubic interpolations are consistently more accurate than linear methods in terms of both max error and RMS error, which is easy to understand; 2) amongst cubic interpolation schemes, the new quasi-cspline method with exact slopes is the most accurate. This is the other cubic methods tested only requires nodal values and then approximate their necessary slope information from surrounding nodal values; 3) the new quasi-cspline method with approximated slopes is

generally on par with both ‘interp2.m’ and ‘griddata.m’ with their options set to ‘cubic’.

### *3D test cases*

To test our recipe in part 4, we choose to extend the Super Gaussian into 3D Cartesian system, which yields

$$f(x,y,z) = A_0 \exp\left(-2\left|\sqrt{x^2 + y^2 + z^2} / L\right|^n\right)$$

(12)

For the same reason explained in 2D test case 2, we choose  $n=5$ , and define our first 2 test functions in 3D as

$$\begin{aligned} F_9 &= \exp\left(-\left|\sqrt{(x-0.5)^2 + (y-0.5)^2 + (z-0.5)^2} / 0.2\right|^5\right) \\ F_{10} &= \exp\left(-\left|\sqrt{(x-0.5)^2 + (y-0.5)^2 + (z-0.5)^2} / 0.4\right|^5\right) \end{aligned}$$

(13)

The next 2 test functions are closer to Gaussian functions, which are an extension of  $F_4$  and  $F_5$  (8) in 3D:

$$\begin{aligned}
F_{11}(x,y) &= 5.2 \exp\left\{-81[(x-0.5)^2 + (y-0.5)^2 + (z-0.5)^2]/16\right\}/3 \\
F_{12}(x,y) &= 5.2 \exp\left\{-81[(x-0.5)^2 + (y-0.5)^2 + (z-0.5)^2]/4\right\}/3
\end{aligned}
\tag{14}$$

The coarse meshes we choose are  $11 \times 11 \times 11$  and  $21 \times 21 \times 21$  node regular rectangular meshes defined on  $[0,1]^3$ . These sets of nodes are tessellated by the Matlab command ‘DelaunayTri’ into 2 tetrahedral meshes (Fig. 11). To perform our interpolation tests, data defined on  $11 \times 11 \times 11$  or  $21 \times 21 \times 21$  coarse meshes is interpolated onto  $21 \times 21 \times 21$  or  $41 \times 41 \times 41$  node meshes respectively, and compared with the exact function values at these test points.

We compare 5 different interpolation methods here. The first 2 methods only work on structured brick / cube meshes: 1) Matlab’s built-in ‘interp3.m’ with ‘cubic’ interpolation option, and 2) ‘interp3.m’ with ‘linear’ interpolation option. These 2 methods are known to be fairly accurate on structured brick meshes. The next 3 methods work on unstructured tetrahedral meshes: 3) the new quasi-cspline scheme with *exact* nodal slopes; 4) the quasi-cspline scheme with *approximated* nodal slopes; 5) standard Finite Element linear interpolation.

In total, we have 8 different comparison groups – 4 test functions  $F_9$  to  $F_{12}$ , each with 2 sets of meshes. We have visualized 2 of the 8 test cases here:

Fig. 12 shows the coarse data on  $11 \times 11 \times 11$  mesh and benchmark field on  $21 \times 21 \times 21$  mesh for test function  $F_{10}$ ; Fig. 13 shows the error distributions using the 5 different methods mentioned in the above paragraph (we omit plotting the interpolated fields since there are no obvious visual differences); Fig. 14 shows the coarse data on  $21 \times 21 \times 21$  mesh and benchmark field on  $41 \times 41 \times 41$  mesh for test function  $F_{12}$ ; Fig. 15 shows the error distributions for this  $F_{12}$  test case. In the end, we show max error and RMS error measurements on Table 5.

From Table 5 we see that: 1) The new quasi-cspline method using exact slope information at nodes is the most accurate. However, this comparison is somewhat unfair since the other 4 methods either do not use slope information, or must approximate slope information from surrounding nodal values. 2) The quasi-cspline method with approximated slopes is comparable with the tricubic approach of ‘interp3.m’ in terms of accuracy. 3) The trilinear interpolation method in ‘interp3.m’ and the standard Finite Element linear interpolation method are the worst, even though they are widely used in 3D numerical calculations.

These examples have demonstrated that the Matlab subroutine ‘interp3.m’ is fairly accurate on structured brick meshes (‘Finite Difference type’ meshes), but their logic does not extend to unstructured meshes. On the other hand, the

new quasi-cspline method works on unstructured tetrahedral meshes, and its accuracy is comparable with the well-established cubic interpolation methods on structured brick meshes. Since more and more discrete numerical modeling techniques utilize tetrahedral meshes for their ability to flexibility fit irregular domain boundaries and incorporate variable element sizes, we think that this new interpolation recipe – especially in its 3D version – is likely to be of interest to many researchers and developers. It is also relatively cheap to compute, as it uses only local operations and tetrahedral elements with 16-20 term shape function coefficients.

Many high order element methods have been developed in Finite Element analysis, but typically these only have C<sub>0</sub> continuity between elements. Our method provides an explicit recipe to conduct quasi-cubic interpolation between the values defined by a mesh of linear 4-node tetrahedral elements, with or without additional nodal slope information.

### ***Part 6 -- Discussion***

*Nielson/Zhang methods are more accurate? Why?*

We first discuss the test differences between our quasi-cspline methods, the

Nielson method (1979) and its recent variant (Zhang and Cheng, 2002).

Regarding the 2D test case 1 comparison (33-node coarse mesh test) in part 5: The Nielson triangle function has 18 fitting parameters within a triangle (10 for full cubic, and 8 higher-than-cubic terms). This is exactly the same number of fitting parameters as if we made a fit with the mesh built using also all midside points on the edges on each triangle – now each triangle has 6 nodes, with 3 fitting constraints per node. In Figure 8, we show an example where we add a midside node on each edge of a triangle on the 33-node mesh (Fig. 8), and reconnect this enriched 121-node set with Matlab’s ‘DelaunayTri’ command. (The resulting mesh is shown in Fig. 16). A comparison of the Nielson/Zhang method on the 33-node mesh (Table 2) and our 2D method on the 121-node mesh (Table 6) is a more equal comparison because they have the same number of fitting parameters (although the Nielson-Zhang methods still have the advantage of a higher order polynomial basis).

Another advantage of the Nielson/Zhang methods is that they are C1 continuous everywhere, while our 2D method is C1 continuous everywhere except in directions perpendicular to element edges. The quasi-cspline method trades this ‘perfect’ C1 continuity property in return for a simpler, faster interpolation scheme that can easily be extended to 3D problems where computational work is also important. However, by making the interpolation C1

continuous at all vertex points (see the ‘umbrella-skeleton’ shape in Fig. 4), the result is that this method has smaller C1 edge discontinuities than do typical piecewise continuous finite elements.

### *The use of bubble functions*

We have previously noted that our interpolation recipe for 2D (5) and 3D (7) are only quasi-cubic, but do not contain all cubic polynomial terms. In 2D, a full bivariate cubic polynomial would need 10 fitting constraints -- we only have 9, while in 3D, a full trivariate cubic polynomial would need 20 fitting constraints - - we only use 16. In order to reproduce full cubic polynomials, we would need to add 1 element bubble function for 2D ( $N_{10}$  in equation 4) and 4 element bubble functions for 3D in ( $N_{17-20}$  in equation 6). Adding these bubble functions to our existing recipes (5, 7) would potentially make them more accurate if good additional fitting constraints are used.

However, we have already used all simple vertex-linked constraints, namely nodal values and nodal slopes (eqns. 5, 7). In order to add additional bubble functions, we need extra fitting constraints to determine the parameters applied to them. This means we need information from nodes that are outside

the element, or need to add new within element/inter-element smoothness constraints.

Here we propose 2 easy-to-compute ways to generate these extra fitting constraints in 3D that only require local calculations:

- 1) *Obtain an estimate for the value at the center of each triangle* (in 3D this means the center of each face, not the center of each tetrahedron). Notice that the bubble functions do not affect either nodal values or slopes, and has a maximum value at the center of the triangle it is defined on (Fig. 3d, Fig. 7d), we could easily add bubble functions to our existing shape functions to match the center value. In 3D this fitting estimate of the value at the center of each tetrahedral face could be an inverse-distance-weighted average of the nodal values of the two elements that share that face. In 2D, if we extrapolate nodal information outside a triangle to generate each triangle-center fitting value, this could potentially degrade local accuracy in regions with rapid variations, as it would be an extra multiple-element smoothing process.
- 2) *Apply additional smoothness constraints*. For example, we could ask that all face-normal derivatives be continuous at the center of each face, or that the face-normal curvature be zero at the center of each face.

## ***Part 7 – Summary***

We present a quasi-cspline interpolation algorithm for unstructured triangular and tetrahedral data. Our method follows the essence of 1D cubic Hermite spline (cspline) interpolation by using and fitting nodal values and vertex slopes with unstructured edge-segments of each triangle/tetrahedron, and utilizes Finite Element hierarchical shape functions to interpolate values within each triangular / tetrahedral element. This means that the computational work needed for smooth interpolation is essentially that for a serendipity cubic finite element. We have tested the quasi-cspline recipe for 2D and 3D interpolation using vectorized and parallelized Matlab code, and have also used the resulting scheme for the treatment of semi-Lagrange advection in large 2D and 3D numerical simulations on unstructured triangular and tetrahedral meshes (Phipps Morgan and Shi, 2011, Hasenclever, PhD thesis; Hasenclever et al., 2011). It provides accuracy comparable to that of cubic-spline-based interpolation schemes that work only on regular finite-difference-type meshes, and is less accurate, but also less computationally intensive than the Nielson ‘family’ of C1-interpolation schemes (Nielson, Zhang) for triangular tessellations. Unlike Nielson’s interpolation scheme, the quasi-cspline scheme generalizes naturally to irregular 3D tetrahedral meshes, where it provides a

significant improvement to linear and to piecewise continuous finite element interpolations.

## Reference

- Alfeld, P. (1984). A discrete C<sub>1</sub> interpolant for tetrahedral data. *Rocky Mountain J. of Mathematics*, 14, 5-16.
- Barnhill, R., Birkhoff, G., & Gordon, W. (1973). Smooth interpolation in triangles. *Journal of Approximation Theory*, 8 (2), 114-128.
- Franke, R. (1979). A critical comparison of some methods for interpolation of scattered data.
- Gregory, J. (1974). Smooth interpolation without twist constraints. *Computer Aided Geometric Design*, 71-87.
- Hasenclever, J., Phipps Morgan, J., Hort, M., & Rüpke, L. (2011). 2D and 3D numerical models on compositionally buoyant diapirs in the mantle wedge. *Earth Planet. Sci. Lett.*, in press
- Hughes, T.J.R. (2000). The Finite Element Method: linear static and dynamic Finite Element Analysis, Dover Publications, Inc.
- Nielson, G. (1979). The side-vertex method for interpolation in triangles. *Journal of Approximation Theory*, 25 (4), 318-336.
- Yang, T.Y. (1986). Finite Element structural analysis, Prentice Hall, 446-449
- Zhang, C., & Cheng, F. (2002). Triangular patch modeling using combination method. *Computer aided geometric design*, 19 (8), 645-662.
- Zienkiewicz, O.C. and Taylor, R.L. (2000). The Finite Element Method, 5th Ed., Elsevier



**Table 1.** List of x-y coordinates for the 33-point mesh discretization used in Test 1 (Franke, 1979).

X	Y	X	Y
0	0	0.05	0.45
0	1	1	0
0	0.5	1	1
0.5	1	0.5	0
0.1	0.15	1	0.5
0.15	0.3	0.2	0.1
0.3	0.35	0.25	0.2
0.1	0.75	0.6	0.25
0.8	0.4	0.9	0.35
0.7	0.2	0.85	0.25
0.95	0.9	0.8	0.65
0.6	0.65	0.75	0.85
0.65	0.7	0.7	0.9
0.35	0.85	0.7	0.65
0.6	0.85	0.75	0.1
0.9	0.8	0.75	0.35
		0.55	0.95

**Table 2. Maximum errors generated by 5 interpolation methods using the 33 node discretization in Test 1.**

Max Error -- max ( abs (Tinterp-Tbench) )	F1	F2	F3	F4	F5	F6
Nielson method (Nielson, 1979)	2.162E-02	1.346E-02	6.101E-03	1.882E-02	2.705E-03	8.498E-04
Combination method (Zhang and Cheng, 2002)	2.876E-02	8.342E-03	2.316E-03	4.704E-03	2.841E-04	2.253E-04
Interp2slope with exact nodal slopes	5.056E-01	8.617E-02	9.784E-03	5.617E-02	3.844E-01	2.684E-02
Interp2slope with approximated nodal slopes	8.100E-01	1.744E-01	5.109E-02	2.206E-01	7.996E-01	9.359E-02
Standard linear Finite Element interpolation	1.135E+00	1.920E-01	6.688E-02	3.983E-01	1.034E+00	2.825E-01

**Table 3. Maximum and RMS errors generated by 6 interpolation methods on a regularly spaced 11x11 node 2D coarse mesh (Test 2).**

Max Error -- max ( abs (Tinterp-Tbench) )	F1	F2	F3	F4	F5	F6	F7	F8
Interp2slope with exact nodal slopes	5.648E-02	1.190E-02	2.823E-05	5.324E-04	7.507E-03	9.492E-04	7.310E-02	8.255E-03
Interp2slope with approximated nodal slopes	2.077E-01	5.038E-02	2.391E-03	1.191E-02	4.931E-02	3.014E-02	1.445E-01	4.928E-02
Standard linear Finite Element interpolation	3.338E-01	7.017E-02	5.331E-03	4.224E-02	1.508E-01	4.389E-02	1.625E-01	7.741E-02
Matlab interp2.m with 'linear' option	3.523E-01	3.508E-02	4.641E-03	4.119E-02	1.363E-01	3.245E-02	1.470E-01	4.640E-02
Matlab interp2.m with 'cubic' option	1.696E-01	1.842E-02	1.230E-03	2.462E-03	2.493E-02	4.395E-03	9.936E-02	3.008E-02
Matlab griddata.m with 'cubic' option	2.094E-01	5.038E-02	3.327E-03	1.144E-02	4.408E-02	2.933E-02	1.491E-01	5.055E-02
RMS Error	F1	F2	F3	F4	F5	F6	F7	F8
Interp2slope with exact nodal slopes	3.703E-03	7.245E-04	7.623E-06	9.238E-05	7.776E-04	8.356E-05	8.295E-03	1.299E-03
Interp2slope with approximated nodal slopes	1.538E-02	2.872E-03	4.494E-04	1.875E-03	5.317E-03	3.703E-03	1.949E-02	7.811E-03
Standard linear Finite Element interpolation	4.565E-02	5.072E-03	1.508E-03	9.684E-03	1.925E-02	1.184E-02	2.706E-02	1.479E-02
Matlab interp2.m with 'linear' option	4.726E-02	4.603E-03	1.534E-03	9.412E-03	1.940E-02	1.168E-02	2.656E-02	1.474E-02
Matlab interp2.m with 'cubic' option	1.323E-02	1.800E-03	2.198E-04	6.680E-04	3.676E-03	6.733E-04	1.856E-02	5.561E-03
Matlab griddata.m with 'cubic' option	1.628E-02	3.664E-03	4.790E-04	1.815E-03	5.261E-03	3.447E-03	2.085E-02	7.721E-03

**Table 4. Maximum and RMS errors generated by 6 interpolation methods on a regularly spaced 21x21 node 2D coarse mesh (Test 2).**

21-by-21-node coarse mesh test case F1-F6 from (Zhang and Cheng, 2002)									
Max Error -- max ( abs (Tinterp-Tbench) )	F1	F2	F3	F4	F5	F6	F7	F8	
Interp2slope with exact nodal slopes	4.584E-03	1.742E-03	2.194E-06	3.434E-05	5.324E-04	9.451E-05	8.255E-03	8.644E-04	
Interp2slope with approximated nodal slopes	3.003E-02	1.294E-02	6.360E-04	2.457E-03	7.970E-03	8.322E-03	3.908E-02	9.658E-03	
Standard linear Finite Element interpolation	9.599E-02	1.974E-02	1.462E-03	1.087E-02	4.224E-02	1.311E-02	7.741E-02	2.316E-02	
Matlab interp2.m with 'linear' option	9.778E-02	9.869E-03	1.214E-03	1.080E-02	4.119E-02	9.349E-03	4.640E-02	1.223E-02	
Matlab interp2.m with 'cubic' option	1.845E-02	3.103E-03	1.433E-04	1.975E-04	2.220E-03	8.412E-04	1.923E-02	1.879E-03	
Matlab griddata.m with 'cubic' option	2.980E-02	1.294E-02	5.812E-04	2.521E-03	7.348E-03	8.508E-03	3.781E-02	9.658E-03	
RMS Error	F1	F2	F3	F4	F5	F6	F7	F8	
Interp2slope with exact nodal slopes	2.270E-04	7.746E-05	4.789E-07	5.848E-06	5.024E-05	5.370E-06	5.721E-04	7.844E-05	
Interp2slope with approximated nodal slopes	2.016E-03	5.411E-04	8.145E-05	2.682E-04	5.853E-04	6.756E-04	2.806E-03	9.128E-04	
Standard linear Finite Element interpolation	1.259E-02	1.498E-03	3.891E-04	2.450E-03	5.118E-03	2.974E-03	7.639E-03	3.749E-03	
Matlab interp2.m with 'linear' option	1.243E-02	1.248E-03	3.871E-04	2.425E-03	5.096E-03	2.964E-03	7.642E-03	3.853E-03	
Matlab interp2.m with 'cubic' option	1.119E-03	1.630E-04	1.697E-05	4.261E-05	2.594E-04	7.477E-05	2.257E-03	3.394E-04	
Matlab griddata.m with 'cubic' option	1.941E-03	5.051E-04	8.148E-05	2.758E-04	5.876E-04	6.758E-04	2.959E-03	9.348E-04	

**Table 5. Maximum and RMS errors generated by 5 interpolation methods on regularly spaced 11x11x11 and 21x21x21 node 3D meshes.**

11x11x11 coarse mesh

Max Error -- max ( abs (Tinterp-Tbench) )	F9	F10	F11	F12
Matlab 'interp3.m' with 'linear' option	1.708E-01	5.892E-02	6.063E-02	1.900E-01
Matlab 'interp3.m' with 'cubic' option	9.936E-02	3.008E-02	3.288E-03	3.541E-02
interp3slope with exact nodal slopes	1.129E-01	1.958E-02	1.153E-03	1.454E-02
Interp3slope with approximated nodal slopes	2.106E-01	6.097E-02	1.704E-02	9.059E-02
Standard linear Finite Element interpolation	2.824E-01	1.059E-01	6.166E-02	2.033E-01
RMS Error	F9	F10	F11	F12
Matlab 'interp3.m' with 'linear' option	1.929E-02	1.640E-02	9.592E-03	1.412E-02
Matlab 'interp3.m' with 'cubic' option	1.143E-02	5.207E-03	7.942E-04	2.840E-03
interp3slope with exact nodal slopes	8.061E-03	1.970E-03	1.676E-04	9.647E-04
Interp3slope with approximated nodal slopes	1.677E-02	9.976E-03	2.961E-03	5.795E-03
Standard linear Finite Element interpolation	2.317E-02	1.993E-02	1.127E-02	1.684E-02

21x21x21 coarse mesh

Max Error -- max ( abs (Tinterp-Tbench) )	F9	F10	F11	F12
Matlab 'interp3.m' with 'linear' option	5.892E-02	1.556E-02	1.612E-02	6.063E-02
Matlab 'interp3.m' with 'cubic' option	1.923E-02	1.902E-03	2.267E-04	3.288E-03
interp3slope with exact nodal slopes	1.958E-02	1.794E-03	7.654E-05	1.153E-03
Interp3slope with approximated nodal slopes	5.631E-02	1.329E-02	4.274E-03	1.727E-02
Standard linear Finite Element interpolation	1.059E-01	3.420E-02	1.619E-02	6.166E-02
RMS Error	F9	F10	F11	F12
Matlab 'interp3.m' with 'linear' option	6.050E-03	4.420E-03	2.501E-03	3.767E-03
Matlab 'interp3.m' with 'cubic' option	1.779E-03	4.819E-04	4.954E-05	2.036E-04
interp3slope with exact nodal slopes	7.147E-04	1.470E-04	1.108E-05	6.655E-05
Interp3slope with approximated nodal slopes	3.159E-03	1.451E-03	5.875E-04	9.496E-04
Standard linear Finite Element interpolation	7.280E-03	5.392E-03	2.953E-03	4.593E-03

**Table 6. Maximum errors generated by the 2D cspline methods on a mesh with 121 sample nodes shown in Fig. 16. This test has a similar number of fitting parameters to the Nielson-type interpolation methods shown in Table 1 and 2, and thus provides a fairer comparison of the relative accuracy of these different 2D interpolation techniques.**

121-node coarse mesh Max Error -- max ( abs (Tinterp-Tbench) )	F1	F2	F3	F4	F5	F6
Interp2slope with exact nodal slopes	1.925E-01	2.400E-02	9.837E-04	5.636E-03	3.975E-02	2.579E-03
Interp2slope with approximated nodal slopes	2.886E-01	9.264E-02	1.588E-02	3.177E-02	1.384E-01	3.910E-03

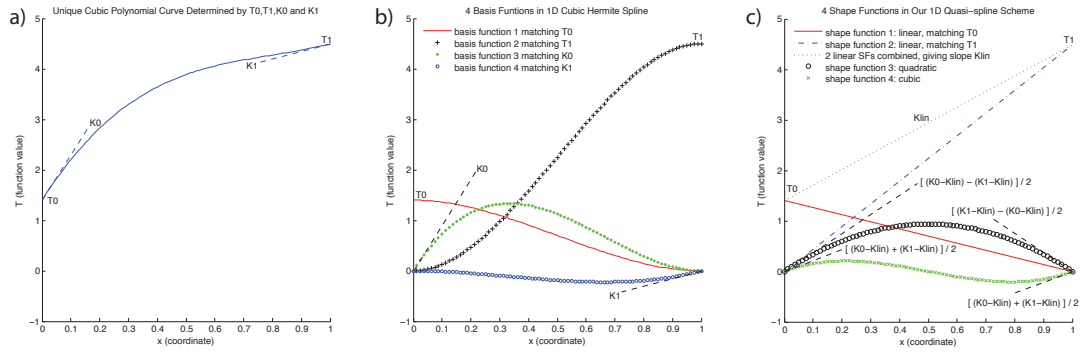


**Figure 1. Comparison of the standard cubic Hermite spline (cspline) and our quasi-cspline parameterization for 1D interpolation.** In 1D, the 2 different parameterizations lead to the same cubic polynomial function. a) Unique cubic curve determined by nodal values  $T_0$  at  $x=0$ ,  $T_1$  at  $x=1$  and nodal slopes  $K_0$  at  $x=0$ ,  $K_1$  at  $x=1$ . b) A cspline uses these 4 basis functions to fit the nodal values and slopes – each function fits 1 of the 4 constraints:  $T_0$ ,  $T_1$ ,  $K_0$  and  $K_1$ . c) Our quasi-cspline scheme uses a different set of finite-element-like shape functions to fit the same 4 constraints with the same cubic polynomial: 2 linear shape functions fit nodal values while introducing a linear background slope, quadratic and cubic shape functions fit the 2<sup>nd</sup> (mean slope deviation) and 3<sup>rd</sup> order (cubic correction to fit slopes exactly at the two interval ends) corrections to the linear background slope over this 1D interval. This results in the same cspline curve, but in a form better suited for finite-element bookkeeping techniques.

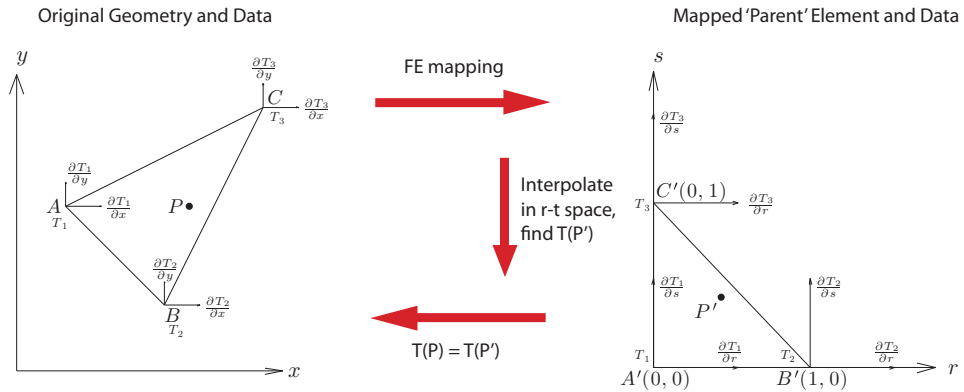


**Figure 2. General approach of our quasi-cspline scheme in 2D. Each triangle's nodal coordinates are mapped to a regular 'parent' element following standard FE approaches. Interpolation to fit nodal values and nodal slopes is then calculated within this regular parent element using the hierarchical shape functions shown in Figure 3.**

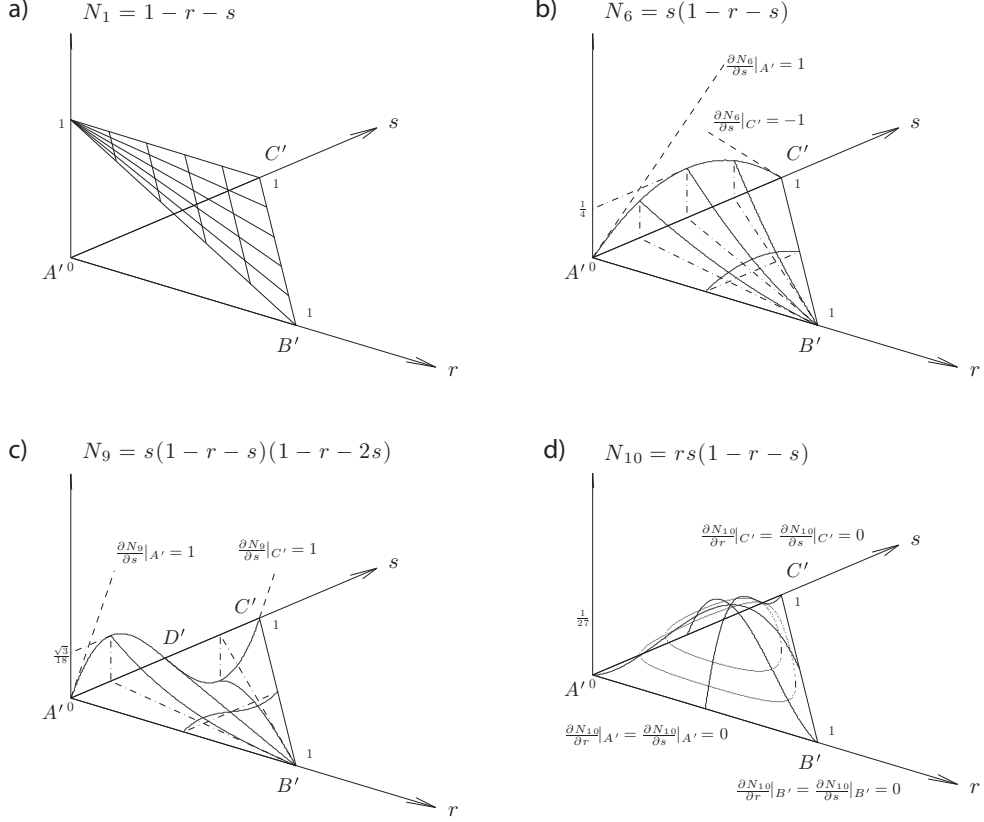
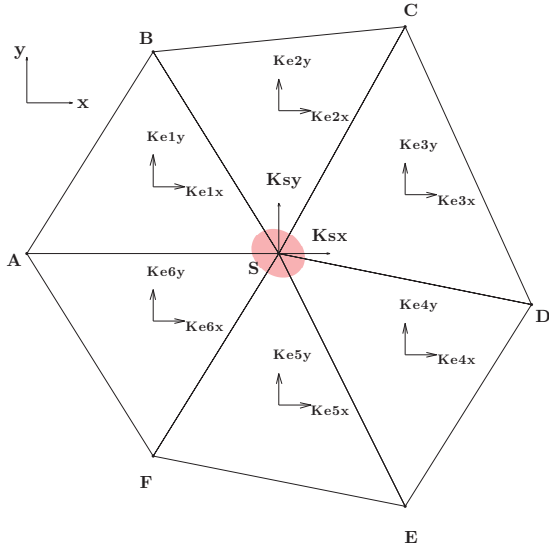


**Figure 3. Examples of 2D hierarchical shape functions in each of 4 subcategories:**  
**a)** linear shape function  $N_1$ . These shape functions match nodal values.  
**b)** quadratic shape function  $N_6$ . These shape functions match mean slope deviations along each edge of the triangle (same function as in 1D quasi-cspline parameterization in Figure 1.)  
**c)** cubic shape function  $N_9$ . These cubic shape functions add a cubic correction to fit slopes exactly at the two vertices of this element edge.,  
**d)** interior bubble function  $N_{10}$ . This bubble function does not affect nodal values or slopes, and can be used if a full cubic polynomial is desired, and there is extra information to constrain the bubble value. (See text for further discussion.)

a)



b)

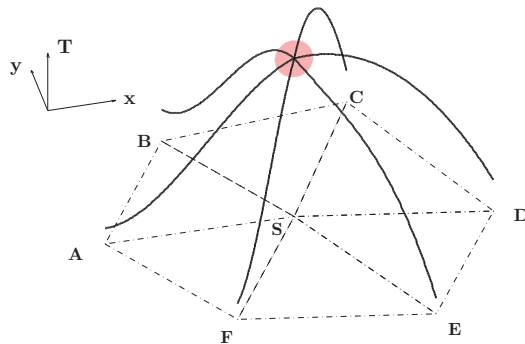


**Figure 4. a)** Sketch of the technique used to estimate smooth nodal slope information when only nodal values are given. Nodal slopes can be calculated as a weighted average of all linear slopes defined by the values at the vertices of the neighboring elements that share a given node. The black lines show element edges, the red ellipse shows the projection of a circular tangent disk with the resulting slope and the central node. **b)** The interpolated result around a given node has an ‘umbrella-skeleton’ structure along the edges of each triangle, as it is fitting a cspline along each triangle edge that matches the value  $T$  and slopes  $dT/dx$  and  $dT/dy$  at the node. Black lines show these edge csplines, and the red tangent disk is also shown.

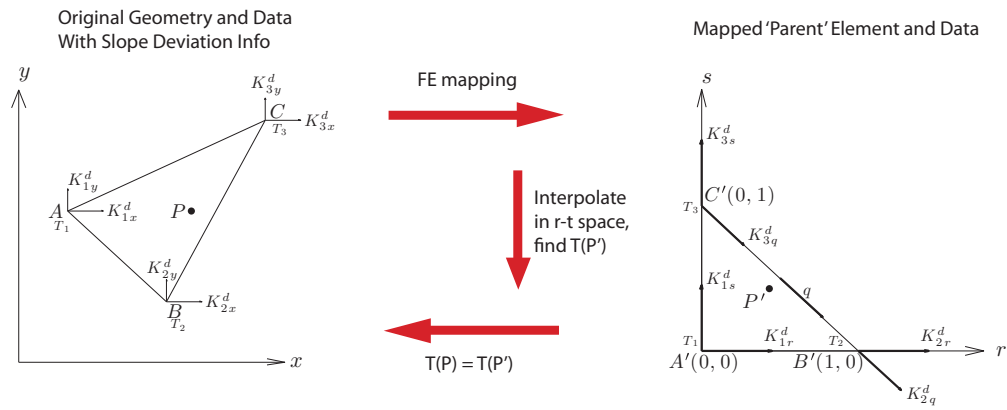


**Figure 5. Calculation steps for the quasi-cspline interpolation in 2D.** 1) Instead of mapping nodal slopes themselves, slope deviations (nodal slopes minus the linear background slopes) are mapped using the hierarchical shape functions in Figure 3; 2) these deviations are mapped to the *along-edge* directions at each node in the parent element space.

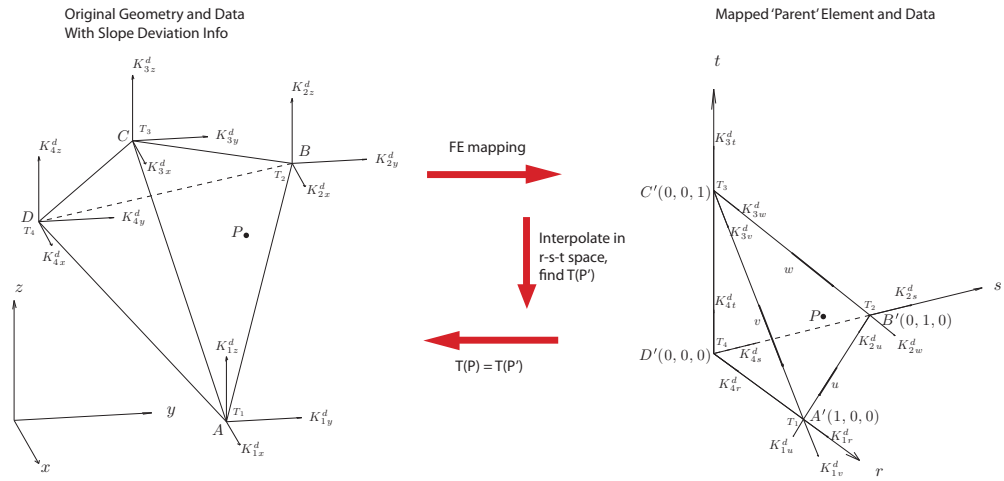


**Figure 6. Element geometry and calculation steps for the quasi-cspline scheme in 3D. All calculations are exactly analogous to the 2D quasi-cspline, with nodal values and slope deviations mapped to a parent tetrahedral element where the interpolation is done.**

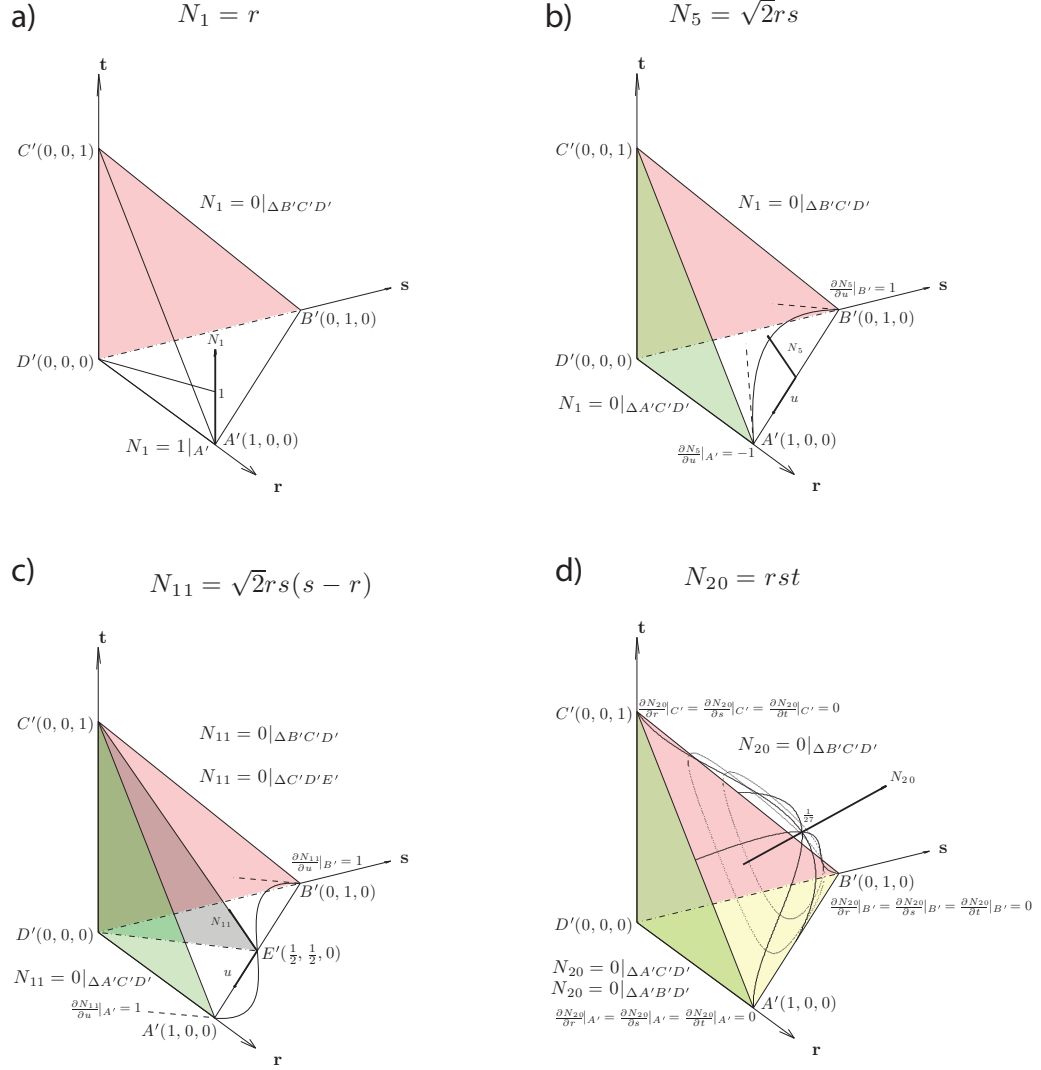


**Figure 7. Examples of 3D hierarchical shape functions in each of the 4 subcategories.** a) Linear shape function  $N_1$ . These shape functions match nodal values. b) Quadratic shape function  $N_5$ . These shape functions match mean slope deviations along each edge of the triangle (same function as in Figures 1 and 3). c) Cubic shape function  $N_{11}$ . These cubic shape functions add a cubic correction to fit slopes exactly at the two vertices of this element edge (same function as in Figures 1 and 3). d) Face bubble function  $N_{20}$ . These bubble functions do not affect nodal values or slopes, and can be used if a full cubic polynomial is desired, and there is extra information to constrain the bubble values. (See text for further discussion.)

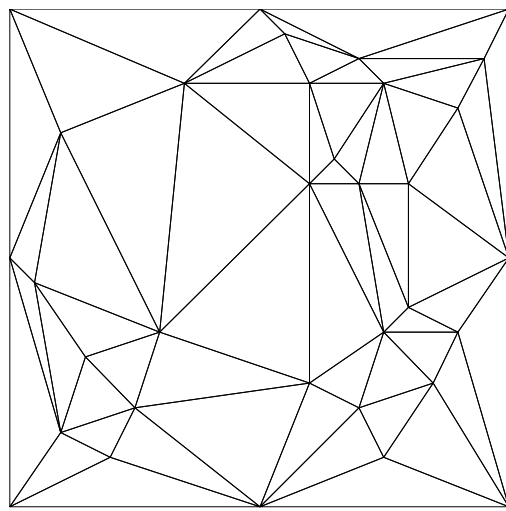


**Figure 8. Mesh used for test 1. Delaunay triangulation of 33 points provided in Table 1 by Franke (1979).**

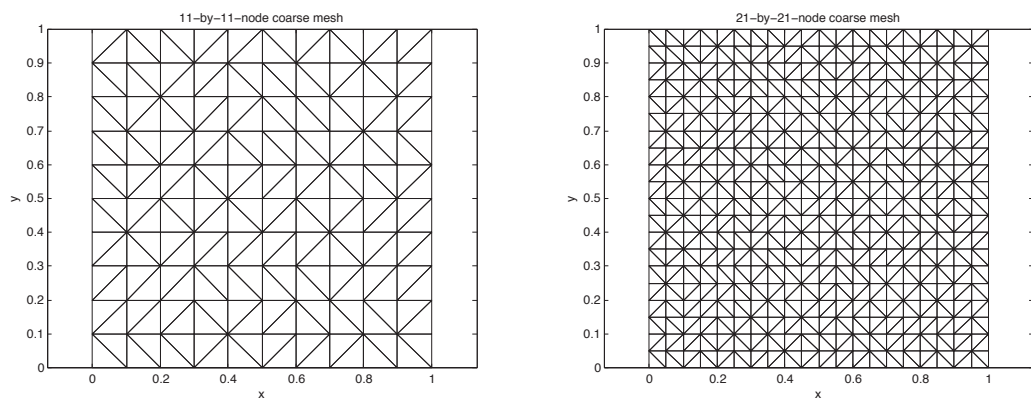


**Figure 9. Node locations and meshes used for test 2. Triangulations of the 11x11 and 21x21 node sets using Matlab command ‘DelaunayTri’. Notice that these 2 meshes can be used in 2 ways – either as structured rectangular meshes or unstructured triangular meshes.**

$$Super \ Gaussian : f(x) = A_0 \exp(-2|r/L|^n)$$

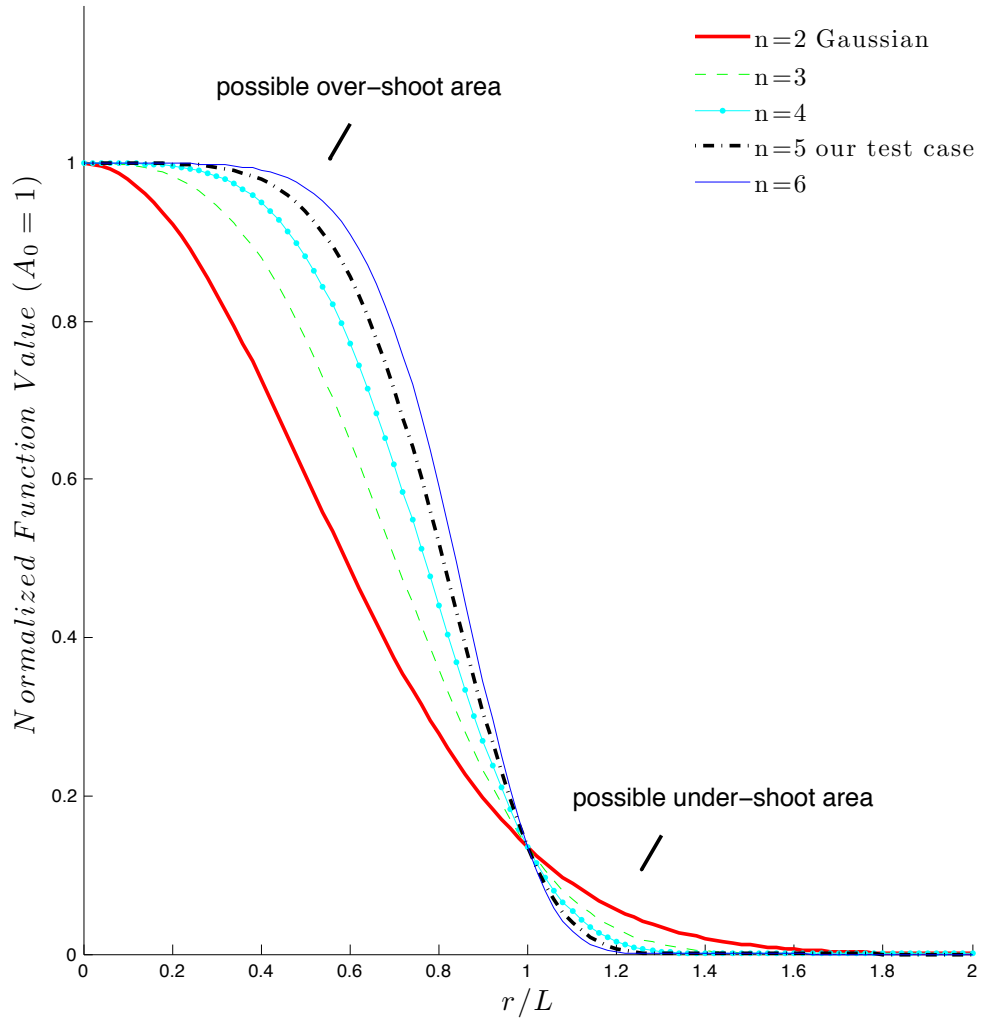


**Figure 10. Examples of 1D Super Gaussian functions for  $n=2-6$ .**

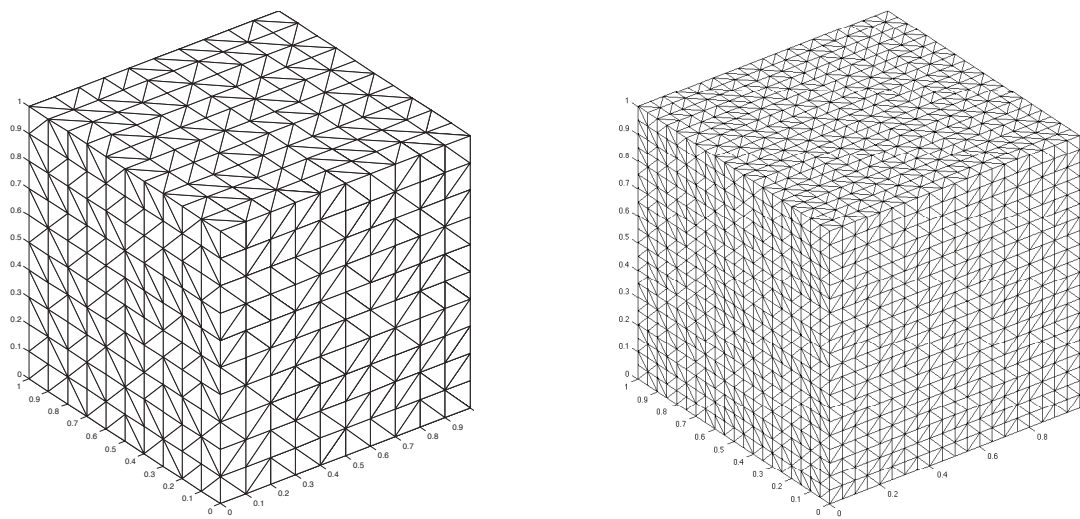


**Figure 11. Tetrahedral tessellations of the  $11 \times 11 \times 11$  and  $21 \times 21 \times 21$  node sets using the Matlab command ‘DelaunayTri’.** Notice that these 2 meshes can be used in 2 ways – either as structured brick meshes or unstructured tetrahedral meshes.

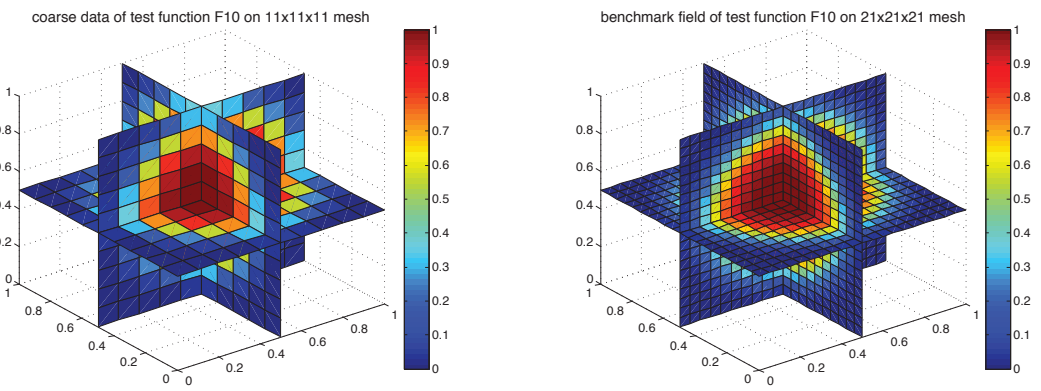


**Figure 12. Super Gaussian function  $F_{10}$  evaluated on 11x11x11 coarse mesh and 21x21x21 benchmark mesh.**

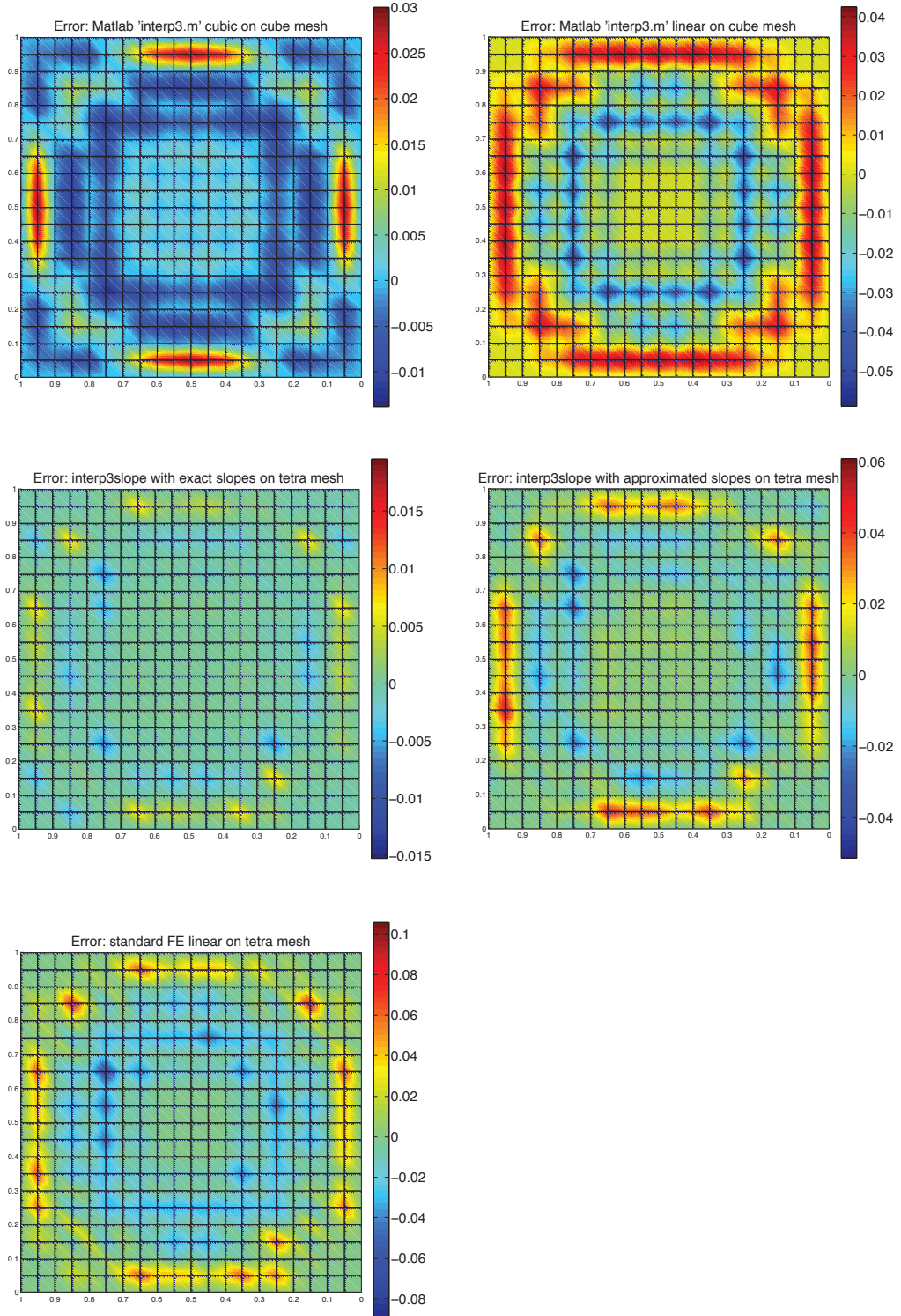


**Figure 13. Error distribution of  $F_{10}$  test case (Fig. 12) with the 5 different methods on plane  $y=0.5$ .**

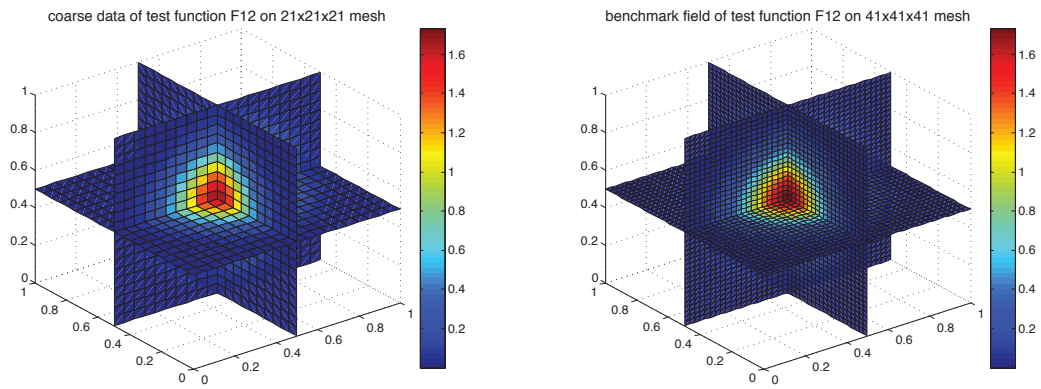


**Figure 14. Gaussian function  $F_{12}$  evaluated on the 21x21x21 coarse mesh and 41x41x41 benchmark mesh.**

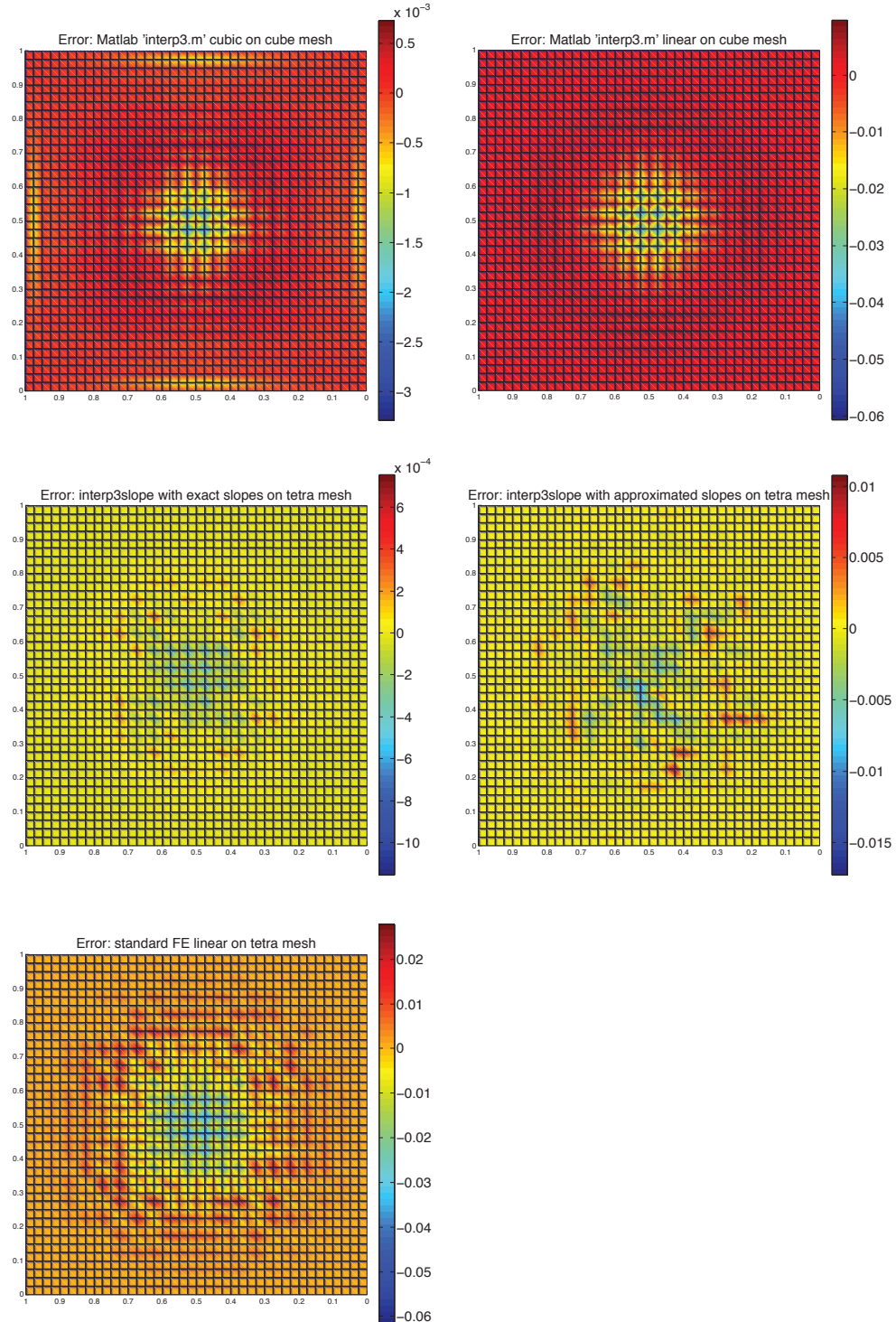


**Figure 15. Error distributions for the  $F_{12}$  test case (Fig. 14) with the 5 different methods on plane  $y=0.5$ .**

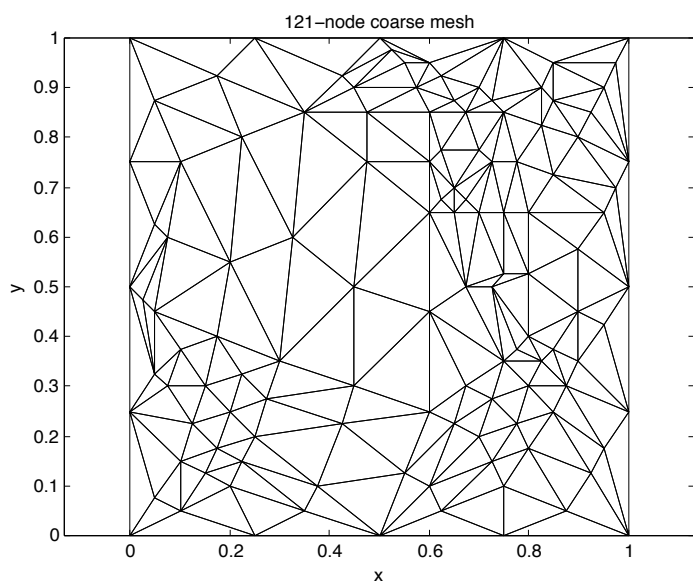


**Figure 16.** Triangulation of 121 points, this point set is generated by adding midside nodes to the 33 point triangulation (Franke, 1979) shown in Fig. 8, and making a Delaunay triangulation of this new set of 121 node points.

## CHAPTER 3

# Plume-asthenosphere-lithosphere Interactions Within a Mantle with a Plume-fed Asthenosphere: Implications for Iceland- and Hawaii-type Plume Dynamics

Chao Shi<sup>1</sup>, Jason Phipps Morgan<sup>1</sup>, and Jörg Hasenclever<sup>2</sup>

<sup>1</sup>Dept. of Earth and Atmospheric Sciences, Cornell University, Ithaca, NY

<sup>2</sup>Institute of Geophysics, Hamburg University, Hamburg, Germany

### ***Abstract***

We study the flow and temperature structures arising from on- and off-axis deep-mantle plumes within a convecting 3D mantle with thermal lithosphere and subducting slabs. The thermal plumes are assumed to have a temperature-dependent density and viscosity contrast with surrounding mantle, with thermal expansion controlling density and viscous creep governed by an Arrhenius-type temperature relation. The code used for these

experiments is a parallel Matlab+MPI-based 3D Finite Element code that we have developed, which works with unstructured tetrahedral meshes, and which can handle large and abrupt (up to 5 orders of magnitude) viscosity contrasts. We show the results for: 1) viable conditions (plume flux, density contrast, viscosity contrast) for the existence of a plume-fed asthenosphere system with an on/off-axis plume; 2) the resulting 3-D flow patterns in the asthenosphere and the dynamic topography at the surface and base of the asthenosphere associated with this flow; 3) the decoupling effect of a buoyant and less viscous asthenosphere layer for underlying mantle, and how this leads to stabler (more fixed) hot spot drift.

### ***Introduction***

The conventional view of Earth's mantle convection is that, it occurs in convection cells, with plates and slabs forming the cold top boundary layer of each cell; the asthenosphere is the region where temperature and pressure conditions result in the lowest viscosity region of the mantle, and a seismic Low Velocity Zone (LVZ) (Fig. 1a). We think this picture is too simple, and that a plume-fed asthenosphere (PFA) may form an important dynamic boundary layer beneath the plates, especially where the lithosphere is relatively thin in ocean basins. If the asthenosphere is fed by hot plumes from the deep mantle

(Fig. 1b), then it will be more buoyant and less viscous than its underlying mantle. This will lead to several dynamic effects: limited sub-slab asthenosphere entrainment; a pervasive counterflow pattern within the asthenosphere; broad asthenosphere decoupling of plates and deeper mantle except in the regions around subducting slabs and where thick cratonic roots may extend beneath the PFA; and dynamic links within the D"-plume-asthenosphere system (cf. Phipps Morgan et al., 1995a; Phipps Morgan et al., 2007; Yamamoto et al., 2007; Shi and Phipps Morgan, 2011 (CHAPTER 1)). A more realistic 3D view of this plume-fed asthenosphere concept underneath oceanic lithosphere is shown in Fig. 1c, which is based on boundary-layer-based numerical experiments in Yamamoto et al. (2007) and this study.

The asthenosphere is observed in seismic studies as a low-seismic-velocity (Dziewonski and Anderson, 1981) and high-attenuation (Widmer et al., 1991) zone between ~100-300km depths. It is now known to be widely distributed underneath oceanic lithosphere (e.g. Gaherty et al., 1999; Nettles and Dziewonski, 2008; Dalton et al., 2009). However, beneath the stable continental regions, seismic speeds are much faster, implying a much stronger mantle between ~80-250 km depth (Goes and van der Lee, 2002). The seismic Low Velocity Zone (LVZ) is also considered by most scientists as a lower viscosity zone, as an effect of competing temperature and pressure conditions at the shallowest mantle (Weertman and Weertman, 1975; Buck

and Parmentier, 1986; Karato and Wu, 1993). Furthermore, studies of oceanic plates and global stress distribution implies the existence of an asthenosphere with a viscosity of  $\sim 1E18\text{-}19$  Pa-s (Richter and McKenzie, 1978; Wiens and Stein, 1985; Ghosh et al, 2007), which is consistent with the viscosity estimates from glacier-rebound studies at Iceland (Sigmundsson and Einarsson, 1992) and other non-tectonic regions.

Several potential causal mechanisms have been proposed to explain the observed features of a shallow asthenosphere individually: the seismic LVZ is presumed to be due to the presence of partial melt in the asthenosphere but not deeper (Anderson, 1989; Hammond and Humphreys, 2000), or higher water content in the asthenosphere (Karato and Jung, 1998); the significant change in seismic attenuation between asthenosphere and underlying mantle is supposed to be related to a sharp increase in grain-size below the asthenosphere (Faul and Jackson, 2005); and the viscosity increase below the asthenosphere is proposed to be due to a change between dislocation creep within the asthenosphere and diffusion creep below the asthenosphere (Weertman and Weertman, 1975; Karato and Wu, 1993). However, all these observations can be more simply explained by the single unifying hypothesis that the plume-fed asthenosphere has a higher potential temperature than the underlying mesosphere.

We favor the Plume-fed Asthenosphere hypothesis that the asthenosphere forms and persists as a simple consequence of plume upwelling from deep mantle. Hot buoyant material rises until its ascent is stopped by overlying plates. It tends to ‘puddle’ beneath the lithosphere where it forms a persistent hot and low viscosity layer that can only be effectively removed by near-surface cooling and transformation into lithosphere. Because of its temperature dependent buoyancy and low viscosity, it will tend to float above the rest of the mantle, and is hard for subducting slabs to drag down at trenches (Phipps Morgan et al., 1995;2007; Shi and Phipps Morgan, 2011 (CHAPTER 1)).

In this paper, we first try to verify the 2D results (Shi and Phipps Morgan, 2011 (CHAPTER 1)) in 3D numerical experiments that have a truly internally consistent dynamic mantle plume rising from D''. For code verification purposes, our first experiments explore the geometry of a ridge-centered Iceland-type plume, later we also explore a model for an off-ridge-axis Hawaii-type plume. We will show the results of, 1) viable conditions (plume flux, density contrast, viscosity contrast) for the existence of a PFA system with an on/off-axis plume; 2) The resulting 3D flow patterns in the asthenosphere, with their associated dynamic topography at the surface and base of the asthenosphere; 3) The particular ‘plume bump’ in relief at the base of a

buoyant asthenosphere around the plume conduit that offers a possible explanation for the blue “fast halo” seen in the recent PLUME seismic experiment (Wolfe et al., 2009) -- this is further studied in Phipps Morgan et al. (2011); 4) the decoupling effect of a buoyant and less viscous asthenosphere layer for underlying mantle, and how this effect leads to relatively fixed hot spots.

### ***Numerical Method***

We use a parallel-Matlab-based Finite Element code on a 4-16core cluster: for the Stokes flow problem we use multigrid-preconditioned conjugate gradient Patera algorithm -- in each time step, we solve first for pressure and velocity, then update temperature; for temperature we use semi-Lagrange for advection, and Crank-Nicolson for diffusion -- in each time step, we let heat diffuse by solving a diffusion-only heat equation with finite elements (Hughes, 2000), then we utilize the velocity field to find the backtrack positions for all nodes, conduct a cubic interpolation (Shi and Phipps Morgan, 2011; Chapter 2) over the unstructured mesh for temperature on the backtrack positions, and then advect temperature profile in a semi-Lagrange fashion. Code techniques are described in more detail by Hasenclever (2010).

We utilize unstructured tetrahedral meshes with quadratic elements to discretize the spatial domain. This decision is made to focus computational power into regions which will highly affect the global flow pattern -- in an earlier study (Phipps Morgan et al., 2007), it was found that fine mesh in the slab-entrainment ‘sheet’ is very important for resolving the large scale pattern of counterflow within the asthenosphere. When the plate speed  $V$  is 100 km/Ma, viscosity of the asthenosphere  $\mu_{asth}$  is  $10^{19}$  Pa s, density contrast between the asthenosphere and its underlying mantle  $\Delta\rho_{asth}$  is  $\sim 320$  kg/m<sup>3</sup>, we estimate that the thickness of the asthenosphere entrainment sheet  $h$  is 20km, using the boundary layer theory-derived relation  $h = \sqrt{4\mu_{asth}V/\Delta\rho_{asth}g}$  (Phipps Morgan et al., 2007). This requires at least a 3-5km resolution within the entrainment sheet.

Density  $\rho$  and viscosity  $\mu$  are both temperature dependent in our code:  
 $\rho = \rho_0 [1 - \alpha(T - T_0)]$ , while  $\mu = \mu_0 \exp\{30[(T_0/T) - 1]\}$ , where the reference mantle density  $\rho_0 = 3300$  kg/m<sup>3</sup>, the reference mantle viscosity  $\mu_0 = 10^{21}$  Pa s, the ambient mantle potential temperature  $T_0 = 1200^\circ\text{C}$ , and the thermal expansion coefficient  $\alpha = 2.5\text{e-}5$ . Viscosity is lowered by 1 additional order of magnitude within the plume conduit to mimic possible (power-law) shear weakening, and also lowered to  $10^{18}$  Pa s near D” to create a weak,

asthenosphere-like boundary layer at the base of the convecting mantle. The question is: with these parameters, and with a plume potential temperature  $T \sim 1400^\circ\text{C}$  when it enters asthenosphere depth (this  $\sim 200^\circ\text{C}$  temperature difference is the measured temperature difference between suboceanic asthenosphere and underlying mantle in the (Cammarano and Romanowicz, 2007) for temperature structure in the upper mantle) in a previous 2D study we found there would be a dynamic but persistent plume-fed asthenosphere layer (Shi and Phipps Morgan, 2011 (CHAPTER 1)), can we obtain similar results in 3D experiments where the plume flux is not applied as a ‘boundary condition’ but instead a self-consistent outcome of the flow solution?

### ***On-ridge-axis Iceland-type Plume***

Our first set of numerical experiments focus on testing whether an average plume flux of  $\sim 1.2$  times as the slab flux – the flux we found sufficient to sustain a plume-fed asthenosphere in 2D (Shi and Phipps Morgan, 2008; Chapter 1) will lead to a persistent plume-fed asthenosphere layer within the convecting lithosphere/mantle system. Like in 2D, the 3D model takes into account plume supply, ridge accretion, lithosphere cooling with age, and well-resolved slab dragdown effects, all of which must be accurately approximated for a ‘brute-force’ numerical experiment to accurately assess this basic

question.

### *On-axis Plume Model Setup: Model Geometry, Boundary Conditions and Mesh*

The model geometry is illustrated in Fig. 2. The model domain is a 12000 km x 3000 km x 1000 km region, e.g. the trench-to-trench distance is 12000 km, the mantle thickness is 3000 km, and the trench length is 1000 km. We chose this “1 plume per 1000 km trench” scenario using the following back-of-envelope estimation: assuming a trench subduction rate (map area)  $2.5 \text{ km}^2 / \text{yr}$ , and typical subduction velocity 100 mm/yr, we arrive at 25000 km total length of subducting trench for an Earth-like rate of plate subduction; if we take the conventional estimate that there are roughly  $\sim 25$  strong upwelling plumes in the mantle then each average plume feeds 1000 km of plate subduction.

In these experiments, we induce a ridge-centered mantle plume to form at the hot base of the mantle by prescribing temperature boundary conditions at the plume’s base. Because density and viscosity are both temperature dependent, a hot region at the base of the mantle naturally produces upwelling due to buoyancy effects, and lower viscosity increases the speed of plume flow. At the surface, oceanic lithosphere moves in both directions away from the ridge,

consuming asthenosphere to make new lithosphere and dragging underlying material to the trench where subducting slabs try to drag asthenosphere material into deep mantle (Fig. 2). We take advantage of problem symmetries when modeling the effects of a ridge-centered plume. This allows us to use only 1/4 the elements needed to resolve a high-resolution plume at an arbitrary point inside the box, i.e. we only mesh and solve for the green region in Fig. 2 – a 6000 km x 3000 km x 500 km box.

Boundary conditions: on the top boundary, the horizontal velocity boundary condition simulates a plate moving at a speed of 100 km/Ma, and the vertical velocity boundary condition is used to simulate the consumption of asthenosphere into the growing lithosphere (Fig. 3). This is calculated from the thickness of oceanic lithosphere and the plate velocity (100 km/Ma), which is a combination of thermal and compositional lithosphere (Yale and Phipps Morgan, 1998). The lithospheric slab is then subducted back into the domain with a temperature profile calculated using the half-space cooling solution for a lithospheric thermal boundary layer of appropriate plate age (Turcotte and Schubert, 2002). Material flux out of the box through the ridge and lithosphere base to ‘grow’ lithosphere is completely balanced by flux into the box through the ‘slab’. All the rest of the domain boundary has symmetry boundary conditions, so that the plume-plate-slab system is the only factor moving mass and heat through the computational domain.

The tetrahedral mesh shown in Fig. 4 is generated by GiD, and used to model the velocity and temperature field in asthenosphere and mantle. It covers a 6000 km x 3000 km x 500 km model space, which represents the green region in Fig. 2. Our goal is to obtain sufficiently high resolution in the asthenosphere, the slab-entrainment ‘sheet’ (the thin asthenosphere layer which goes down alongside the slab), and the D” layer by having a fine mesh in these regions. Therefore mesh resolution varies in different regions from ~3.7km near the ridge and within the asthenosphere entrainment sheet to ~500 km in the middle of the mantle where only broad background flow patterns arise.

#### *On-axis Plume Model Results*

Fig. 5 is a snapshot in a run started with pre-existing plume and asthenosphere at 50 Ma model time. This figure shows the results of several initial numerical experiments. It is encouraging that the same form of asthenosphere flow seen in the 2D experiments (Shi and Phipps Morgan, 2011 (CHAPTER 1)), with prescribed plume fluxes, is also evident in these 3D experiments with a naturally evolving plume flux.

A ridge-oriented view of the computational domain is shown in Fig. 5a, with 2 temperature isosurfaces highlighted: 1280°C (green) and 1320°C (orange). These isosurfaces outline the general geometry of a plume-fed asthenosphere. We observe that ‘bumps’ related to dynamic isostasy are generated both at the plume and trench. The plume bump can be used to explain the fast arrival ring-like structure in Wolfe et al. (2009), and will be further discussed later in this paper, as well as in Phipps Morgan et al. (2011). Fig. 5b provides another view of the plume-fed asthenosphere, with streamlines highlighting the flow field within the plume and asthenosphere, color meaning speed. Because of low viscosity within the asthenosphere, instead of only ridge-perpendicular flow, the plume fills in the near-ridge side of the asthenosphere with radial flow. The streamlines turn more parallel to plate motion when further away from the plume entrance, and finally a counterflow is seen near trench. Fig. 5c shows temperature contours over the whole volume of our domain, while a clear plume-fed asthenosphere system is seen. We find that with modal parameters described previously, plume feeding and buoyant asthenosphere counterflow keeps the asthenosphere ~200°C warmer than underlying mantle, consistent with a recent seismic+mineral physics-based estimate for the upper mantle geotherm in suboceanic regions (Cammarano and Romanowicz, 2007). Fig. 5d shows speed contours over the whole volume, we see mantle flow slowing down when shielded from plate motion by a weak asthenosphere. Subasthenospheric mantle only ‘feels’ the effects of

surface plate motions where the subducting slab penetrates below the asthenosphere. In this experiment, we see that the asthenosphere is acting as a decoupling layer between lithosphere and subasthenospheric mantle. (By analogy, plate motions could also couple to mantle flow where continental cratons extended below much of the buoyant asthenosphere layer)

### ***Off-ridge-axis Hawaii-type Plume***

We have shown in the previous section that similar plume-fed asthenosphere behavior with a ridge-centered plume seen in 2D experiments also exists in 3D. Next we explore a situation where the plume is away from the ridge axis – a ‘Hawaii-type’ plume setting. We chose to move onto this scenario not only because off-axis plumes are common on Earth, but also because in the previous on-axis model the plume was fixed at a corner of the computational domain to take advantage of symmetry boundary conditions. We would like to move the plume base away from corners and corner related boundary conditions to more realistically study how the plume conduit can be ‘deformed’ by motion of its surrounding ambient convecting mantle, but the ridge-symmetry boundary conditions also force the plume to stay along the intersection of the two planes of symmetry in the computational domain. This different boundary condition lets us explore a key issue about plume

dynamics: how fixed are plume upwelling structures with respect to deep mantle flow, and why? We also examine the other questions that arose in the ridge-centered experiments, e.g. what is the flux/temperature distribution within a plume conduit, under what conditions does a plume-fed asthenosphere arise as a flow structure within a numerical experiment with well-resolved plume and slab-entrainment boundary layers, what is the dynamic relief at the base of the asthenosphere around a plume, etc.

#### *Off-axis Plume Model Setup: Model Geometry, Boundary Conditions and Mesh*

The modal geometry is very similar to what is shown in Fig. 2 for the on-axis plume case, the only difference being that the plume is moved away from the ridge axis. This translates to a one-symmetry plane geometry with a plume on each side of the ridge in Fig. 2, and the green box computational region now contains half a potential plume conduit, instead of only a quarter of a plume. The other boundary conditions are kept the same except that the heating region is moved from a corner of the base to the center of the base beneath the plume conduit. This way a buoyant upwelling would initiate in the middle of the base, forming an off-ridge Hawaii-type plume structure. The tetrahedral mesh for this off-axis plume case is shown in Fig. 6, in both a front and back view. The fine mesh region for the plume conduit is now moved from around a

corner edge to the middle of the front side of the meshing domain.

### *Off-axis Plume Model Results*

Fig. 7 is a 30 Ma snapshot started from pre-existing plume and asthenosphere, which shows the general results of the off-ridge Hawaii-type plume experiment. Fig. 7a provides a ridge perspective of the temperature field in our off-ridge plume run, with 2D temperature profiles plotted on back (plume-axis-cutting) and left (trench-side) walls, and a 1350°C isosurface highlighted throughout the 3D space. The isosurface shows the general geometry of the base of the plume-fed asthenosphere. Similar to the on-axis case, plume feeding and counterflow of buoyant asthenosphere keeps the asthenosphere ~200°C warmer than underlying mantle. Here too ‘bumps’ related to dynamic isostasy are again generated around both the plume and subducting slab. Fig. 7b shows the velocity field on the left (trench-side) wall, back (plume-axis-cutting) wall and base ( $D''$ ) wall: color shows speed, arrows only show flow direction -- their length is uniform. A semi-transparent isosurface of  $T=1350^\circ\text{C}$  outlines the base of the asthenosphere. Focusing on the directions of the flow field, we see that: the plume joins the asthenosphere with radial flow; topmost material is dragged by plate motion, yet flow 50 km shallower than the LAB can move freely against plate motion and eventually

reach the ridge; a counterflow is seen near trench. Focusing on the speed of flow alone, we find that: high flow speeds are seen within plume conduit, D” layer, asthenosphere and slab; while mantle flow slows down when shielded from plate motion by a weak asthenosphere. This again highlights the decoupling effect of the asthenosphere layer for underlying mantle flow – in essence suboceanic mantle below asthenosphere depths ‘feels’ the effects of subducting slabs, but is isolated from the effects of overlying plate motions. Fig. 7c shows the trench-perpendicular velocity field  $U_x$ . Here a warm color means flow is moving towards the trench, while cold colors mean flow is moving towards the ridge, with light green to light yellow colors indicating nearly stationary mantle. Here it is more evident that plume material can flow relatively freely to all directions in the asthenosphere, due to its low viscosity, plume material can feed all the way towards ridge and trench. The color switches from green to yellow around the plume conduit, this means that in this scenario, the plume conduit is almost a stable feature in an actively convecting mantle. This result shows that: with a weak decoupling asthenosphere layer, hot spots can remain almost ‘fixed’ within an actively convecting mantle.

### ***Discussion***

### *High Flux in the Central (Hottest) Part of the Plume Conduit, Pulsing Plume*

In the off-ridge-axis plume model, we measure the plume flux in the plume conduit and in the subduction zone. Fig. 8a shows plume temperature cross-section at  $z = -2500$  km, near the plume base. The 3D surface map and the 2D contour map underneath show the same dataset. The ambient mantle is at  $1200^\circ\text{C}$ , while the hottest part of plume is  $\sim 1480^\circ\text{C}$ . This temperature profile is associated with a 3 orders of magnitude change of viscosity, which leads to very high plume upwelling speeds in the center part of the plume, shown in Fig. 8b. In panel (b), we show plume upwelling speeds on a cross-section at  $z = -2500$  km. Like panel (a), the 3D surface map and the 2D contour map on panel (b) plot the same dataset. We see very high upwelling speeds in the central (hottest) part of the plume cross-section because it is both the most buoyant and least viscous part. The viscosity in this cross-section ranges from  $10^{18}\text{ Pa s}$  (plume axis) to  $10^{21}\text{ Pa s}$  (ambient mantle). The upwelling speed in the center of the conduit can be as high as  $4000\text{ km/Ma}$ . Notice that this speed is much higher than typical rates of plate motion and/or slab subduction. This experiment shows that even if the observed plume stem is thin, a very high upwelling flux can occur within the plume conduit, due to the buoyancy and low viscosity near the axial region of the plume. A more detailed plot shows the plume flux contribution from each temperature band (Fig. 8c). Because of the very high speed near the center line of the plume, the central region with

less than  $\frac{1}{4}$  of the plume's cross-sectional area accounts for more than half of the upwelling flux. A comparison of upwelling plume flux (red) vs. downgoing slab with asthenospheric entrainment sheet flux (blue) is shown in Fig. 8d. In this run, we adjust the plume base temperature and heating area so that the upwelling and downgoing flux are almost equal so that there is a quasi-stable plume-fed asthenosphere (we do not directly set plume upwelling speed, rather it is an outcome of the experiment). However, at their onset, the 2 fluxes are not stable. Instead there is clear evidence of a naturally pulsing plume in this experiment; even when the plume base temperature and heating region are constant, the plume flux, and to a much smaller degree the downward slab-related flow both pulse with a timescale of  $\sim 1.2$  Myr. While more experiments are needed to quantify what process(es) control this frequency, we have qualitatively observed from a few partial numerical experiments that this pulsing arises as the plume conduit tries to 'adjust' its width in response to a sharp change in plume flux, and that a primary control on frequency is the viscosity of the lower mantle surrounding the conduit.

#### *Detailed PFA System Dynamics and Temperature Structure*

To better reveal the dynamics and temperature structure in the PFA system generated by the off-ridge-axis plume, we track particle movement and generate flow lines, and plot them on top of several temperature isosurfaces

(Fig. 9). In panels (a) and (b), temperature profile is shown as colored isotherms from 1350°C to 1470°C, while streamlines show the 3D flow pattern in the plume-fed asthenosphere system. Hotter axial material in the plume tends to rise to shallower depths where it is more strongly dragged by the overriding plate. Cooler material from the rim of plume enters into deeper parts of asthenosphere, where it can flow to either ridge or trench. Particles following plume-trench-D"-plume route have the shortest geological residence time in mantle (<100s of Ma); the plume-ridge-D"-plume route holds a much longer geological residence time; particles located in the regions without flow lines would be almost ‘stuck’ in mantle. Of course the natural motion migration of subduction zones with time will reduce this effect, but the idealized experiment clearly shows that there are likely to be several different ‘residence times’ within whole mantle convection with a plume-fed asthenosphere. It is interesting that plume material rises all the way from deep mantle at a very high speed (Fig. 7-8), but without mixing (flow lines within conduit are all parallel). Natural buoyancy stratification occurs immediately when hot material enters the asthenosphere.

### *Plume Bump and Dynamic Topography*

When zooming into the plume entrance (Fig. 9c), we find that the flow field is linked to a dynamic ‘bump’ in the relief at the base of the buoyant

asthenosphere. We can reinterpret the PLUME (Wolfe et al., 2009) inversion for lateral seismic variations beneath Hawaii with the dynamic plume bump relief at the base of a buoyant asthenosphere. Fig. 10a is taken from PLUME Vs structure beneath Hawaii (300-km-depth of their Fig 2.) A similar pattern is found between 100-400 km depths. A slow Vs plume conduit is seen between 100-1200 km depths. These results suggest a deep penetrating Hawaii plume, yet it is intriguing that there is a blue fast Vs halo around the red slow Vs region. It is impossible to explain this as a thermal halo around the plume; this should lead to a slow wavespeed halo, not a fast one (Fig. 10d). However, if the asthenosphere is plume-fed, hence more buoyant than underlying mantle, there is a simple explanation for this pattern. The anomaly would be due to faster travel times resulting from dynamic topography at the asthenosphere-mesosphere interface; uplift of the denser mesosphere by the buoyancy of the rising plume increases the distance a wave travels through faster mantle and reduces the distance though the slower asthenosphere (Fig. 10e). This effect will only happen if the asthenosphere is more buoyant than underlying mantle, in other words if there is a plume-fed asthenosphere.

Fig. 10b shows the PLUME anomaly recovered using a procedure that tried to force as much travel-time anomaly as possible into structure between 50-250 km depths (their Fig. S9b). We use these wave speed variations to estimate amplitude of the dynamic ‘bump’ at base of a plume-fed

asthenosphere. With the plume bump interpretation shown in Fig. 10e, the inference of a ~40-70 km high-~200 km-wide ‘bump’ of uplift of the base of the PFA can be directly estimated from PLUME results and the assumption of a ~6-10% reduction in shear velocity between the PFA and underlying mantle (Fig. 10f). This is consistent with the plume bump in the off-ridge-axis Hawaii-type plume model (Fig. 10c): on the 1350°C isosurface, a plume bump of ~60 km is generated at the asthenosphere entrance of a ~150-km-diameter plume. This effect is further studied in Phipps Morgan et al. (2011).

The PFA model also appears to provide a possible explanation for several additional recent observations: 1) The underside reflections from a ~250-350km-deep reflector in ocean basins (Cao et al., 2010) lies right around the bottom of the asthenospheric counterflow, which would produce a strong sense of shear, as well as a relatively sharp temperature change. 2) the 200 degree hotter-than-underlying-mantle suboceanic asthenosphere (Cammarano and Romanowicz, 2007) would naturally lead to low seismic wavespeeds and high attenuation (Faul and Jackson, 2005).

These numerical experiments clearly demonstrate that the asthenosphere can remain as a persistent hotter-than-average region of the mantle if it is fed by observed mantle-penetrating plumes (Montelli et al. 2004, Wolfe et al., 2009) at a rate comparable to its rate of removal by lithosphere accretion and

subduction. Clearly more experiments of this type will be needed to better quantify this mode of mantle flow, and to determine how it would look in a more realistic spherical Earth with migrating subducting zones, potentially time-variable plumes, and continental cratons. However these experiments show that it is possible to resolve these effects on a relatively small parallel compute-cluster, which means we should now be able to make much faster progress in exploring these questions.

## References

- Anderson, D.L., 1989. Theory of the Earth, Blackwell Scientific Publications.
- Brodholt, J.P., Helffrich, G. and Trampert, J., 2007. Chemical versus thermal heterogeneity in the lower mantle: The most likely role of anelasticity, *Earth Planet. Sci. Lett.*, 262, 429-437.
- Buck, W.R. and Parmentier, E.M., 1986. Convection beneath young oceanic lithosphere: Implications for thermal structure and gravity. *J. Geophys. Res.*, 91, 1961–1974.
- Cao, Q., Wang, P., van der Hilst, R.D., de Hoop, M. and Shim, S.-H., 2010. Imaging the upper mantle transition zone with a generalized Radon transform of SS precursors, *Physics of Earth and Planetary Interiors*, 180, 80-91.
- Cadek, O., and Fleitout, L., 2006. Effect of lateral viscosity variations in the core-mantle boundary region on predictions of the long-wavelength geoid, *Stud. Geophys. Geod.*, 50(2), 217-232.
- Cammarano, F. and Romanowicz, B., 2007. Insights into the nature of the transition zone from physically constrained inversion of long-period seismic data, *PNAS-High Pressure Geoscience*, 104, 9139-9144.
- CIMNE, 2011. GiD, International Center for Numerical Methods in Engineering, <http://gid.cimne.upc.es/>.
- Dabrowski, M., Krotkiewski, M. and Schmid, D.W., 2008. MILAMIN: MATLAB-based finite element method solver for large problems, *Geochem. Geophys. Geosyst.*, 9, Q04030
- Dalton, C.A., Ekström, G. and Dziewonski, A.M., 2009. Global seismological shear velocity and attenuation: A comparison with experimental observations, *Earth Planet. Sci. Lett.*, 284, 65-75.
- Davies, D.R., Davies, J.H., Hassan, O., Morgan, K. & Nithiarasu, P., 2008. Adaptive finite element methods in geodynamics; Convection dominated mid-ocean ridge and subduction zone simulations. *Int. J. Num. Meth. Heat Fluid Flow*, 7-8, 1015-1035,
- Dziewonski, A. and Anderson, D.L., 1981. Preliminary reference Earth model. *Phys. Earth Planet. In.*, 25, 297–356.
- Gaherty, J.B., Kato, M. and Jordan, T.H., 1999. Seismological structure of the up- per mantle: a regional comparison of seismic layering. *Phys. Earth Planet. In.*, 110, 21–41.

Ghosh, A., Wen, L., Holt, W.E., Haines, A.J. and Flesch, L.M., 2007. A best-fit lithosphere-mantle coupling model constrained by plate motions and the velocity gradient tensor field in the plate boundary zones, EOS Trans. AGU, 88(52), Fall Meet. Suppl., Abstract T21B-0582.

Goes, S. and van der Lee, S., 2002. Thermal structure of the North American uppermost mantle inferred from seismic tomography. *J. Geophys. Res.*, 107, ETG2-1–ETG2-13.

Hammond, W.C. and Humphreys, E.D., 2000. Upper mantle seismic wave velocity: effects of realistic partial melt geometries. *J. Geophys. Res.*, 105, 10975–10986.

Hasenclever, J., 2010. Modeling Mantle Flow and Melting Processes at Mid-Ocean Ridges and Subduction Zones - Development and Application of Numerical Models. Ph.D. Thesis.

Hughes, T.J.R., 2000. *The Finite Element Method: linear static and dynamic Finite Element Analysis*, Dover Publications, Inc.

Karato, S.-I. and Wu, P., 1993. Rheology of the upper mantle: a synthesis. *Science*, 260, 771–778.

Karato, S.-I. and Jung, H., 1998. Water, partial melting and the origin of the seismic low velocity and high attenuation zone in the upper mantle. *Earth Planet. Sci. Lett.*, 157, 193–207.

Long, M. D., 2009, Complex anisotropy in D<sub>II</sub> beneath the eastern Pacific from SKS–SKKS splitting discrepancies, *Earth Planet. Sci. Lett.*, 283, 181-189.

Montelli, R., Nolet, G., Dahlen, F.A., Master, G., Engdahl, E.R. and Hung, S.-H., 2004. Finite-frequency tomography reveals a variety of plumes in the mantle, *Science*, 303, 338-343.

Nettles, M. and Dziewonski, A.M., 2008. Radially anisotropic shear velocity structure of the upper mantle globally and beneath North America, *J. Geophys. Res.*, 113, B02303.

Oxburgh, E.R., Parmentier, E.M., 1977. Compositional and density stratification in oceanic lithosphere-causes and consequences, *Journal of the Geological Society*, 133, 343-355

Persson, P.-O., Strang, G., 2004. A simple mesh generator in MATLAB. *SIAM Review*, 46(2), 329-345.

Phipps Morgan, J., Morgan, W.J., Zhang, Y.-S. and Smith, W.H.F., 1995a.

Observational hints for a plume-fed sub- oceanic asthenosphere and its role in mantle convection. *J. Geophys. Res.*, 100, 12753–12768.

Phipps Morgan, J., Morgan, W.J. and Price, E., 1995b. Hotspot melting generates both hotspot volcanism and a hotspot swell? *J. Geophys. Res.*, 100, 8045–8062.

Phipps Morgan, J., 1997. The generation of a compositional lithosphere by mid-ocean ridge melting and its effect on subsequent off-axis hotspot upwelling and melting. *Earth Planet. Sci. Lett.*, 146, 213–232.

Phipps Morgan, J. and Morgan, W.J., 1999. Two-stage melting and the geochemical evolution of the mantle: A recipe for mantle plum-pudding. *Earth Planet. Sci. Lett.*, 170, 215–239.

Phipps Morgan, J., Hasenclever, J., Hort, M., Rüpke, L. and Parmentier, E. M., 2007. On subducting slab entrainment of buoyant asthenosphere. *Terra Nova*, 19: 167–173.

Phipps Morgan, J., Shi, C., Hasenclever, J., 2011. New Observational and Experimental Evidence for a Plume-Fed Asthenosphere Boundary Layer in Mantle Convection, *Earth Planet. Sci. Lett.*, *submitted*.

Richter, F.M. and McKenzie, D., 1978. Simple plate models of mantle convection. *J. Geophys.*, 44, 441–471.

Sigmundsson, F. and Einarsson, P., 1992. Glacio-isostatic crustal movements caused by historical volume change of the Vatnajokull ice cap. *Geophys. Res. Lett.*, 19, 2123–2126.

Shi, C., Phipps Morgan, J., 2009. Plume-fed Asthenosphere: a possible origin for 250–350km deep seismic reflectors?, *Eos Trans. AGU*, 90(52), Fall Meet. Suppl., Abstract DI13A-1647.

Shi, C., Phipps Morgan, J., Hasenclever, J., 2011. Plume-asthenosphere-lithosphere interactions within a mantle with a Plume-fed Asthenosphere: implications for Hawaii- and Iceland-type plume dynamics, *in prep*

Thoraval, C., Machetel, P. and Cazenave, A., 1995, Locally layered convection inferred from dynamic models of the Earth's mantle, *Nature*, 375.

Turcotte, D. L. and Schubert, G., 2002, *Geodynamics*, 2<sup>nd</sup> Ed., Cambridge University Press.

Weertman, J. and Weertman, J.R., 1975. High temperature creep of rock and mantle viscosity. *Annu. Rev. Earth Planet. Sci.*, 3, 293–315.

- Widmer, R., Masters, G. and Gilbert, F., 1991. Spherically symmetric attenuation within the Earth from normal mode data. *Geophys. J. Int.*, 104, 541–553.
- Wiens, D.A. and Stein, S., 1985. Implications of oceanic intraplate seismicity for plate stresses, driving forces, and rheology. *Tectonophysics*, 116, 143–162.
- Wolfe, C.J., Solomon, S.C., Laske, G., Collins, J.A., Detrick, R.S., Orcutt, J.A., Bercovici, D. and Hauri, E.H., 2009. Mantle shear-wave velocity structure beneath the Hawaiian hot spot, *Science*, 326, 1388-1390.
- Yale, M. and Phipps Morgan, J., 1998, Asthenosphere flow model of hotspot–ridge interactions: a comparison of Iceland and Kerguelen, *Earth Planet. Sci. Lett.*, 161, 1-4, 45-56.
- Yamamoto, M., Phipps Morgan, J. and Morgan, W.J., 2007a. Global plume-fed asthenosphere flow—I: Motivation and model development, *Geological Society of America Special Papers*, 430, 165-188.
- Yamamoto, M., Phipps Morgan, J. and Morgan, W.J., 2007b. Global plume-fed asthenosphere flow—II: Application to the geochemical segmentation of mid-ocean ridges, *Geological Society of America Special Papers*, 430, 189-208.
- Zienkiewicz, O.C. and Taylor, R.L., 2000. *The Finite Element Method*, 5th Ed., Elsevier

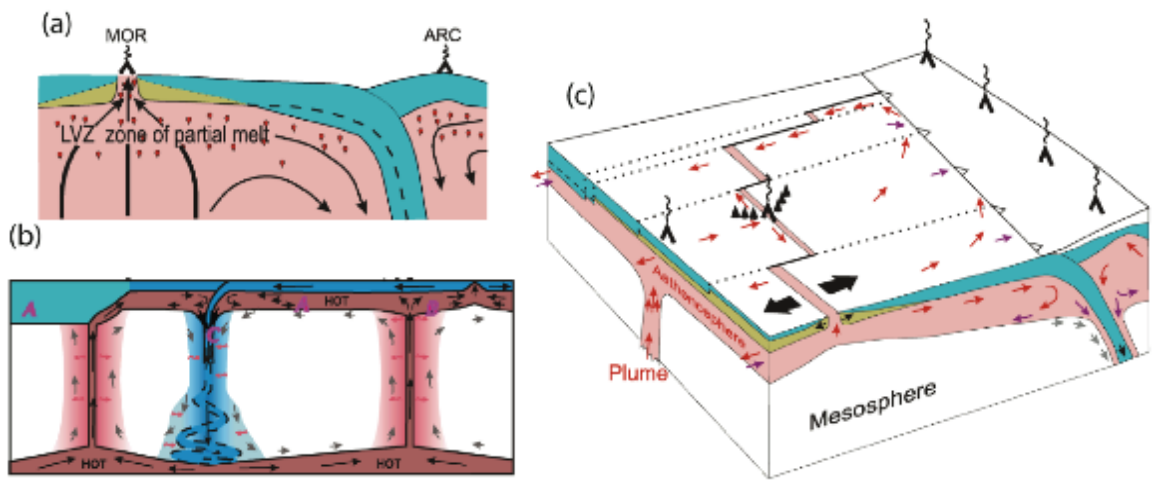


**Figure 1.** (a) Textbook view of the asthenosphere as a seismic low velocity zone (LVZ) embedded within a large-scale mantle convection cell. (b) Plume-fed asthenosphere conception of asthenosphere as a dynamic boundary layer within a more complex mode of whole mantle convection. Letters A, B and C show sites where emerging evidence is supporting this idea as discussed here; A - seismic geotherms; B - underside reflections from the base of the suboceanic asthenosphere; C - side-reflections from the base of the subduction slab. (c) View of likely flow characteristics of a more realistic plume-fed asthenosphere based on numerical experiments in (Yamamoto et al., 2007) and Fig. 5, 7 and 9 in this paper.

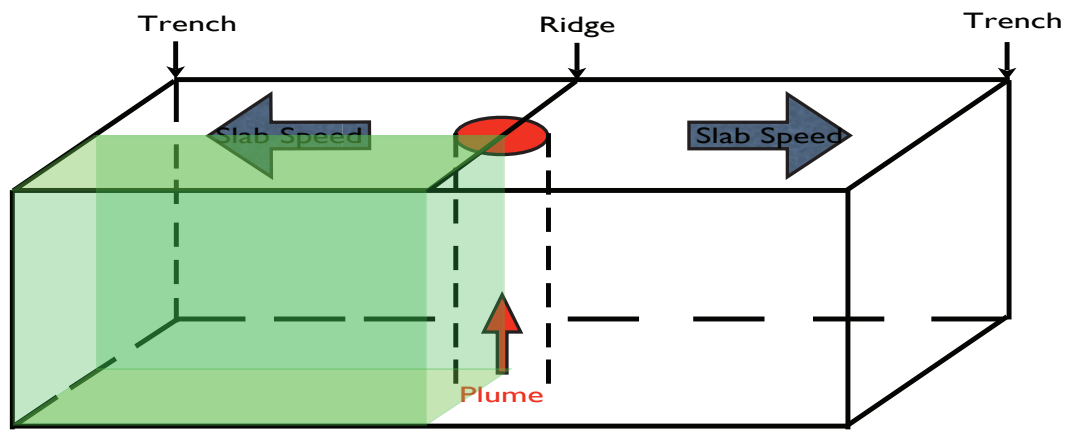


**Figure 2. Model setup for 3D ridge-centered plume experiments.** The model region is shown in green. We take advantage of problem symmetries to use only 1/4 the elements needed to resolve a high-resolution plume at an arbitrary point inside the box, i.e. we only mesh and solve for the green region -- 6000 km x 3000 km x 500 km.

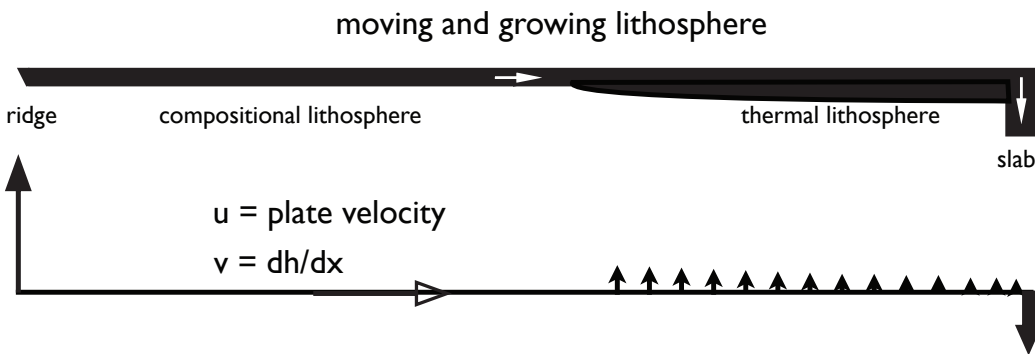


**Figure 3. Actual geometry of the Lithosphere-Asthenosphere-Boundary (LAB) geometry vs. our flat-top approximation.** The top panel is a cartoon for an oceanic lithosphere; the bottom figure is our flat approximation of the asthenosphere accretion into this moving, growing lithosphere with the proper vertical velocity boundary condition calculated from the top geometry, so that the flat LAB consumes asthenosphere the same way. For large scale flow models, these 2 kinds of boundary conditions have equivalent plate drag and asthenosphere consumption, therefore we choose the simpler-to-mesh flat approximation for these 3D experiments.

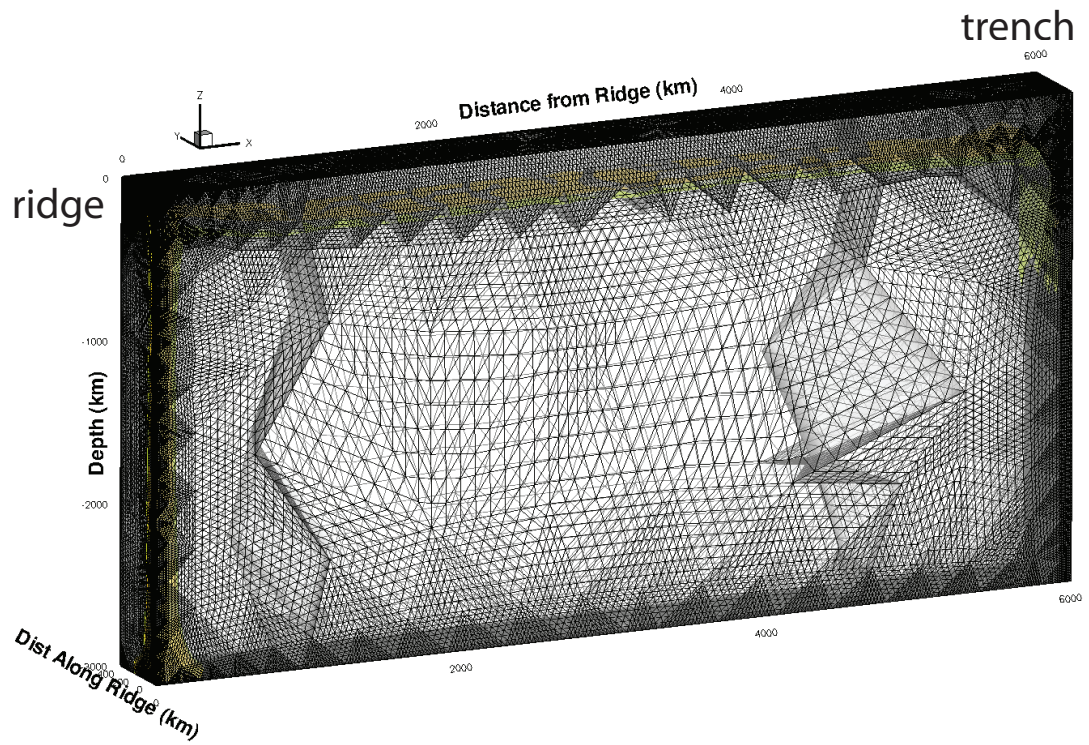


**Figure 4.** Unstructured mesh used for the on-ridge-axis Iceland-type plume 3D numerical experiments using GiD (CIMNE 2011). Finer elements are used in the plume, asthenosphere, slab, D'', and also in the near-trench region where counter flow may form. There are around 200 thousand degrees-of-freedom in a 2-level multigrid, and around 1.3 million degrees-of-freedom with a 3-level multigrid in this model, the smallest quadratic element in a 2-level multigrid has a characteristic size of  $\sim 3.7$  km.

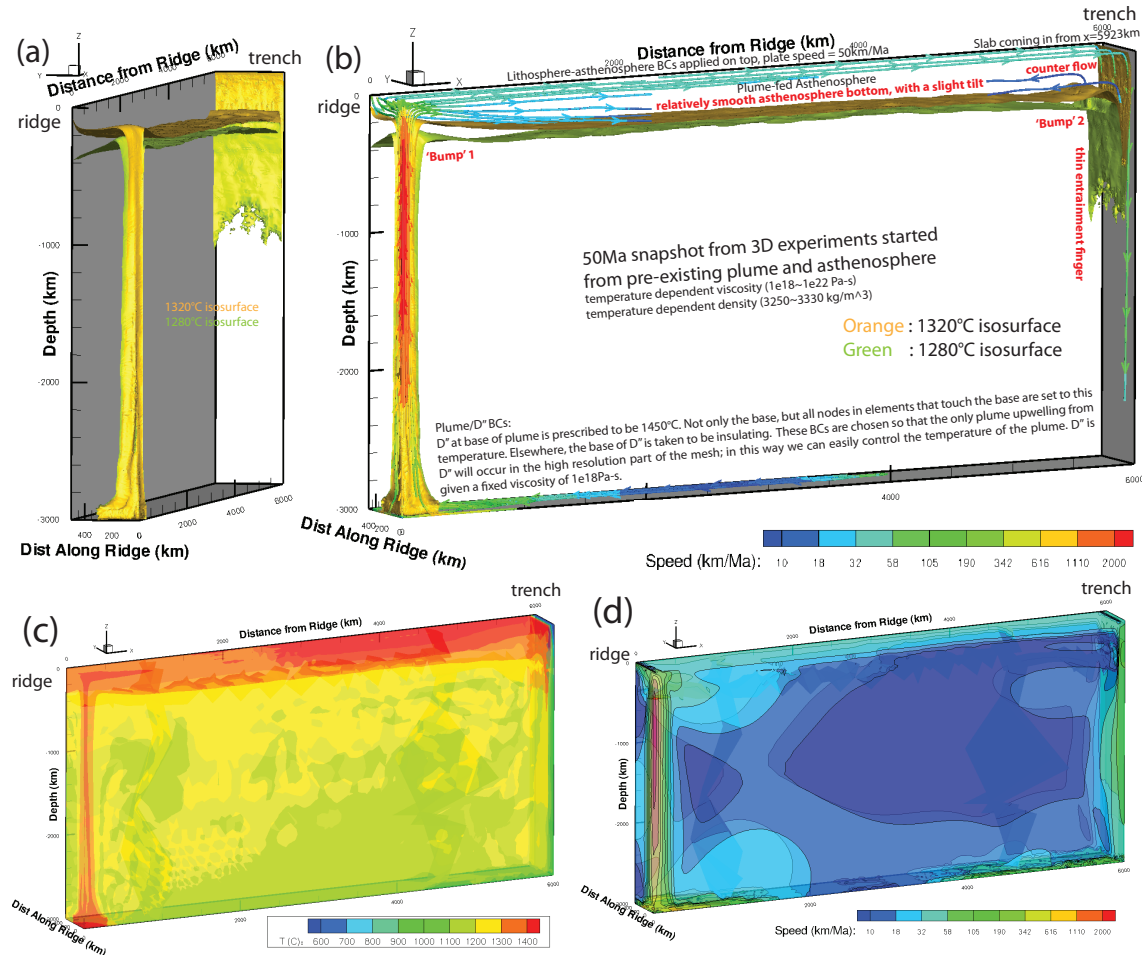


**Figure 5. Results of the on-ridge-axis Iceland-type plume experiment.** a) Ridge view of our computational domain: 1280°C (green) and 1320°C (orange) isosurfaces show the general geometry of a plume-fed asthenosphere. ‘Bumps’ related to dynamic isostasy are generated both at the plume and trench. b) Another view of the plume-fed asthenosphere: stream lines highlight the flow field within the plume and asthenosphere, the plume fills in the near-ridge side of the asthenosphere with radial flow, while counter flow is seen near trench. c) Temperature contours over the whole volume of our domain. The addition of hot plume material and asthenosphere counter flow keep the asthenosphere ~200°C warmer than underlying mantle. (d) Speed contours over the whole volume. Mantle flow slows down when ‘shielded’ from plate motions by a weak asthenosphere layer.

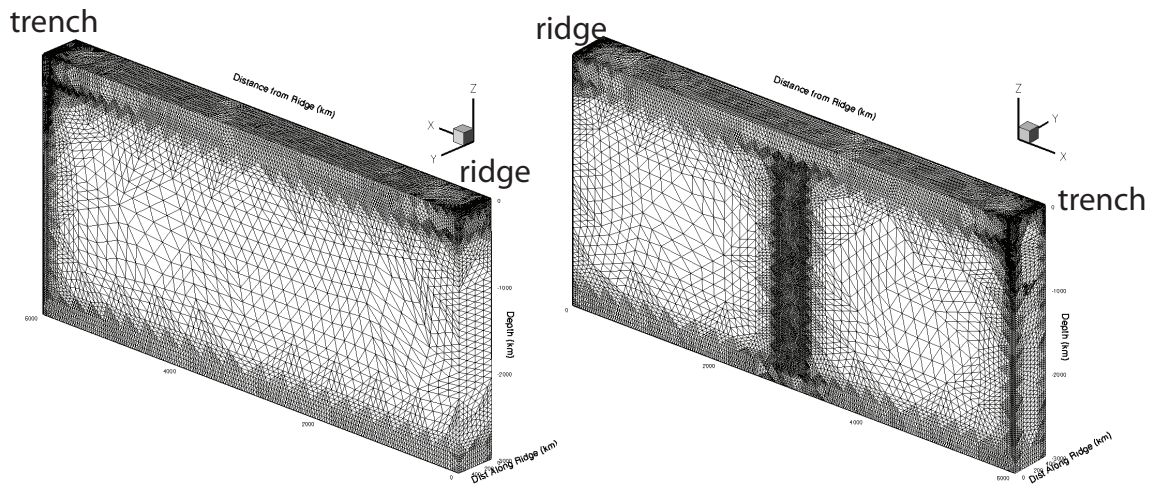


**Figure 6. Unstructured mesh used for the off-ridge-axis Hawaii-type plume 3D numerical experiments. Finer elements are used in the plume, asthenosphere, slab, D'', and also in the near-trench region where counter flow may form. This mesh has roughly 500 thousand degrees-of-freedom with a 2-level multigrid, or 3.5 million degrees-of-freedom with a 3-level multigrid.**

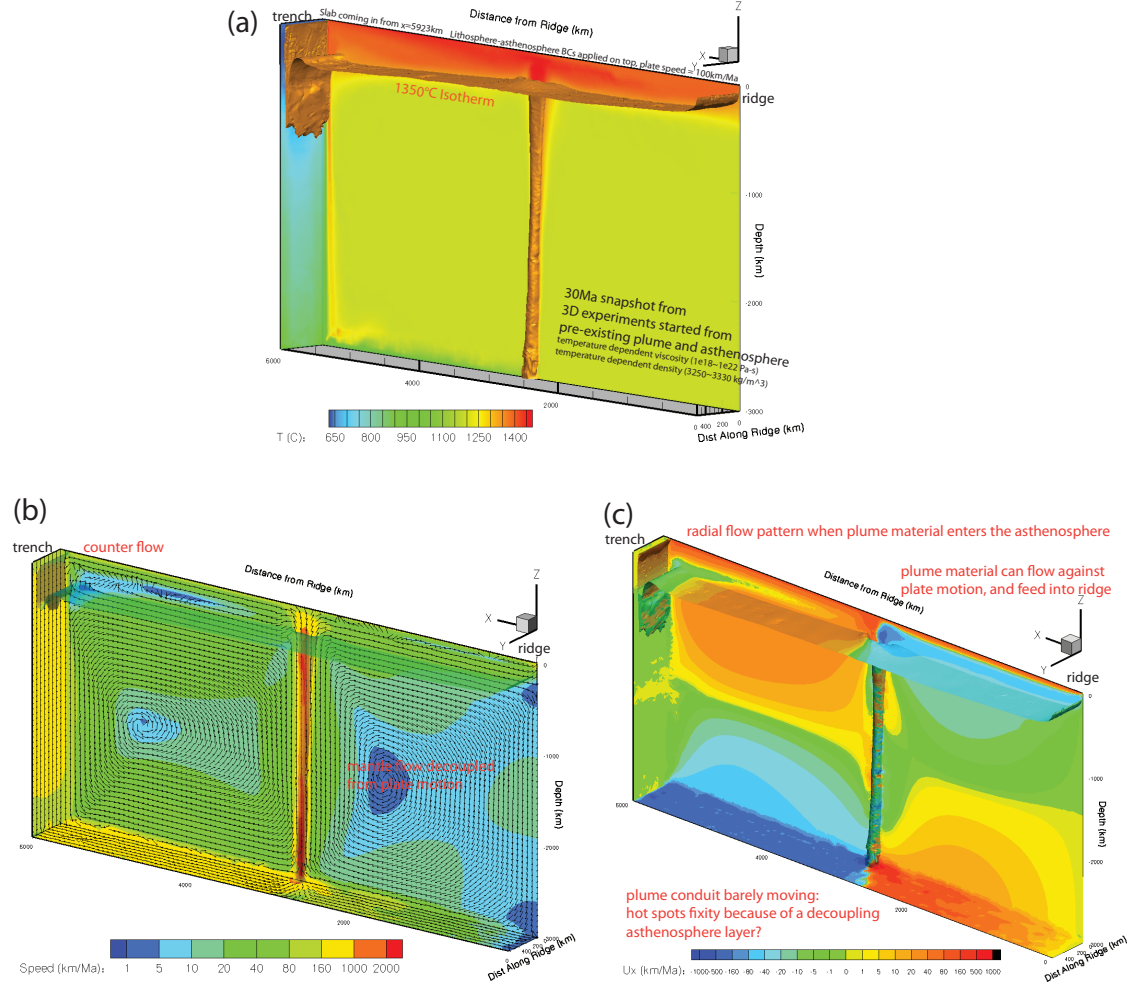


**Figure 7. Results of the off-ridge-axis Hawaii-type plume experiment. (a)** Ridge view of the temperature field in our off-axis plume run. The 1350°C isosurface shows the general geometry of a plume-fed asthenosphere. Plume feed and counter flow keeps the asthenosphere ~200°C warmer than underlying mantle. ‘Bumps’ related to dynamic isostasy are generated both at the plume and trench. **(b)** Velocity field. Color shows speed, arrows only show flow direction -- their length is uniform; the plume joins the asthenosphere with radial flow, while counter flow is seen near trench. High flow speed is seen within plume conduit, D” layer, asthenosphere and slab; while mantle flow slows down when shielded from plate motion by a weak asthenosphere. **(c)** Trench-perpendicular velocity field  $U_x$ . Plume material can flow relatively freely to all directions in the asthenosphere, due to its low viscosity; plume material can feed all the way towards ridge and trench. The lateral speed at the boundary of the plume conduit is almost zero – the plume remains relatively fixed in this scenario in an actively convecting mantle.

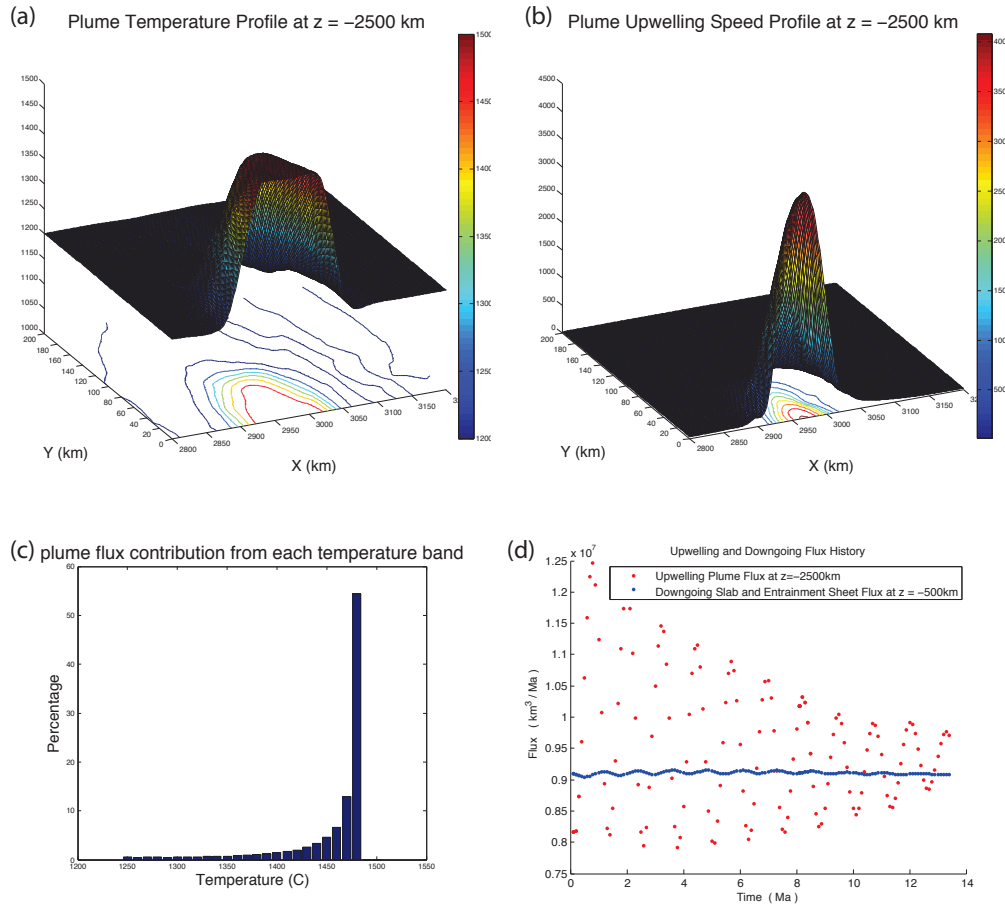


**Figure 8. Flux measurement in the plume conduit and in the subduction zone.** (a) Plume temperature cross-section at  $z = -2500$  km. The 3-D surface map and the 2D contour map underneath show the same dataset. The ambient mantle is at  $1200^\circ\text{C}$ , while the hottest part of plume is set to be  $1480^\circ\text{C}$ . (b) Plume upwelling speed on cross-section at  $z = -2500$  km. The 3-D surface map and the 2D contour map underneath are showing the same dataset. We see very high upwelling speeds in the central (hottest) part of the plume cross-section because it is both the most buoyant and least viscous part. The viscosity is this cross-section ranges from  $10^{18} \text{ Pa s}$  (plume axis) to  $10^{21} \text{ Pa s}$  (ambient mantle). (c) Plume flux contribution from each temperature band. Notice that because of the very high speed near the centerline of the plume, the central region with less than  $1/4$  of the plume's cross-sectional area accounts for more than half of the upwelling flux. (d) Upwelling plume flux (red) vs. downgoing slab flux (blue). In this run the upwelling and downgoing flux are almost equal -- which leads to a quasi-stable plume-fed asthenosphere. Clear evidence for a naturally pulsing plume is seen in this experiment.

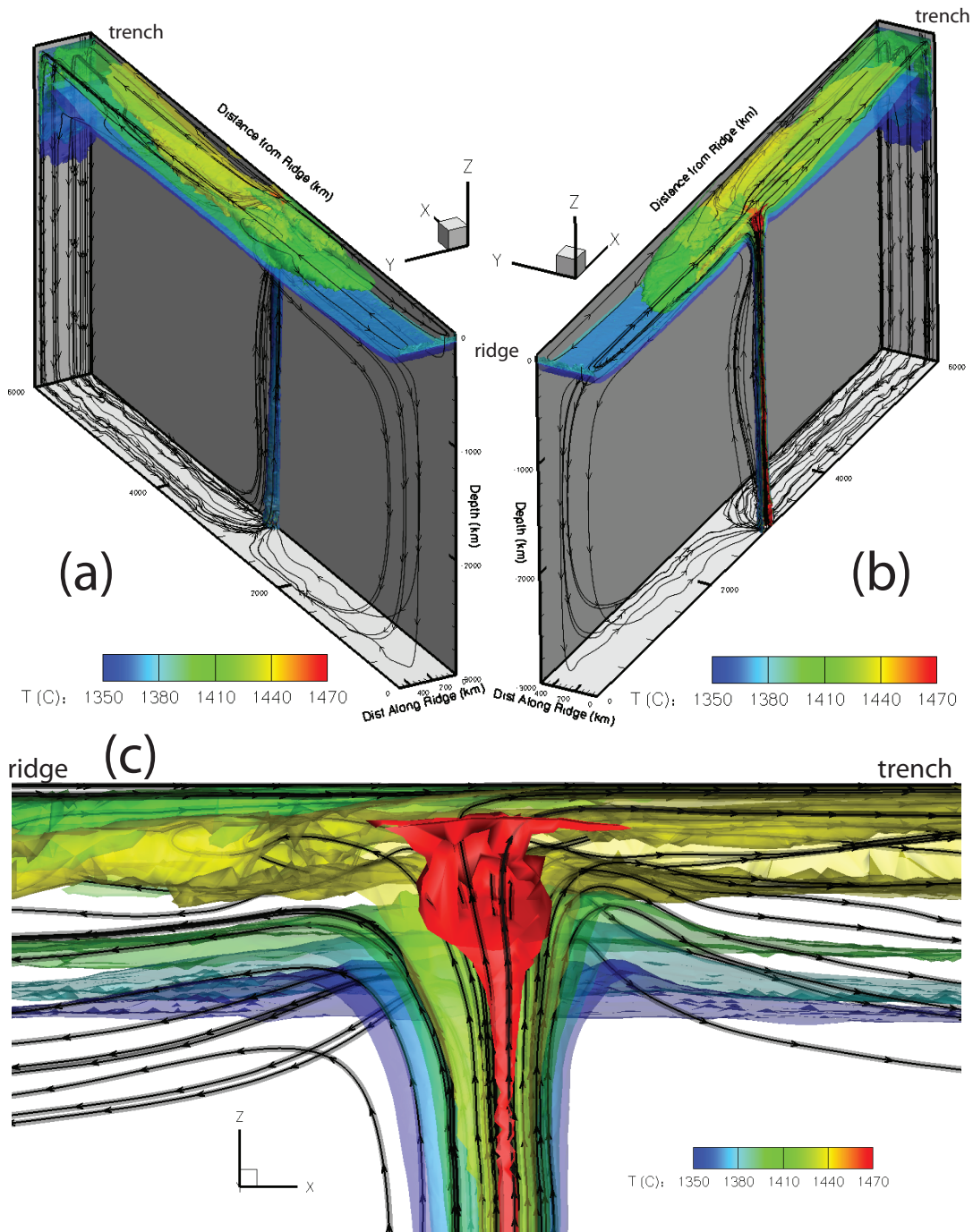


**Figure 9. Detailed flow lines and temperature structure.** In panels (a) and (b), temperature profile is shown as colored isotherms from 1350°C to 1470°C, while streamlines show the 3-D flow pattern in the plume-fed asthenosphere system. Hotter axial material in the plume tends to rise to shallower depths where it is more strongly dragged by the overriding plate. Cooler material from the rim of plume enters into deeper parts of asthenosphere, where it can flow to either ridge or trench (c) zoom into the plume entrance. Notice that the flow field is linked to a dynamic ‘bump’ in the relief at the base of the buoyant asthenosphere.

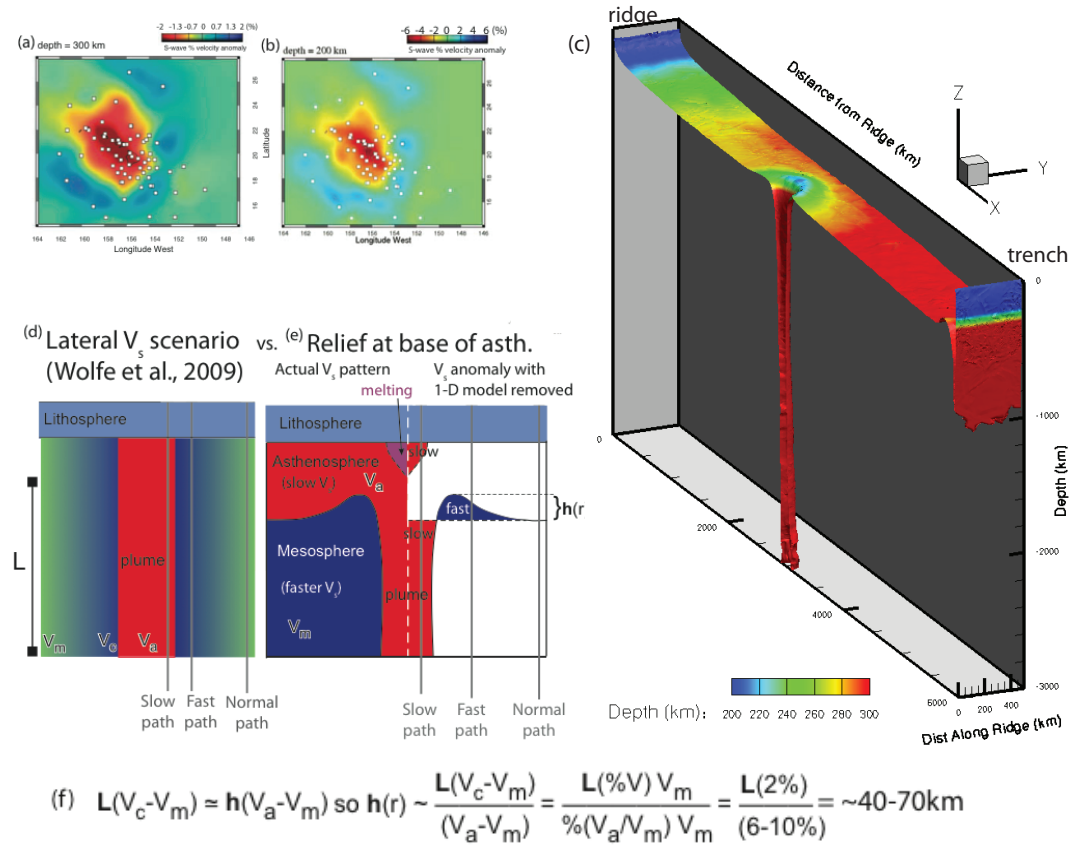


**Figure 10.** Plume bump (dynamic topography) -- reinterpretation of PLUME (Wolfe et al., 2009) inversion for lateral seismic variations beneath Hawaii. (a) PLUME Vs structure beneath Hawaii (300-km-depth of their Fig. 2). A similar pattern is found between 100–400 km depths. Slow plume conduit seen between 100–1200 km depths. (b) The PLUME anomaly was recovered using a procedure that tried to force as much travel-time anomaly as possible into structure between 50–250 km depths (their Fig. S9b). We use these wave speed variations to estimate amplitude of the dynamic ‘bump’ at base of a plume-fed asthenosphere. (c) Topography at the base of a ~150-km-diameter plume from the off-axis plume model. Note similar ‘bump’ of relief. (d) Lateral velocity variations assumed in PLUME analysis, with ray paths shown for slow, fast, and normal arrival times. (e) Lateral velocity variations assumed in our geodynamic reinterpretation of PLUME results. We relate shear wave arrival time anomalies to dynamic relief on the base of a buoyant asthenosphere; relief induced by buoyancy of the underlying plume-conduit. Slow, Fast, and Normal shear wave paths are shown for this scenario. (f) Equation used to estimate the dynamic relief — 40–70 km — predicted by the PLUME experiment’s inferred travel-time delays.